



الجامعة الإسلامية بالمدينة المنورة
ISLAMIC UNIVERSITY OF MADINAH

**The Islamic University Journal
of Applied Sciences (IUJAS)**
Refereed periodical scientific journal

An Open Access Journal



Print ISSN: 1658-7936
Online ISSN: 1658-7944

Special Issue – December 2025



بِسْمِ اللَّهِ الرَّحْمَنِ الرَّحِيمِ



Islamic University Journal of Applied Sciences (IUJAS)



***The Islamic University Journal of Applied Sciences
(IUJAS)***

Issued By

Islamic University of Madinah, Madinah, Saudi Arabia

Special Issue

**7th International Symposium on New and Renewable Energies
October 15 - 16, 2025 Ghardaïa, Algeria**



December 2025

Paper version

Filed at the King Fahd National Library No. 8742/1439 on 17/09/1439
AHInternational serial number of periodicals (ISSN) 1658-7936

Online version

Filed at the King Fahd National Library No. 8742/1439 on 17/09/1439
AHInternational Serial Number of Periodicals (e-ISSN) 1658-7944

The Journal's Website

<https://journals.iu.edu.sa/jesc>

(The views expressed in the published papers reflect the views of the researchersonly, and do not necessarily reflect the opinion of the journal)

Publication Rules at the Journal (*)

❖ General rules:



- Report original scientific research (the main results and conclusions must not have been published or submitted elsewhere).
- Fit with the topics of the journal.
- Report novel results, innovative work and show a new scientific contribution.
- Not to bear similarity of more than 25% of a previously published work of the same author(s).
- Follow the rules, regulation and authentic research methodologies.
- Fulfill the required items and the format of the journal provided in appendix below related to the guide for author.
- Opinions expressed in published articles commit the authors themselves only and not necessarily the opinion of the journal.

❖ For all articles:



- The exclusive right to publish and distribute an article, and to grant rights to others, including commercial purposes.
- For open access articles, IU will apply the relevant third-party user license where IU publishes the article on its online platforms.
- The right to provide the article in all forms and media so the article can be used on the latest technology even after publication.
- The authority to enforce the rights in the article, on behalf of an author, against third parties, for example in the case of plagiarism or copyright infringement.






(*) These general rules are explained in details along with other rules for Author's guide in the journal's website:
<https://journals.iu.edu.sa/jesc>



Editorial Board

	<p>Editor-in-Chief: Mohamed Benghanem</p> <p>Professor, Faculty of Science, Islamic University of Madinah, Saudi Arabia.</p> <p>Orcid: https://orcid.org/ 0000-0002-2527-8741</p>
	<p>Managing Editor: Ahmad B. Alkhodre</p> <p>Professor, Computer science, Islamic University of Madinah. Saudi Arabia</p> <p>Orcid: https://orcid.org/0000-0001-6168-3552</p>

Editorial Board Members

	<p>Aly Ramadan Seadawy</p> <p>Professor, Mathematics, Taibah University, Madinah, Saudi Arabia</p> <p>Orcid: https://orcid.org/0000-0002-7412-4773</p>
	<p>Reda Abdelmonsef A. Ibrahim</p> <p>Professor, Biology, Kafrelsheikh University, Egypt</p> <p>Orcid: https://orcid.org/0000-0001-6472-5666</p>

	<p>Mussa. A. Said</p> <p>Professor, Chemistry, Islamic University of Madinah, Saudi Arabia.</p> <p>Orcid: https://orcid.org/0000-0003-3073-5449</p>
	<p>Fazal Noor</p> <p>Professor, Computer science and engineering, Islamic University of Madinah. Saudi Arabia</p> <p>Orcid: https://orcid.org/0000-0002-0096-3435</p>
	<p>Basem Rashid Alamri</p> <p>Associate Professor, Electrical Engineering, Taif University, Saudi Arabia</p> <p>https://orcid.org/0000-0002-8667-0042</p>
	<p>Saad Talal Alharbi</p> <p>Professor in Computer Science, Human Computer Interaction, Faculty of Computers, Taibah University, Saudi Arabia</p> <p>https://orcid.org/0000-0003-0913-8631</p>
	<p>Yazed Alsaawy</p> <p>Associate Professor, Computer and information systems, Islamic University of Madinah. Saudi Arabia</p> <p>Orcid: https://orcid.org/0000-0001-5031-3388</p>

	<p>Abdul Qadir Bhatti</p> <p>Professor, Civil Engineering, Faculty of Engineering, Islamic University of Madinah. Saudi Arabia</p> <p>ORCID Link https://orcid.org/0000-0001-5433-7803</p>
	<p>Shamsuddin Ahmed</p> <p>Professor, Industrial Engineering, The Faculty of Computer and Information Systems Islamic University of Madinah, Saudi Arabia.</p> <p>https://orcid.org/ orcid.org/</p>

Editorial Secertary

	<p>Ahmad Ziad Al-Zuhaily</p> <p>Assistant Editor, Computer science, Engineer, Islamic University of Madinah. Saudi Arabia</p>
	<p>Abdulrahman Saeed Odeh</p> <p>Assistant Editor, Computer science, Engineer, Islamic University of Madinah. Saudi Arabia</p>

Table of Contents

Article Number	Article Title	Page
1	Practical Validation of an Adaptive-Gain Fractional-Order PI Controller for Grid-tied PV Systems	1
2	Performance Evaluation of P&O, improved Sliding Mode and Fuzzy Logic MPPT Methods in PV Systems: A Comparative Study under uniform and non-uniform conditions.	14
3	A socio-economic approach to agricultural drying activities in the Ghardaïa region of the Sahara	25
4	Advanced Network Voltage Control for Grid-Connected PV Systems Using Smart PV Inverter Capabilities	34
5	Experimental Investigation on Vapor Condensation and Removal in a Box Solar Cooker Using a Pressure Cooker Integrated with a Flexible Pipe	48
6	Relationship between geometric shapes of hollow bricks and their thermal efficiency: Case of a single-family house in hot desert climates	58

7	Performance Enhancement of Solar Modules in Arid Climates: Dust Mitigation Strategies in Ghardaïa, Algeria	71
8	Hybrid MPPT - Simple boost control of Z source inverter integrated in standalone PV systems	80
9	Heat Transfer Enhancement in Solar Air Heaters Using Porous Ribs	91
10	Photocatalytic Hydrogen Production From TiO ₂	101
11	Study Of Mechanical, Electronic and Optical Characteristics for AuBiF ₃ Material	113



Practical Validation of an Adaptive-Gain Fractional-Order PI Controller for Grid-tied PV Systems

Antar Beddar ^{1,*}, Farid Hadjrioua ¹, Issam Abadlia ², Hadj M. Idriss ¹, Djafer Djelloul ¹

¹ Unité de recherche appliquée en énergie renouvelable, Ghardaïa, Algeria, beddarantar@gmail.com 1

² Centre de développement des énergies renouvelables, Algiers, Algeria,

*Corresponding author: (Antar Beddar), Email Address: beddarantar@gmail.com

Abstract

This study investigates energy management in grid-connected photovoltaic (PV) systems, with particular emphasis on the regulation of active and reactive power exchanged with the utility grid under dynamic operating conditions. The intermittent nature of solar energy and grid disturbances requires control strategies capable of ensuring fast response and high-power quality. To address these challenges, an adaptive-gain fractional-order proportional–integral (AG-FOPI) controller is proposed for the inner current control loop of a grid-tied PV inverter. The controller combines the robustness and memory properties of fractional-order integration with an adaptive proportional gain to enhance transient performance while preserving steady-state accuracy. The proposed control strategy is implemented and validated using real-time hardware-in-the-loop (HIL) experimentation based on a TI F28379D digital control platform. Experimental results demonstrate fast and accurate tracking of active and reactive power references, with settling times below 10 ms and negligible overshoot during dynamic transitions. In addition, the injected grid current exhibits low harmonic distortion, with total harmonic distortion consistently maintained below 1.8%. These results confirm the practical suitability of the AG-FOPI controller for grid-tied photovoltaic applications.

Keywords: Grid-tied photovoltaic systems; Fractional-order control; Adaptive proportional gain; Hardware-in-the-loop (HIL); Active and reactive power control.

<https://doi.org/10.63070/jesc.2025.035>

Received 10 July 2025; Revised 05 November 2025; Accepted 05 December 2025;

Available online 24 December 2025.

Published by Islamic University of Madinah on behalf of *Islamic University Journal of Applied Sciences*.

This is a free open access article under the Creative Attribution (CC.BY.4.0) license.

1. Introduction

The development of industrial and urban activities is accompanied by a growing energy demand, exerting increased pressure on fossil resources and accentuating environmental problems linked to greenhouse gas emissions. In recent decades, this continuous rise in electricity consumption has further highlighted the limitations of conventional energy systems and reinforced the need for sustainable alternatives [1], [2]. Renewable energies—and photovoltaics (PV) in particular—are becoming a strong solution for a sustainable energy transition. Thanks to their modularity, abundant availability, and steadily falling production costs, PV systems are increasingly being integrated into distribution networks. As deployment accelerates worldwide, PV technology has become a major contributor to distributed generation and a key component of modern power networks [3].

However, photovoltaic energy injection into the electrical grid presents major technical challenges. Due to the intermittent nature of solar radiation and dynamic operating conditions of the grid, managing both active and reactive power in compliance with grid standards is complex. The inverter plays a crucial role in this context: it must ensure a high-quality conversion of DC power into AC while minimizing harmonic distortion (THD) and enabling precise control of energy exchange. These requirements become increasingly stringent with higher PV penetration levels, where voltage fluctuations, fast irradiance variations, and grid disturbances can significantly affect system stability and power quality [4], [5]. Therefore, inverter control strategies must guarantee fast dynamic response while preserving low current distortion and accurate power regulation under varying operating conditions [6].

Conventional Proportional–Integral (PI) controllers remain widely used due to their simple design and effective steady-state performance. Yet, they often suffer from weak disturbance rejection and slow dynamic response in rapidly changing environments. These limitations are particularly critical in grid-connected PV systems, where sudden changes in irradiance, load, or grid voltage require fast and adaptive control actions [7]. Moreover, the fixed-parameter structure of classical PI controllers restricts their ability to cope with nonlinearities and time-varying dynamics inherent to power electronic converters, often leading to overshoot, steady-state errors, and degraded harmonic performance under real operating conditions [8], [9].

To overcome these drawbacks, numerous advanced control strategies have been investigated in the literature, including model predictive control, sliding mode control, adaptive backstepping, feedback linearization, and artificial intelligence–based techniques such as neural networks and fuzzy logic controllers [10–13]. Although these methods can significantly improve dynamic performance and

tracking accuracy, they are often associated with high computational complexity, demanding tuning procedures, or reduced suitability for real-time embedded implementation.

Among emerging alternatives, fractional-order control techniques have attracted considerable attention. By extending the integration and differentiation orders from integer to non-integer values, fractional-order PI (FOPI) controllers introduce additional degrees of freedom that allow more precise shaping of system dynamics and improved robustness against parameter uncertainties [14–16]. Several studies have reported superior transient response, enhanced disturbance rejection, and better frequency-domain characteristics of FOPI controllers compared to classical PI controllers, particularly in grid-connected PV applications [17], [18]. Nevertheless, most reported results rely mainly on numerical simulations, and practical validation through real-time experimental platforms remains limited.

In parallel, adaptive control mechanisms have been proposed to further enhance inverter performance by adjusting controller parameters online according to system behavior. Adaptive gain strategies enable aggressive control action during transients while maintaining stability and reduced oscillations near steady state [19]. However, the combination of adaptive gain mechanisms with fractional-order control, and their validation under realistic real-time conditions, is still insufficiently explored in the existing literature.

This work addresses this research gap by investigating the practical implementation and real-time validation of an adaptive-gain fractional-order proportional–integral (AG-FOPI) controller for grid-connected photovoltaic systems.

The proposed controller combines the memory and robustness properties of fractional-order integration with an adaptive proportional gain mechanism to ensure fast transient response and improved steady-state performance. The controller parameters are optimized using the Particle Swarm Optimization (PSO) algorithm to achieve an optimal compromise between dynamic response, stability, and power quality.

A key contribution of this study is the primarily validated through Hardware-in-the-Loop (HIL) experimentation. By implementing the control algorithm on a TI F28379D digital control platform and interfacing it with a real-time simulated power stage, the proposed approach enables realistic assessment of implementation constraints such as sampling delays, quantization effects, and computational limitations, which are often neglected in purely simulation-based studies. Experimental results demonstrate accurate regulation of active and reactive power, reduced total harmonic distortion

of grid-injected currents, and improved robustness compared to conventional PI and standard FOPI controllers.

The remainder of this paper is organized as follows. Section 2 presents the modeling of the grid-connected PV system. Section 3 describes the design of the AG-FOPI controller and the PSO-based optimization procedure. Section 4 presents the Hardware-in-the-Loop experimental setup. Section 5 discusses the experimental results. Finally, Section 6 concludes the paper.

2. System Description and Modeling

The overall architecture of the studied single-phase grid-connected photovoltaic (PV) system is depicted in Fig. 1. The system is composed of three main functional blocks: the DC power generation unit, the power conversion and filtering unit, and the control and synchronization unit.

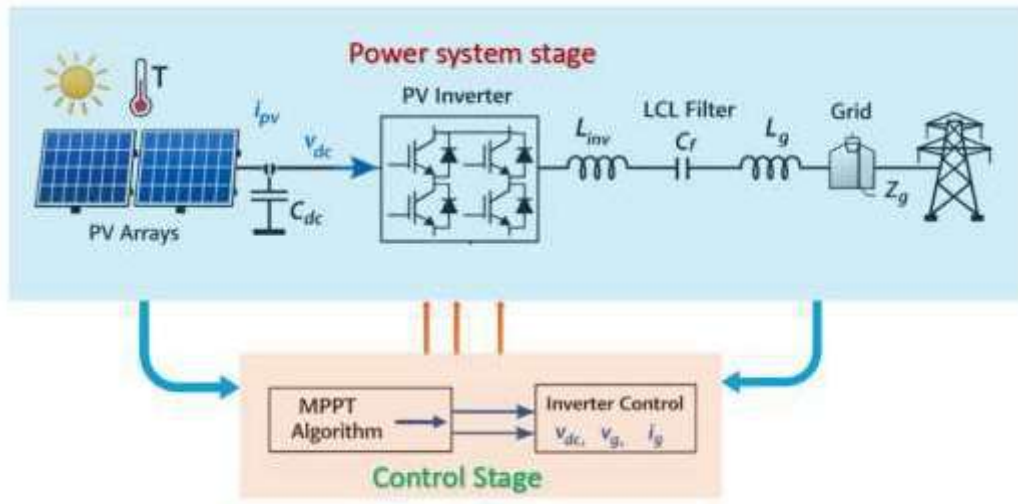


Figure 1. Architecture of the single-phase grid-connected photovoltaic system.

2.1 DC Power Generation Unit

A programmable DC power source is used to emulate the behavior of a photovoltaic generator. This approach allows controlled reproduction of PV operating conditions and facilitates repeatable real-time testing within the HIL environment. A DC-link capacitor C_{dc} is connected in parallel with the DC source to ensure power decoupling, stabilize the DC bus voltage, and attenuate high-frequency voltage ripple induced by inverter switching.

The DC-link voltage regulation is essential to guarantee proper inverter operation and to ensure that sufficient energy is available for grid injection under varying load and power demand conditions.

2.2 Power Conversion and Filtering Unit

The DC/AC conversion stage consists of a single-phase two-level Voltage Source Inverter (VSI). The inverter is followed by an LCL filter composed of inverter-side inductance L_{inv} , grid-side inductance L_g , and filter capacitor C_f , where L_{inv} , L_g , and C_f denote the inverter-side inductance, grid-side inductance, and filter capacitor, respectively. The LCL filter is designed to attenuate switching harmonics while maintaining low total harmonic distortion (THD) in the grid-injected current, ensuring compliance with grid interconnection standards.

An autotransformer may be used to adapt voltage levels and improve coupling with the utility grid, particularly in laboratory or experimental setups.

2.3 Control and Synchronization Unit

The control structure adopts a hierarchical dual-loop strategy. The outer voltage control loop regulates the DC-link voltage v_{dc} by comparing it to its reference value v_{dc}^* . The inner loop controls the grid-injected current i_g , ensuring accurate tracking of the reference current i_g^* , which is derived from the active and reactive power setpoints P^* and Q^* . This loop incorporates the proposed Adaptive-gain Fractional-Order PI (AG-FOPI) controller, whose role is to enhance transient response, improve robustness, and reduce steady-state error under dynamic operating conditions.

To ensure proper synchronization with the grid, a Phase-Locked Loop (PLL) is employed to estimate the grid voltage phase angle θ . The estimated angle enables transformation of system variables from the stationary frame to the rotating dq reference frame, using Clarke and Park transformations. In the dq frame, the inverter dynamics are simplified, allowing decoupled control of active and reactive power.

2.4 Dynamic Model in the dq Reference Frame

The inverter current dynamics expressed in the dq reference frame are given by:

$$\begin{cases} \dot{i}_d = -\frac{R}{L}i_d + \omega i_q - \frac{1}{L}V_d + \frac{V_{dc}}{L}S_d \\ \dot{i}_q = -\frac{R}{L}i_q - \omega i_d - \frac{1}{L}V_q + \frac{V_{dc}}{L}S_q \end{cases} \quad (1)$$

where S_d and S_q are the modulation signals generated by the control law, V_d and V_q are the grid voltage components in the dq frame, ω is the grid angular frequency, and R and L represent the equivalent resistance and inductance of the filter.

Switching and conduction losses are neglected in this modeling stage for control design purposes. Nonlinear coupling terms are compensated using feedforward techniques, which allows independent regulation of the current components.

Under these assumptions, the active and reactive powers injected into the grid can be expressed as:

$$\begin{cases} P = \frac{3}{2}(V_d I_d + V_q I_q) \\ Q = \frac{3}{2}(V_q I_d - V_d I_q) \end{cases} \quad (2)$$

These expressions clearly demonstrate that, under grid-oriented control where $V_q \approx 0$, active power is primarily controlled through I_d , while reactive power is governed by I_q . This property forms the theoretical basis for the decoupled control strategy adopted in this work.

2.5 Summary of the Control-Oriented Model

The proposed system architecture enables efficient energy injection into the utility grid with independent regulation of active and reactive power. The use of the dq reference frame simplifies control design and allows the proposed AG-FOPI controller to operate effectively within the inner current loop.

3. AG-FOPI Controller Design

To ensure robust and high-performance control of the grid-injected current, this work proposes an Adaptive-Gain Fractional-Order Proportional–Integral (AG-FOPI) controller. The controller is specifically designed for the inner current loop of a grid-connected PV inverter, where fast dynamic response and robustness against disturbances are critical. The proposed approach combines the memory properties of fractional-order calculus with a nonlinear adaptive mechanism applied to the proportional gain, enabling improved performance under varying operating conditions.

3.1 Control Law Formulation

The control input $u(t)$ applied to the inner current loop is defined as:

$$u(t) = k_p(e(t)) \cdot e(t) + k_i \cdot D^{-\lambda} e(t) \quad (3)$$

where:

- $e(t) = i_g^*(t) - i_g(t)$ is the current tracking error,
- $D^{-\lambda}$ denotes the fractional-order integral operator of order λ with $0 < \lambda \leq 1$,
- k_i is the constant integral gain,
- $k_p(e)$ is an adaptive proportional gain that adjusts according to the error magnitude.

Unlike classical PI and standard FOPI controllers with fixed gains, the proposed AG-FOPI structure dynamically adjusts the proportional action, allowing the controller to react aggressively during transients while maintaining smooth behavior near steady state.

3.2 Adaptive Proportional Gain Mechanism

The adaptive proportional gain is defined using a hyperbolic tangent function:

$$k_p(e) = k_{p0} + \Delta k_p \cdot \tanh(\alpha |e(t)|) \quad (4)$$

where:

- k_{p0} is the nominal proportional gain,
- Δk_p determines the maximum gain variation,
- α controls the sensitivity of the gain adaptation.

This nonlinear adaptation law ensures a smooth and bounded variation of the proportional gain. For large tracking errors, the gain increases rapidly, providing strong corrective action and improving transient response. As the error decreases, the gain gradually saturates toward its nominal value, which helps reduce steady-state oscillations and prevents excessive control effort.

The adaptive mechanism therefore provides:

- Fast transient response under sudden disturbances or reference changes;
- Reduced steady-state ripple and improved stability near equilibrium;
- Enhanced robustness against parameter uncertainties and grid disturbances.

3.3 Advantages of Fractional-Order Integration

The fractional-order integral term $D^{-\lambda}e(t)$ introduces a distributed memory effect that cannot be achieved with classical integer-order integration. This property allows more flexible shaping of the closed-loop dynamics by adjusting the order λ .

Compared to conventional PI controllers, the fractional-order formulation:

- Improves the trade-off between response speed and steady-state accuracy;
- Enhances robustness to system parameter variations, particularly in the presence of grid impedance uncertainty;

- Provides smoother dynamic behavior under rapidly changing operating conditions, such as fluctuating irradiance or grid disturbances.

These characteristics make fractional-order control particularly suitable for grid-connected PV applications, where system dynamics are inherently nonlinear and time-varying.

3.4 Parameter Optimization Using PSO

The AG-FOPI controller parameters $\{k_{p0}, \Delta k_p, k_i, \lambda, \alpha\}$ are optimized using the Particle Swarm Optimization (PSO) algorithm. PSO is selected due to its simplicity, fast convergence, and ability to handle nonlinear, multi-objective optimization problems without requiring gradient information.

The objective function minimized by PSO is defined as:

$$J = w_1 T_s + w_2 M_p + w_3 \text{ISE} \quad (5)$$

where:

- T_s is the settling time,
- M_p is the maximum overshoot,
- ISE is the integral of the squared error,
- w_1, w_2, w_3 are weighting coefficients reflecting control priorities.

This cost function ensures a balanced optimization that simultaneously addresses transient performance, overshoot limitation, and steady-state accuracy. The weighting coefficients are selected to favor fast response while maintaining acceptable power quality and stability.

3.5 Digital Implementation Aspects

The AG-FOPI controller is implemented in discrete time using the Grünwald–Letnikov approximation for the fractional-order integral term. This approximation is well suited for real-time digital implementation and provides a good compromise between accuracy and computational complexity.

The controller is deployed within the inner current loop of the dual-loop control architecture, while the outer loop regulates the DC-link voltage using a conventional PI controller.

4. Hardware-in-the-Loop Experimental Setup

Hardware-in-the-Loop (HIL) testing is a real-time validation technique that enables the evaluation of control algorithms on actual digital hardware while the physical power system is simulated in real

time. This approach provides a realistic compromise between offline simulation and full-scale experimental testing, allowing safe, repeatable, and cost-effective validation under conditions close to real grid operation.

In this work, the HIL platform is used to validate the proposed AG-FOPI controller. The power stage of the grid-connected PV system—including the photovoltaic source, single-phase voltage source inverter, LCL filter, and utility grid—is modeled in MATLAB/Simulink and executed in real time on a host computer. The control algorithm is implemented on a TI F28379D digital signal controller, which interfaces with the simulated plant through a UART communication interface over a USB connection, ensuring closed-loop operation under real-time constraints.

This configuration allows realistic assessment of embedded implementation constraints, such as sampling delays, quantization effects, and computational limitations, which are typically neglected in purely simulation-based studies. The HIL platform operates at a sampling frequency of 5 μ s, which is sufficient to capture the fast dynamics of power electronic converters and current control loops.

The overall architecture of the HIL setup is illustrated in Fig. 2, showing the interaction between the real controller hardware and the simulated power stage. This setup ensures that the controller behavior observed during testing closely reflects real-world operating conditions.

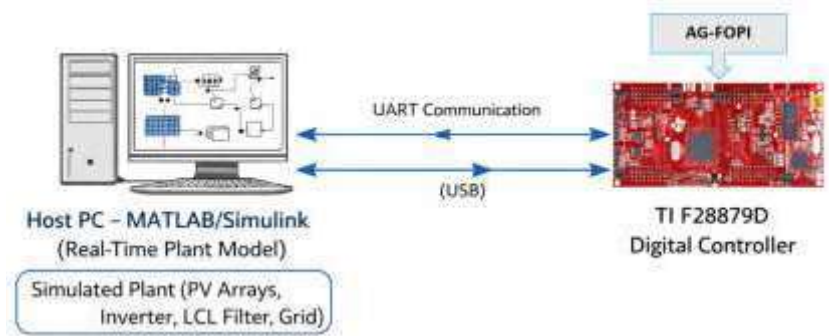


Figure 2. Hardware-in-the-loop experimental setup for the grid-connected PV system.

5. Results and Discussion

This section presents and discusses the experimental results obtained from the HIL validation of the proposed AG-FOPI controller. The results focus on dynamic performance, power quality, decoupling capability, and comparison with conventional PI control, under identical operating conditions.

5.1 Active and Reactive Power Control Performance

Fig. 3 illustrates the active and reactive power injected into the grid under step changes in the P Q reference. The AG-FOPI controller achieves fast and accurate tracking of both active and reactive power references. Settling times are approximately 10 ms, with negligible overshoot, demonstrating the effectiveness of the adaptive proportional gain during transient conditions. This behavior is mainly attributed to the adaptive proportional gain, which increases the control action during transient conditions and smoothly decreases near steady state.

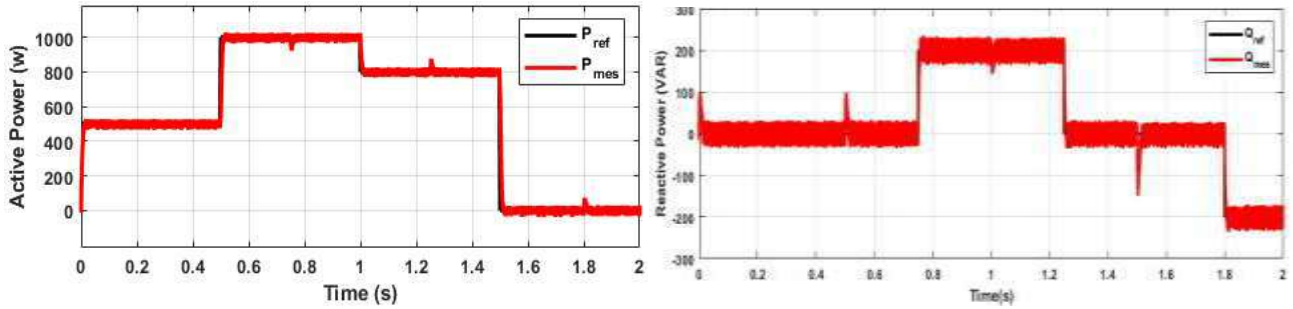


Figure 3. Active and reactive power responses.

The decoupled control capability is clearly observed, as variations in the active power reference P^* have minimal influence on the reactive power response Q , and vice versa. This confirms the suitability of the dq-based control structure combined with the AG-FOPI controller for independent regulation of power components.

5.2 Grid Voltage and Current Waveforms

Fig. 4 presents the grid voltage and injected current waveforms. The injected current remains sinusoidal and synchronized with the grid voltage, even during abrupt changes in power references. This indicates effective phase synchronization through the PLL and accurate current regulation by the inner control loop.

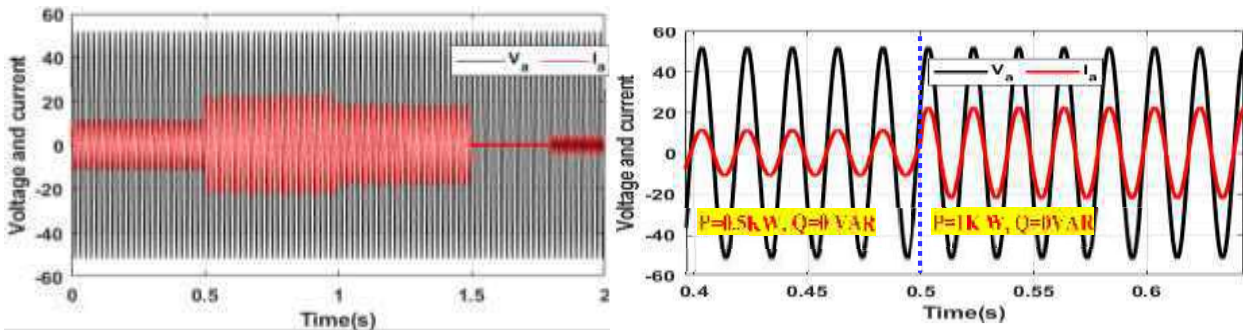


Figure 4. grid voltage and injected current waveforms under P, Q change

5.3 Harmonic Performance Analysis

The harmonic performance of the injected grid current is evaluated using Total Harmonic Distortion (THD) analysis. Fig. 5 shows the measured THD under various operating scenarios. The THD remains consistently below 1.8%, satisfying typical grid code requirements and confirming the controller's ability to maintain high current quality.

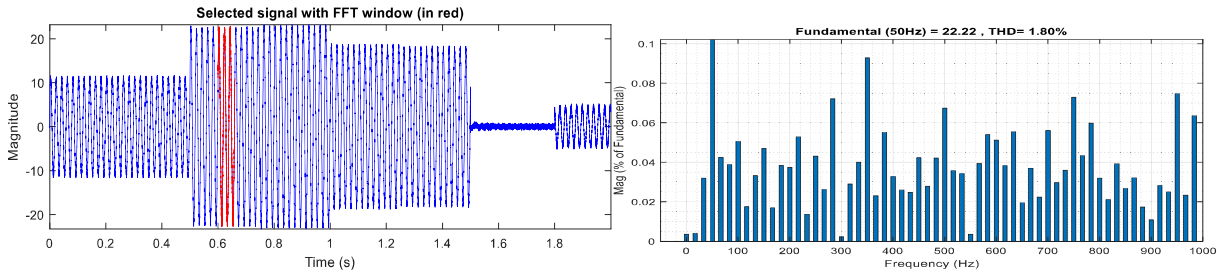


Figure 5. THD Current injected

This low THD level demonstrates the advantage of combining fractional-order integration with adaptive gain control, which improves dynamic response without sacrificing steady-state harmonic performance.

5.4 Comparative Analysis with Classical PI Control

To further highlight the benefits of the proposed approach, a comparative study is conducted between the AG-FOPI controller and a conventional PI controller under identical test conditions. Table I summarizes the comparison in terms of settling time, overshoot, steady-state error, injected current THD, robustness against disturbances, and coupling between active and reactive power.

The AG-FOPI controller exhibits a significantly faster settling time and reduced overshoot compared to the classical PI controller, while maintaining lower THD and improved robustness. The adaptive proportional gain enables aggressive response during transients while preserving smooth steady-state behavior, which cannot be achieved with fixed-gain PI control.

Table 1. Performance comparison of classical PI and AG-FOPI controllers

Performance Criterion	Classical PI	AG-FOPI
Settling time	~80 ms	~10 ms
(P/Q) Overshoot	high	Low to none
Steady-state error	Very low	Very low
Injected current THD (%)	~1.3%	~1.8%
Robustness against disturbances	Moderate	High
Coupling between P and Q	Slight	decoupled
Tuning complexity	Low	Moderate

Overall, the experimental results confirm that the AG-FOPI controller outperforms conventional PI control in dynamic performance, power quality, and robustness, making it a suitable solution for grid-connected PV applications.

6. Conclusion

This work proposed and experimentally validated an adaptive-gain fractional-order proportional–integral (AG-FOPI) control strategy for grid-connected photovoltaic (PV) systems. The controller was designed for the inner current loop to improve dynamic response and power quality under varying operating conditions. Hardware-in-the-loop (HIL) experiments were conducted using a TI F28379D digital control platform to assess the real-time performance of the proposed approach. The experimental results demonstrated fast and accurate tracking of active and reactive power references, with settling times below 10ms and negligible overshoot. In addition, the injected grid current exhibited low harmonic distortion, with THD values consistently below 1.8%, satisfying typical grid code requirements. Compared with conventional PI control, the AG-FOPI controller showed enhanced transient performance, improved robustness, and better decoupling between active and reactive power, while maintaining moderate implementation complexity suitable for real-time embedded systems. These results confirm the practical effectiveness of the proposed controller for grid-tied PV applications. Future work will focus on extending the proposed approach to three-phase systems and grid-disturbance scenarios.

7. References

- [1] J. Goldemberg and T. Johansson, *World Energy Assessment: Overview 2004 Update*. New York, NY, USA: United Nations Development Programme, 2004.
- [2] IEA, *Renewables 2023: Analysis and Forecast to 2028*. Paris, France: International Energy Agency, 2023.
- [3] M. A. Hasan, K. S. Hassan, and M. A. S. Masoum, “Grid integration challenges of photovoltaic systems: A review,” *IEEE Access*, vol. 8, pp. 10500–10516, 2020.
- [4] Y. Yang, F. Blaabjerg, and H. Wang, “Low-voltage ride-through of single-phase transformerless photovoltaic inverters,” *IEEE Transactions on Industry Applications*, vol. 50, no. 3, pp. 1942–1952, May–Jun. 2014.
- [5] IEEE Standard 1547-2018, *IEEE Standard for Interconnection and Interoperability of Distributed Energy Resources with Associated Electric Power Systems Interfaces*, IEEE, 2018.
- [6] H. Patel and V. Agarwal, “Control of a single-stage single-phase PV inverter with MPPT,” *IEEE Transactions on Energy Conversion*, vol. 24, no. 1, pp. 106–115, Mar. 2009.

- [7] D. Liu, W. Li, and X. Yuan, "Comparative study of classical PI and fractional-order PI controllers in power electronics converters," *IEEE Transactions on Power Electronics*, vol. 33, no. 3, pp. 2054–2063, Mar. 2018.
- [8] S. K. Panda and N. Senroy, "Adaptive fractional-order PI control for grid-tied PV inverter with load disturbances," *Control Engineering Practice*, vol. 75, pp. 90–100, 2018.
- [9] F. Zare, M. Moradi, and H. Mokhtari, "Robust fractional-order PI controller for grid-connected PV inverter with uncertainties," *Energy Conversion and Management*, vol. 197, Art. no. 111834, 2019.
- [10] L. Meng, J. S. Lai, and X. Han, "Sliding mode control for grid-connected PV inverters: Theory and implementation," *IEEE Transactions on Industrial Electronics*, vol. 67, no. 1, pp. 411–420, Jan. 2020.
- [11] T. N. Rao and S. K. Panda, "Backstepping control of three-phase grid-connected photovoltaic inverters," *International Journal of Electrical Power & Energy Systems*, vol. 99, pp. 113–120, 2018.
- [12] A. B. Al-Khafaji, H. A. Kazem, and S. M. Muyeen, "Artificial neural network-based control for renewable energy systems," *IEEE Transactions on Neural Networks and Learning Systems*, vol. 31, no. 4, pp. 1295–1305, Apr. 2020.
- [13] M. K. Gupta and R. K. Nema, "Fuzzy logic controller for solar PV inverter control: A review," *Renewable Energy*, vol. 147, pp. 2213–2228, 2020.
- [14] I. Podlubny, *Fractional Differential Equations*. San Diego, CA, USA: Academic Press, 1999.
- [15] J. Sabatier, O. P. Agrawal, and J. A. Tenreiro Machado, Eds., *Advances in Fractional Calculus: Theoretical Developments and Applications in Physics and Engineering*. Berlin, Germany: Springer, 2007.
- [16] H. R. Karimi, A. Sheikholeslam, and J. Kamwa, "Fractional-order control applications in renewable energy systems: A review," *Renewable and Sustainable Energy Reviews*, vol. 134, Art. no. 110329, 2020.
- [17] Y. Li and J. Chen, "Fractional-order PID controllers for grid-connected photovoltaic systems: Design and implementation," *IEEE Transactions on Industrial Electronics*, vol. 65, no. 12, pp. 9720–9729, Dec. 2018.
- [18] M. Taheri and M. R. Zolghadri, "PSO-based optimization of fractional-order controllers for grid-connected photovoltaic systems," *Solar Energy*, vol. 171, pp. 142–154, 2018.
- [19] S. Tahri, M. Amjoud, and A. Antar, "Real-time validation of advanced PV inverter controllers using hardware-in-the-loop platforms," *IEEE Access*, vol. 11, pp. 1700–1710, 2023.



Performance Evaluation of P&O, improved Sliding Mode and Fuzzy Logic MPPT Methods in PV Systems: A Comparative Study under uniform and non-uniform conditions.

Ahmed Chebri ^{1,*}, Fatima Zohra Boukahil ¹, Assala Mouffouk ¹, Boubekour Azoui ¹

¹ Renewable Energies and New Technologies Department, HNS-RE2SD, Batna, Algeria

*Corresponding author: (Ahmed Chebri), *Email Address*: chebri.ahmed.eng@gmail.com

Abstract

This paper presents a comprehensive comparative analysis of three Maximum Power Point Tracking (MPPT) algorithms Perturb and Observe (P&O), improved Sliding Mode Control (SMC), and Fuzzy Logic Control (FLC) applied to photovoltaic (PV) systems operating under both uniform irradiance and partial shading conditions. While uniform irradiance allows straightforward MPPT operation, variations caused by shading introduce nonlinearities in the power–voltage (P–V) characteristics that degrade performance and energy yield. The three MPPT techniques are implemented and evaluated in a simulated PV system using MATLAB/Simscape. Their performance is assessed using key metrics, including tracking efficiency, power losses (at the PV and load levels), and output power ripple. Results show that under uniform conditions, intelligent controllers (SMC and FLC) outperform conventional P&O by achieving faster convergence and improved output stability. Under partial shading, the disparity in algorithm performance becomes more pronounced, with FLC achieving the highest tracking accuracy (up to 99.8%), minimal ripple, and negligible power losses. The results reveal critical insights into the strengths and limitations of each method, providing guidance for optimal MPPT strategy selection in real-world solar energy applications.

Keywords: Photovoltaic (PV) systems; Maximum Power Point Tracking (MPPT); Partial shading; Fuzzy Logic Control (FLC); Sliding Mode Control (SMC); Perturb and Observe (P&O).

<https://doi.org/10.63070/jesc.2025.036>

Received 10 July 2025; Revised 06 November 2025; Accepted 06 December 2025;

Available online 24 December 2025.

Published by Islamic University of Madinah on behalf of *Islamic University Journal of Applied Sciences*.

This is a free open access article under the Creative Attribution (CC.BY.4.0) license.

1. Introduction

Climate change remains one of the most pressing global challenges, driven largely by greenhouse gas emissions from fossil fuel consumption. These emissions have led to rising global temperatures and an increased frequency of extreme weather events, threatening ecosystems and long-term human development. As conventional energy sources dwindle and their environmental impact becomes increasingly unsustainable, the transition to renewable energy is not only a necessity but a strategic imperative for global energy security and sustainable growth [1]. Among renewable technologies, photovoltaic (PV) systems stand out due to their modularity, declining costs, and environmental advantages. However, their power conversion efficiency remains highly dependent on external conditions—particularly solar irradiance. Under uniform irradiance (healthy conditions), PV systems typically exhibit a single, well-defined maximum on the power–voltage (P–V) curve, allowing conventional Maximum Power Point Tracking (MPPT) algorithms to operate effectively. In contrast, partial shading caused by clouds, buildings or trees introduces multiple local maxima on the P–V curve [2], significantly complicating the tracking of the Global Maximum Power Point (GMPP). This can result in suboptimal energy harvesting and even lead to module degradation due to hotspot formation. Given these challenges, this study investigates MPPT performance under both healthy and partially shaded conditions to provide a comprehensive analysis of system behavior across realistic scenarios. However, particular emphasis is placed on the partial shading case, due to its critical impact on system reliability and energy yield in real-world PV deployments. By examining both static and dynamic irradiance patterns, the paper aims to benchmark algorithmic effectiveness in overcoming the limitations of conventional MPPT strategies and enhancing overall system performance. MPPT algorithms are essential in PV systems to continuously adjust the operating point and ensure maximum energy extraction under both uniform and partial shading conditions. Conventional MPPT methods such as Perturb and Observe (P&O), hill climbing (HC) and Incremental Conductance (INC) are widely used for their simplicity and ease of implementation. However, under partial shading, their effectiveness is compromised due to their inability to distinguish local from global maxima on the P–V curve [3, 4]. To overcome these limitations, researchers have explored a range of intelligent and advanced control strategies. These include neuro-fuzzy structures [5], metaheuristic algorithms such as Particle Swarm Optimization (PSO) [6] and the Crow Search Algorithm (CSA), and hybrid methods like Grey Wolf Optimizer integrated with Fuzzy Logic Control (GWO- FLC) [7], GWO-PSO [8] and P&O-FLC [9]. Deep Reinforcement Learning (DRL) has also emerged as a promising solution due to its capacity for adaptive learning in dynamic environments [10]. Additionally, nonlinear and adaptive control strategies such as Sliding Mode Control (SMC) and Fuzzy Logic Control (FLC) have been

employed for their robustness and precision. SMC offers strong resilience against model uncertainties and abrupt irradiance changes, whereas FLC provides an intuitive, human-like decision mechanism that adapts well to complex behaviors without requiring a detailed mathematical model [11]. This paper presents a comprehensive evaluation of three Maximum Power Point Tracking (MPPT) algorithms Perturb and Observe (P&O), improved Sliding Mode Control (SMC), and Fuzzy Logic Control (FLC) applied to photovoltaic (PV) systems under uniform irradiance and partial shading conditions. The study is motivated by the performance limitations of traditional MPPT techniques in the presence of multiple local maxima on the power–voltage (P–V) curve caused by partial shading, which significantly complicates the tracking of the Global Maximum Power Point (GMPP). The modeling of the PV system and the analysis of its P–V characteristics under healthy and shaded conditions are presented in the second section. The third and fourth sections describe the simulation setup and provide a comparative performance evaluation of the three MPPT strategies under both static and dynamic irradiance patterns. Finally, the conclusion is presented in the last section, summarizing the key findings and proposing perspectives for future research.

2. PV system modeling and P-V characteristics

2.1 PV system architecture

To assess the effectiveness of different MPPT techniques in real-world operating conditions, a comprehensive simulation model of a PV energy conversion system is developed in MATLAB/Simscape. Figure 1 presents the overall architecture of a photovoltaic (PV) energy conversion system designed to evaluate and compare the performance of three MPPT algorithms Perturb and Observe (P&O), Fuzzy Logic Control (FLC), and an improved Sliding Mode Control (SMC) under both healthy and partial shading conditions.

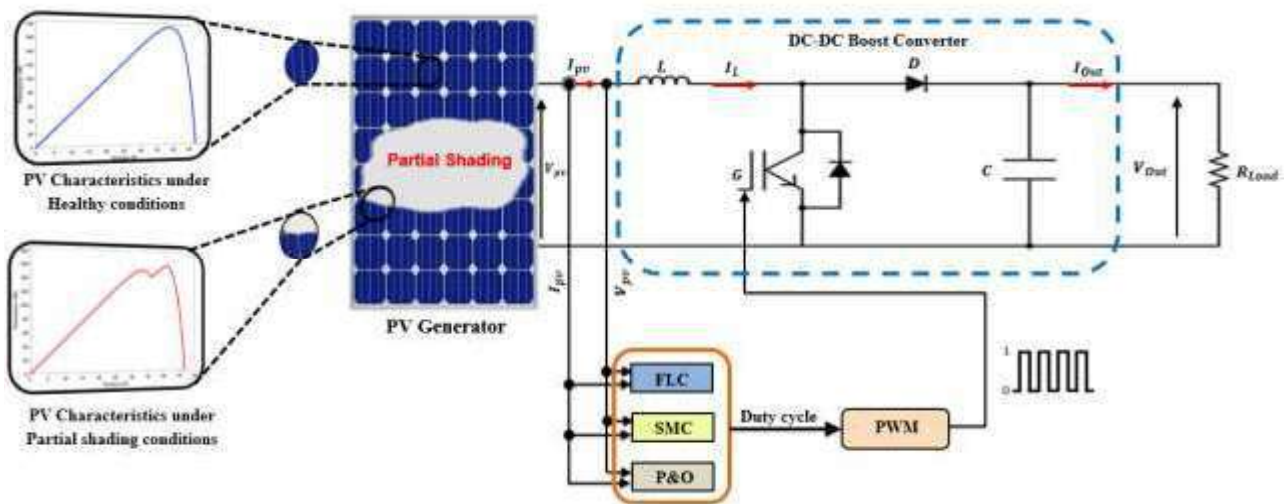


Figure 1. Block diagram of the PV system with MPPT control under healthy and partial shading conditions.

The PV generator is analysed under two separate irradiance scenarios: uniform irradiance (healthy case) the blue curve, where the power-voltage (P–V) curve exhibits a single, well-defined peak; and non-uniform irradiance (partial shading case) the red curve, where shaded cells introduce multiple local maxima, complicating the tracking of the global maximum power point (GMPP). A DC-DC boost converter is used to regulate the PV output, while the MPPT algorithms dynamically adjust the duty cycle signal applied to a PWM controller, enabling real- time adaptation to varying irradiance conditions for efficient power harvesting.

2.2 P–V characteristics under uniform irradiance

The P–V characteristics of the photovoltaic system under three uniform irradiance levels—1000 W/m² (blue), 900 W/m² (brown), and 800 W/m² (red)—are illustrated in Figure 2. In all cases, the curves maintain a single MPP, reflecting a healthy and uniformly irradiated PV array. As the irradiance level decreases, the output power drops proportionally, highlighting the strong dependency of PV performance on solar input. This reduction in irradiance leads to lower power generation, which must be considered during energy yield analysis and system design.

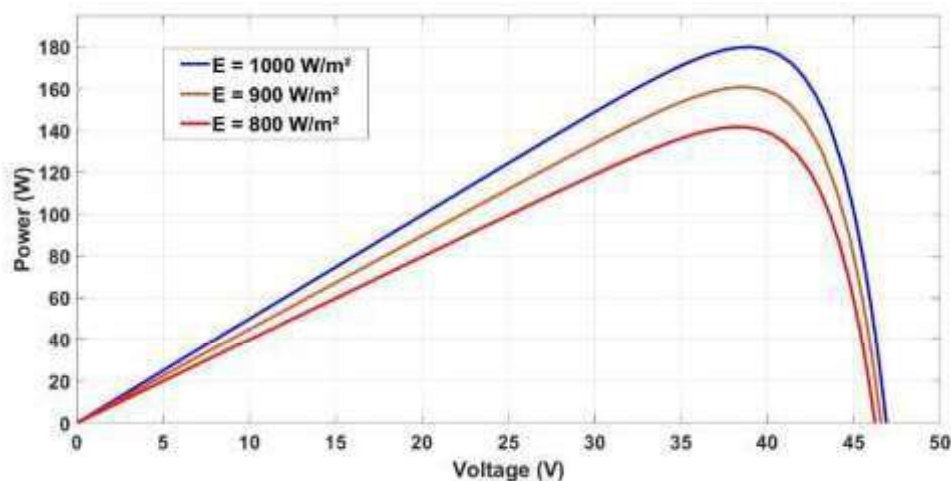


Figure 2. P–V Characteristics under Varying Irradiance Levels (Healthy Condition).

2.3 P–V characteristics under partial shading

The power–voltage (P–V) characteristics of the photovoltaic system under three distinct operating scenarios—a healthy uniform irradiance condition (blue curve) and two partial shading cases—are shown in Figure 3. Under healthy conditions, the curve exhibits a single, well-defined Maximum Power Point (MPP), indicating optimal operation without mismatch losses. In contrast, partial shading leads to multiple local peaks in the P–V curves due to uneven irradiance distribution across the PV modules, resulting in the formation of Local MPPs (LMPPs) and a Global MPP (GMPP). These multiple peaks highlight the challenges faced by conventional MPPT algorithms, which may become

trapped at a local maximum, thereby reducing energy harvesting efficiency. A noticeable reduction in the maximum extractable power is observed when comparing the GMPPs of the shaded cases with the healthy condition, quantifying the power losses induced by partial shading.

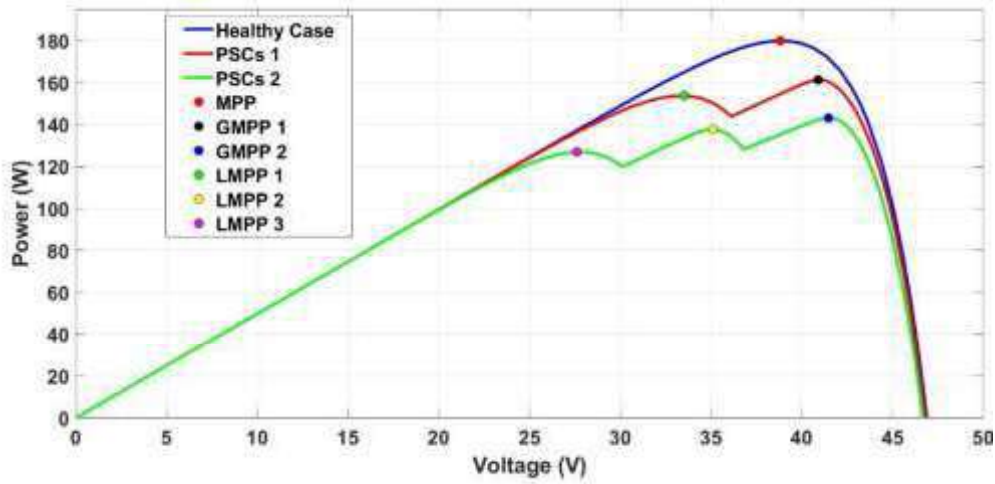


Figure 3. P–V characteristics of the PV system under uniform (healthy) and partial shading conditions.

3. Simulation framework and performance evaluation metrics

The performance of the proposed Maximum Power Point Tracking (MPPT) algorithms—Perturb and Observe (P&O), improved Sliding Mode Control (SMC), and Fuzzy Logic Control (FLC)—is evaluated through detailed simulations carried out in the MATLAB/Simscape environment. The photovoltaic (PV) energy conversion system consists of two BlueSolar SPP04090120 modules connected in series. The electrical characteristics of the PV module used in the simulations are summarized in Table 1.

Table 1. Electrical Parameters of the 90 W PV Module under Standard Test Conditions (STC).

Parameter	Value
Maximum Power (P_{MPP})	90 W
Voltage at MPP (V_{MPP})	19.5 V
Current at MPP (I_{MPP})	4.61 A
Open-Circuit Voltage (V_{OC})	23.44 V
Short-Circuit Current (I_{SC})	4.98 A

To assess the robustness and effectiveness of the MPPT techniques, two operating scenarios are considered: uniform irradiance (healthy condition) and non-uniform irradiance (partial shading

condition). These scenarios allow a comprehensive evaluation of the tracking capability, stability, and efficiency of each algorithm under realistic operating conditions.

Several key performance indicators are defined and calculated under both operating conditions to enable a quantitative comparison of the MPPT algorithms.

3.1 Tracking efficiency

Tracking efficiency quantifies the ability of the algorithm to deliver power close to the theoretical maximum available from the PV generator. It is calculated using the following expression:

$$\eta(\%) = \left(\frac{P_{Load}}{P_{PV}} \right) \times 100 \quad (1)$$

where (P_{Load}) is the power delivered to the load, and (P_{PV}) represents the measured PV power, defined as the maximum power point (MPP) under uniform conditions and the global MPP (GMPP) under partial shading.

3.2 Power losses

Power losses are evaluated in two stages to distinguish between tracking accuracy and conversion efficiency. Two types of losses are considered:

- **PV-side power losses**, defined as the difference between the theoretical maximum PV power and the tracked PV power:

$$P_{Loss,PV} = P_{PV(theoretical)} - P_{PV(tracked)} \quad (2)$$

- **Load-side power losses**, defined as the difference between the tracked PV power and the power delivered to the load:

$$P_{Loss,Load} = P_{PV(tracked)} - P_{Load} \quad (3)$$

3.3 Power ripple

Power ripple is used to measure the fluctuations in the output power during steady-state operation. It provides an indication of the stability and precision of the power extraction process. The formula for calculating power ripple is:

$$Power\ Ripple\ (\%) = \frac{P_{Max} - P_{Min}}{P_{Max}} \times 100 \quad (4)$$

Where (P_{Max}) and (P_{Min}) denote the maximum and minimum power values observed during steady-state operation, respectively. These performance indicators provide a comprehensive basis for evaluating the dynamic response, stability, and overall effectiveness of the MPPT algorithms under both uniform and partial shading conditions.

4. Simulation results and discussion

This section discusses the performance of the three MPPT algorithms—Perturb and Observe (P&O), improved Sliding Mode Control (SMC), and Fuzzy Logic Control (FLC)—applied to the photovoltaic system under both uniform irradiance and partial shading conditions. The objective is to interpret the dynamic and steady-state responses of each controller in terms of tracking accuracy, power stability, ripple magnitude, and energy losses, in order to identify the most suitable MPPT strategy for reliable and efficient photovoltaic energy conversion under realistic operating conditions.

4.1 Performance under uniform irradiance conditions

The dynamic behavior of the PV output power under variable irradiance conditions for the three evaluated MPPT algorithms—Fuzzy Logic Control (FLC), improved Sliding Mode Control (SMC), and Perturb and Observe (P&O)—is illustrated in Figure 4. The FLC method exhibits the most favorable response, characterized by fast convergence to the maximum power point and minimal oscillations, indicating strong dynamic performance and high tracking precision. The improved SMC algorithm also demonstrates robust operation, maintaining effective tracking with moderate oscillatory behavior. In contrast, the P&O algorithm displays inferior tracking stability, with evident power fluctuations and a tendency to deviate from the global maximum, reflecting limited adaptability to rapidly changing conditions.

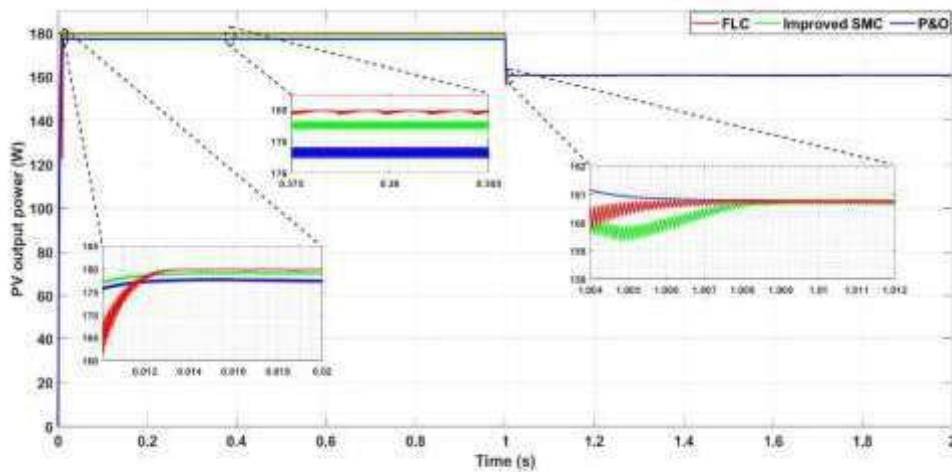


Figure 4. The PV output power of the three algorithms under varying irradiance conditions.

Figure 5 presents the corresponding load power profiles for the same MPPT strategies. Consistent with the PV output analysis, FLC ensures the most stable and reliable power delivery to the load, highlighting its superior capability in maintaining consistent operation under varying irradiance. While SMC and P&O both exhibit fluctuations in load power, the improved SMC achieves slightly enhanced steadiness compared to P&O, confirming its relatively better performance. Overall, FLC emerges as

the most effective technique in ensuring both accurate MPPT and stable power output, followed by improved SMC, with P&O showing the most pronounced limitations.

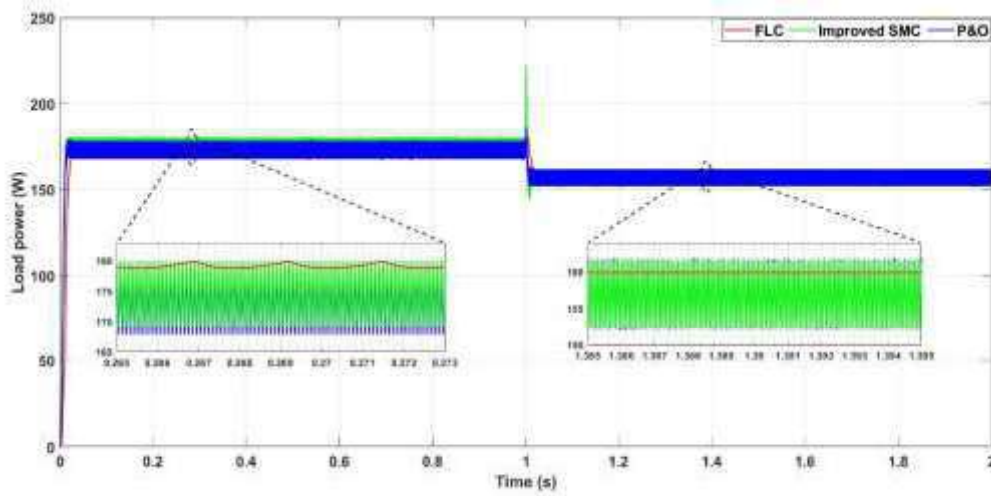


Figure 5. Load power response under partial shading conditions using P&O, FLC, and improved SMC algorithms.

4.2 Performance under partial shading conditions

Partial shading introduces multiple local maxima in the power–voltage characteristic, making MPPT significantly more challenging and increasing the risk of convergence to suboptimal operating points. The PV output power under partial shading is shown in Figure 6. The results indicate that both FLC and improved SMC effectively track the Global Maximum Power Point (GMPP), ensuring maximum energy extraction under non-uniform irradiance conditions. In contrast, the conventional P&O algorithm fails to reach the GMPP and instead settles near a Local Maximum Power Point (LMPP), resulting in reduced output performance.

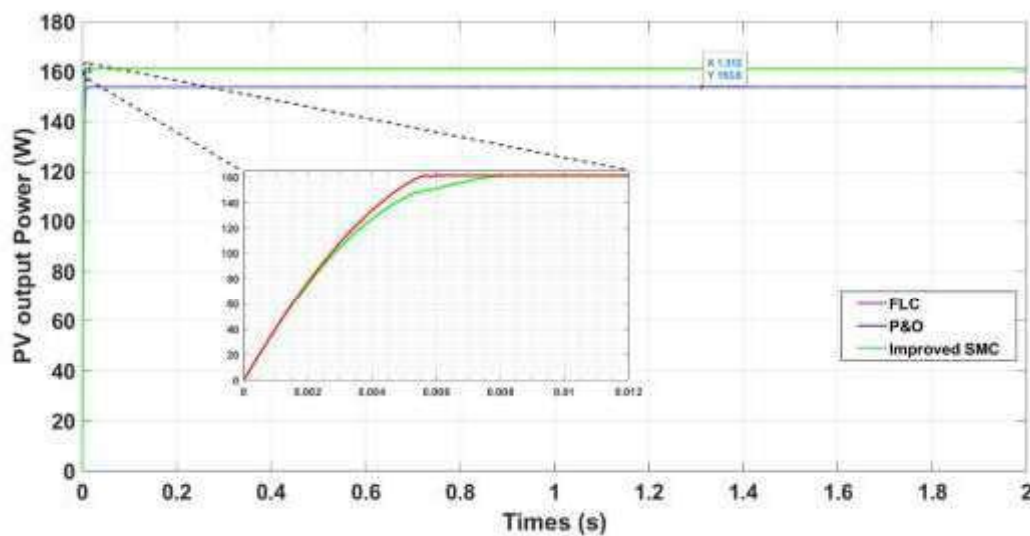


Figure 6. PV output power response under partial shading using P&O, FLC, and improved SMC.

The load power responses under partial shading are depicted in Figure 7. The FLC method maintains highly stable and smooth power delivery, with minimal oscillations around the steady state, confirming its accuracy and robustness in tracking the GMPP. The improved SMC algorithm also converges reliably to the GMPP, although minor power fluctuations are observed. On the other hand, the P&O approach exhibits noticeable oscillatory behavior and a lower average power output, reflecting its limitations in dynamic response and reduced efficiency under partial shading conditions.

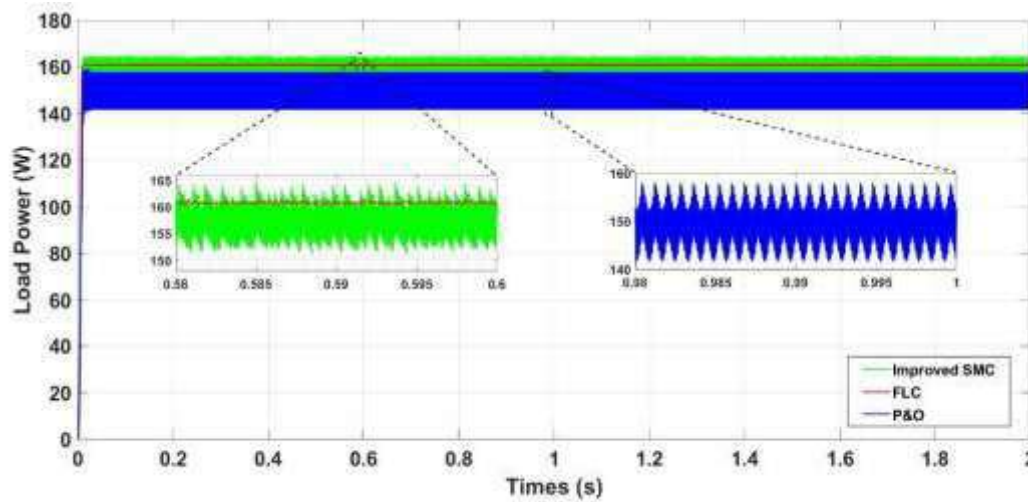


Figure 7. Load power performance under partial shading conditions using the P&O, improved SMC, and FLC algorithms.

4.3 Comparative performance evaluation

The comparative performance of the three MPPT algorithms is summarized in Table 2. Under healthy irradiance conditions, the classical P&O method records the lowest efficiency (90.24%) with significant power ripple (6%) and higher load losses (17.3 W), indicating its limitations in fast convergence and steady-state stability. In contrast, the intelligent FLC method achieves 99.6% efficiency, with negligible PV losses and a substantially reduced ripple of 0.6%, showcasing its superior ability to track the MPP with minimal dynamic fluctuations. The improved SMC approach also demonstrates strong performance, balancing high efficiency (97.5%) with moderate ripple (5.88%) and lower total losses compared to P&O. Under non-uniform irradiance conditions, which emulate realistic partial shading effects, the performance divergence becomes even more pronounced. The P&O algorithm fails to track the Global Maximum Power Point (GMPP) effectively, resulting in considerable PV power losses (7.6 W) and a decline in efficiency to 92.78%. Meanwhile, improved SMC maintains strong performance with 97.9% efficiency, moderate power losses, and controlled ripple. Once again, FLC exhibits the most robust and consistent behavior, sustaining 99.8% efficiency, virtually eliminating PV and load-side losses, and producing an exceptionally low ripple (0.18%), confirming its adaptability and high precision under rapidly changing and shaded conditions. This

comprehensive evaluation clearly highlights the limitations of conventional MPPT techniques like P&O in dynamic and shaded environments, while confirming the potential of intelligent controllers—particularly FLC—as powerful algorithms for maximizing energy extraction and ensuring system reliability in modern PV applications.

Table 2. Comparative performance of MPPT Algorithms under Healthy and Shaded Conditions.

	MPPT Algorithm	Efficiency (%)	Load Power (W)	Output PV Power (W)	Power losses (W)		Power ripple (%)
					PV losses	Load losses	
Healthy case	P&O	90.24	160	177.3	2.7	17.3	6
	Improved SMC	97.5	174.65	179.05	0.95	4.4	5.88
	FLC	99.6	179.35	180	Negligible	0.65	0.6
Shaded Case	P&O	92.78	149.75	153.8	7.6	4.05	0.03
	Improved SMC	97.9	158	161.3	0.1	3.3	0.14
	FLC	99.8	161	161.3	0.1	0.3	0.18

5. Conclusion and future work

This paper presented a comparative assessment of P&O, improved SMC, and FLC MPPT algorithms for photovoltaic systems under uniform and partial shading conditions. Simulation results demonstrated that intelligent controllers significantly outperform conventional P&O, particularly in shaded environments. Among the evaluated methods, FLC achieved the highest tracking efficiency (up to 99.8%), with negligible power losses and minimal ripple, ensuring fast convergence and excellent stability. Improved SMC also showed robust performance but with slightly higher oscillations. Overall, the findings confirm FLC as a highly effective and reliable MPPT solution for real-world PV applications, especially under complex and dynamic irradiance conditions. Future work will focus on experimental validation using real-time hardware platforms such as DSP or microcontroller-based systems, as well as the development of hybrid or adaptive MPPT strategies to further enhance performance under rapidly changing and complex shading conditions.

References

- [1] G. Upreti, "Climate change and its threat to humanity in the Anthropocene," in *Ecosociocentrism: The earth first paradigm for sustainable living*: Springer, 2023, pp. 137-162.

- [2] M. Ben Smida, A. T. Azar, A. Sakly, and I. A. Hameed, "Analyzing grid connected shaded photovoltaic systems with steady state stability and crow search MPPT control," *Frontiers in Energy Research*, vol. 12, p. 1381376, 2024.
- [3] D. Mazumdar, C. Sain, P. K. Biswas, P. Sanjeevikumar, and B. Khan, "Overview of solar photovoltaic MPPT methods: a state of the art on conventional and artificial intelligence control techniques," *International Transactions on Electrical Energy Systems*, vol. 2024, no. 1, p. 8363342, 2024.
- [4] S. A. Sarang *et al.*, "Maximizing solar power generation through conventional and digital MPPT techniques: a comparative analysis," *Scientific Reports*, vol. 14, no. 1, p. 8944, 2024.
- [5] I. Sajid *et al.*, "Optimizing photovoltaic power production in partial shading conditions using dandelion optimizer (DO)-based MPPT method," *Processes*, vol. 11, no. 8, p. 2493, 2023.
- [6] H. Ahessab, A. Gaga, and B. Elhadadi, "Enhanced MPPT controller for partially shaded PV systems using a modified PSO algorithm and intelligent artificial neural network, with DSP F28379D implementation," *Science Progress*, vol. 107, no. 4, p. 00368504241290377, 2024.
- [7] A. M. Eltamaly and H. M. Farh, "Dynamic global maximum power point tracking of the PV systems under variant partial shading using hybrid GWO-FLC," *Solar Energy*, vol. 177, pp. 306-316, 2019.
- [8] S. A. Taha, Z. S. Al-Sagar, M. A. Abdulsada, M. Alruwaili, and M. A. Ibrahim, "Design of an efficient MPPT topology based on a grey wolf optimizer-particle swarm optimization (GWO-PSO) algorithm for a grid-tied solar inverter under variable rapid-change irradiance," *Energies*, vol. 18, no. 8, p. 1997, 2025.
- [9] H. Karimi, A. Siadatan, and A. Rezaei-Zare, "A Hybrid P&O-Fuzzy-Based Maximum Power Point Tracking (MPPT) Algorithm for Photovoltaic Systems under Partial Shading Conditions," *IEEE Access*, 2025.
- [10] B. C. Phan, Y.-C. Lai, and C. E. Lin, "A deep reinforcement learning-based MPPT control for PV systems under partial shading condition," *Sensors*, vol. 20, no. 11, p. 3039, 2020.
- [11] M. H. Ali, M. Zakaria, and S. El-Tawab, "A comprehensive study of recent maximum power point tracking techniques for photovoltaic systems," *Scientific Reports*, vol. 15, no. 1, p. 14269, 2025.



A socio-economic Approach to Agricultural Drying Activities in the Ghardaïa Region of the Sahara

H.Bensaha,^{1*} A. Bemseddik¹, D. Daoud¹, A.Bensaha², Ammisaid², G. Hamdoun¹, L. Cheraa²

¹Unité de Recherche Appliquée en Energies Renouvelables, URAER, Centre de Développement des Energies Renouvelables, CDER, 47133, Algeria,

²University of Ghardaia, Algeria

*Corresponding author: (Hocine Bensaha), Email Address: muget78@gmail.com

Abstract

This study aims to analyse the socio-economic profile of agri-food producers and dryers in the Ghardaïa region of the Sahara, where agriculture is a fundamental pillar of rural livelihoods. Although agricultural drying is a relatively modest source of income and employment, it plays a significant role for smallholders and marginalised farmers, particularly among the most economically disadvantaged in the population. A stratified random sampling method was adopted to select producer-dryers from different areas of the region. Primary data were collected using structured interviews and pre-tested questionnaires administered during individual interviews. A total of 240 producer-dryers were surveyed in the study area. Statistical analysis of the data reveals that the majority of producer-dryers are women (76.7%), elderly (52.5%) and illiterate (63.4%). Around 64.1% have a farm of less than two hectares, and 61.6% are considered small farmers, cultivating less than one acre of farmland. Most respondents are engaged in subsistence farming, a field in which many have over 15 years' experience.

Keywords: Agricultural drying sector; Saharan agro-ecological zones; Local and cross-border trade dynamics; Subsistence farming; Socio-economic profile

<https://doi.org/10.63070/jesc.2025.037>

Received 10 July 2025; Revised 07 November 2025; Accepted 08 December 2025;

Available online 24 December 2025.

Published by Islamic University of Madinah on behalf of *Islamic University Journal of Applied Sciences*.

This is a free open access article under the Creative Attribution (CC.BY.4.0) license.

1. Introduction

Agriculture remains the backbone of the Algerian economy, with almost 60% of the population relying on it for their livelihood. Of the various agricultural and related activities, livestock farming is particularly important in rural areas (Amrani, 2004). It provides small and marginal farmers with a continuous source of income, employment, nutrition, and draught power. Livestock plays a particularly important role in the mixed farming systems that dominate much of rural Algeria (Benmihoub, 2015). Algeria has one of the largest agricultural territories in the world. It covers a wide variety of areas, including mountains, plains and fallow land, as well as areas dedicated to breeding cattle, buffalo, sheep and goats. According to the 2023 General Census of Agriculture (RGA), the country's agricultural land is structured in a particularly diverse way, including herbaceous crops, fallow land, fruit plantations, vineyards and natural grasslands. The south of the country is oriented towards Saharan and pastoral agriculture, with date and olive cultivation predominant, while the north is characterised by cereals, market gardening and citrus fruits (MADR, 2002 ; MADR, 2008).

Provided it is better leveraged, agricultural drying can offer significant employment opportunities and be a key source of income for rural populations (Bendjelid et al., 2004). In the Ghardaïa region, for example, it plays a crucial role in the rural economy, particularly for smallholder farmers and landless workers. Thanks to its adaptability to diverse agro-climatic conditions, relatively low investment requirements and rapid returns, it has become a sustainable source of income in this Saharan region (Adair et al., 2022). Drying practices play a fundamental role in the Algerian rural economy. They contribute to subsistence and food security and generate additional income for thousands of smallholder and marginalised farmers. Of the various techniques, open-air drying (also known as traditional drying) is notable for its low capital requirements, ease of execution, short processing time, and adaptability to a wide range of agro-climatic conditions (Bensaha et al., 2024).

The Saharan region of Ghardaïa, with its variety of agroclimatic zones, is one of the most important areas for Saharan agriculture in Algeria. Some areas of the region have become major centres for drying practices. The rural economy of the region relies heavily on agriculture and related activities. Goat farming is a key source of income, particularly for landless workers and marginal farmers. This sector supports rural households by providing them with a regular income through market gardening, date production and manure use (Cote, 2002).

The agricultural drying sector accounts for 5.63% of the Algerian government's gross value added, and 43.70% of the gross value added by the agricultural sector and related activities. Drying processes are often referred to as 'the poor's work' and are primarily associated with impoverished, landless or marginalised farmers. Drying fruits, vegetables and meat is one of the most profitable agricultural

activities in Saharan regions, providing many smallholder farmers and precarious agricultural workers with income, employment and food security. According to the 20th General Census of Agriculture (RGA), solar drying is particularly prevalent among small farms, especially for drying figs, tomatoes, and chilli peppers. In Ghardaïa, for instance, drying agricultural produce, particularly using solar power, is a common method of preserving fruit, vegetables, spices, and other produce. Therefore, this study focused on the drying practices of rural populations in this Saharan region. Understanding the socioeconomic profile of producers engaged in drying is essential for designing targeted interventions and policies that can improve productivity, sustainability, and livelihood security (Bensaha, 2022).

Socioeconomic factors such as level of education, farm size, drying methods used, income level and access to credit can have a significant influence on management practices and the profitability of agricultural drying. Despite the economic importance of this activity in the Ghardaïa region, there is limited empirical data available on the living conditions of producers involved in drying (Bensaha et al., 2020). This study aims to address this knowledge gap by analysing the socio-economic characteristics of producers in this Saharan region. The focus is on the demographic profile, resource availability and income structure of these producers, as well as the constraints and challenges they face in carrying out their activities. The results of this research will provide evidence-based policy recommendations to improve the socio-economic situation of agricultural drying producers in rural areas and promote the sustainable development of the agricultural drying sector in the Ghardaïa region.

2. Material and methods

This study was conducted in the Ghardaïa region, located 600 km south of the capital. It is a rural area with a Saharan climate, where agriculture and related activities constitute the main source of income for the majority of the population. This region is characterized by arid agriculture, red loamy soils, and a semi-arid climate, which are suitable for the breeding of small ruminants, particularly goats, as well as market gardening.

The survey was conducted through individual interviews. A proportional stratified random sampling procedure was adopted for data collection and analysis (Olivier de sardan, 2001). Data were collected from 240 producer-dryers using a pre-tested questionnaire. The interview guide was pre-tested with 15 producers from an area not included in the sample to ensure the questions were clear, relevant and consistent. Following this, minor adjustments were made to improve the instrument's fluidity and comprehensiveness.

The collected data was analysed statistically. The primary data collection was carried out through face-to-face interviews conducted by the researcher and trained field assistants. Each interview lasted

approximately 45 to 60 minutes and was conducted at the respondent's home or farmstead. Data collection was carried out during early mornings and late evenings to ensure that respondents were available and not engaged in farm or wage labour activities (Bousbia et al., 2024).

Age: This is the respondent's age, expressed in completed years, at the time of the interview. Age is a determining factor that influences the availability of labour, the experience of producer-dryers and their willingness to adopt modern technologies.

Sex: It refers to the gender of the respondent who takes care of the goats. The respondents were categorized into male and female. Gender distribution in goat farming often reflects broader socio-cultural patterns in rural.

Education: This refers to the highest level of formal education successfully completed by the respondent, whether through school or university. Educational attainment plays a key role in raising awareness and improving the effectiveness of management and the adoption of scientific practices in agricultural drying.

Occupation of the respondent: This is the occupation that the respondent was engaged in in order to support themselves at the time of the survey. This variable indicates whether the farmer relies primarily or partially on their production for income. It also provides information on labour availability, risk diversification and income-generating potential. In rural areas of Algeria, particularly in regions such as Ghardaïa, drying is often practised alongside farming, wage labour, or other subsistence activities. This activity is defined as follows:

Primary occupation: This is the occupation from which more than 50% of the respondent's family income is generated. This enables us to identify the main source of income for the household and gain a better understanding of economic dependence, professional priorities and financial stability.

Secondary occupation: This is a profession that is practised alongside the main activity, providing an additional source of income for the respondent's household. This secondary activity enables us to evaluate the economic diversification of households, which is often crucial for enhancing their resilience in the face of economic or climatic hazards.

Farm size: This is the total quantity of dried products that the respondent's household produced at the time of the interview. Farm size is a key indicator of the scale and intensity of drying activities. It reflects the producer's economic situation, their capacity to invest, the availability of land and labour, and their dependence on the crop as a source of livelihood.

Experience in agricultural drying: This is the total number of years of direct experience that the respondent had in agricultural drying at the time of the interview. This experience is crucial for developing management practices, improving productivity and ensuring the sustainability of farms. It also reflects farmers' traditional knowledge, practical skills and adaptability in management.

3. Results and discussion

Gender

The result revealed that majority women (76.7 %) are engaged in goat farming than men (23.3%), Since men are involved other agriculture related practices. This finding is in line with Mosher (2017), Bensaha et al., (2019) reported that rural women played an important and substantial role in goat farming.

Age

The majority of drying producers (52.5%) are in the over-50 age group, while those in the 31–50 age group represent 38.8%, and those in the under-30 age group represent 8.7%. This distribution can be explained by the low involvement of the younger generation in drying practices. This finding is consistent with previous observations, which report that the majority of agricultural producers are in the older age groups (Bensaha et al., 2015).

Education

Literacy is one of the important factors which accelerates development and progress of any enterprise. The results revealed that 63.4 per cent were illiterate, whereas only 22.9 per cent of goat farmers were educated up to the secondary level. It also showed that 10.8 per cent of the goat farmers educated up to primary level and meagre numbers of graduates were involved in goat farming (2.9 %). The present finding is in agreement with the findings of Bensaha et al., (2019), Rouabhi et al., (2016).

Primary occupation

Agricultural drying is the main occupation for 73.3% of respondents, with agriculture and related activities coming in second place at 26.7%. These results are consistent with those of Ref., who also found that agricultural drying is not only the main activity, but also an important source of income — and for some farmers, a supplementary one (Bensaha et al., 2016).

Landholding

According to their landholding capacity, the majority of dry producers were smallholders (61.6%), followed by medium-sized farmers (26.7%), landless farmers (9.2%) and, lastly, large-scale farmers (2.5%). These results contrast with those of Bensaha et al., 2017, who found that the majority of dry producers in the north of the country (87.9%) and the steppe region (86%) were landless agricultural workers.

Farm size

In Algeria, the quantity of agricultural produce intended for drying varies significantly depending on the size of the farm and the capacity of the producer. The results of the survey showed that the majority of respondents (64.1%) produced "medium" quantities of products intended for drying. Meanwhile,

23.8% were classified as small producers and only 12.1% as large producers. Participants reported a total quantity of dried products ranging from 6 to 25 quintals, with an estimated average of 12 quintals per producer (Addoun et al., 2023).

This distribution reflects the predominance of medium-sized producers in the agricultural drying sector, which is representative of the general structure of agriculture in several Algerian regions, particularly rural areas in the north and the highlands. It also indicates limited production capacity, which is linked to factors such as land availability, access to drying equipment and investment levels. These results highlight the importance of supporting small and medium-sized producers, who constitute the majority of those involved in this activity, in order to improve yields and the quality and overall profitability of dried products.

Source of purchase of dry products

In the study area, the majority of producers involved in drying activities (49.2%) reported primarily using their own harvests as the raw material. This self-sufficiency reflects the direct addition of value to agricultural production, a practice commonly observed among small and medium-sized farmers in Algeria. Meanwhile, 34.6% of respondents sourced fresh produce from local traders, indicating the existence of an additional supply market for drying. Finally, 16.2% of producers reported using a mixture of products from their own production and external sources (MADR, 2012 ; Bensaha , 2022). This mixed supply method demonstrates flexibility within Algeria's agricultural drying value chain, where producers adapt their practices according to seasons, agricultural yields and market accessibility. It also highlights the partial dependence of some producers on commercial channels to ensure business continuity, particularly during periods of low production (Bensaha et al., 2019).

Experience in agricultural drying

Data analysis revealed that the majority of agricultural drying producers (47.1%) had between 21 and 30 years' experience in the field. Respondents with 11–20 years' experience represented 35.4%, while those with over 30 years' experience accounted for 11.3%. In contrast, only 6.2% of producers reported having less than 10 years' experience. The average experience of all participants was 16.39 years, with a range of 1–42 years.

These results demonstrate that agricultural drying in the study area is primarily rooted in traditional expertise acquired and passed down over many years. This highlights the importance of this practice in local agricultural customs, particularly in rural areas of Algeria, where it is both a preservation method and a sustainable source of income. However, the low proportion of young or recently engaged producers in this activity may also indicate a lack of generational renewal, possibly due to the sector's limited appeal to young people or the absence of suitable support mechanisms (Bensaha et al., 2024 ; Kherrafi et al., 2023).

4. Conclusion

In the Saharan region of Ghardaïa in Algeria, agricultural drying represents a promising way to promote sustainable agriculture, foster rural development and empower women and young farmers. Thanks to its adaptability to local climatic conditions and economic viability, as well as the growing demand for dried products, this sector offers considerable potential.

Effective extension services and the dissemination of scientific knowledge on good drying practices could raise awareness among local populations, improve farm productivity and ensure the sustainability of rural farmers' livelihoods.

The study results show that the quantity of dried products could be significantly increased by adopting improved techniques, helping to meet producers' needs and raise their socioeconomic status. The majority of producers appear to be smallholders with limited education and land resources, for whom drying is an essential source of supplementary income, particularly for the most vulnerable households. Women play a particularly significant role in this sector, reflecting their central position in managing family farms in the region. However, despite this potential, the sector faces several challenges, particularly with regard to disease management, the availability of plant protection products, and the lack of organised marketing structures.

The study highlights the need for targeted public policies, capacity-building programmes and improved access to finance to sustainably improve the living conditions of dry-farm producers in the Ghardaïa region.

5. References

- [1] Adair, P., Lazreg, M., Bouzid, A., & Ferroukhi, S. A. (2022). L'agriculture algérienne: l'héritage du passé et les défis contemporains. *Les cahiers du Cread*, 38(3), 413-440.
- [2] Addoun T, Hadeid M, Bensaha H, Zegait R. (2023). A New Dynamic of Saharan Agricultural Transformation: Thermal Area of Zelfana (Southern Algeria). *Agric. conspec. sci.* Vol. 88 No. (1). 75-84
- [3] Amrani, K. (2024). Durabilité des agrosystèmes oasiens: évaluation et perspectives de développement.. Cas de la palmeraie de Ouargla (Algérie). *Les Cahiers d'EMAM. Études sur le Monde Arabe et la Méditerranée*.
- [4] Bendjelid A., Brûlé J.-C., Fontaine J. (dir.), (2004). *Aménageurs et aménagés en Algérie. Héritages des années Boumediene et Chadli*, Paris, L'Harmattan.

- [5] Benmihoub A (2015). « 50 ans de réformes du foncier agricole étatique en Algérie, une rétrospective », Options méditerranéennes, série B, no 72, p. 53-70.
- [6] Bensaha H, Abdelhakem S and Bensaha L, (2015). Impact of Foreign Labor on the Dynamics and Sustainability of Agricultural Production Units, Case of Ghardaia Region (Algeria Northern Sahara). Research Journal of Applied Sciences, Engineering and Technology, 10(4): 408-413.
- [7] Bensaha H, Arbouche R. Impact de la dynamique de l'agriculture et ses conséquences sur la durabilité de l'écosystème saharien: cas de la vallée de M'zab (Sahara septentrional). Revue Marocaine des Sciences Agronomiques et Vétérinaires. Vol. 4, No 3 (2016).
- [8] Bensaha H, Bensaha A, Daoud D, Benseddik A and Lalmi D (2024). Marketing of Dried Agricultural Products: What Socio-Economic Opportunities for the Saharan Regions? 2024 IEEE International Multi-Conference on Smart Systems & Green Process (IMC-SSGP), Djerba, Tunisia, 2024, pp. 1-7, doi: 10.1109/IMC-SSGP63352.2024.10919797.
- [9] Bensaha H, Benseddik A, Lalmi D, and Kherrou S (2019). Sanitary assessment of an agricultural greenhouse equipped with thermal storage system in the Ghardaïa Region. AIP Conference Proceedings 2190, 020096 (2019);<https://doi.org/10.1063/1.5138582>.
- [10] Bensaha H, Benseddik A, Lalmi D, Arbouche R. (2020). Around the Drying Practice and Developmental Improvement Proposal in Algerian Northern Sahara: Case of the Saharan Regions. TEST Engineering & Management. The Mattingley Publishing Co., Inc. Vol.83. p24359 – 24371
- [11] Bensaha Hocine (2022). Le séchage solaire est-il une alternative de valorisation des fruits et légumes déformés ? Bulletin des Energies Renouvelables N° 53. 06-07 p
- [12] Bensaha Hocine. 2022. Les pandémies mondiales : stratégie de l'utilisation des énergies renouvelables dans le secteur hydro-agricole. Bulletin des Energies Renouvelables. Numéro :52. Page.5
- [13] Bensaha, H., Bensaha, Y., Bensaha, L., Arbouche, L., (2017). Overview of agricultural policies for access to agricultural land modes in the region of Ghardaia (Algeria). Int. J. Curr. Res. Biosci. Plant Biol. 4(3), 88-92. doi: <https://doi.org/10.20546/ijcrbp.2017.403.010>
- [14] Bensaha, H., Benseddik, A., Lalmi, D., Zegait, R., Arbouche, R. (2019). Dried Products and Sustainable Development in Saharan Regions: The Case of Ghardai'a in the M'zab Region of Algeria. Arab World Geographer, 22(4), pp. 333–343
- [15] Bousbia, A., Gueroui, Y., Aouadi, A., Teweldebirhan, M. D., Bessa, R. J. B., Symeon, G., & Boudalia, S. (2024). Typology analysis of cattle farms in Northeast Algeria: Potential for sustainable development. Agricultural Systems, 218, 103995.

- [16] Côte M., (2002). « Des oasis aux zones de mise en valeur : l'étonnant renouveau de l'agriculture saharienne », Méditerranée, t. 99, no 3-4, p. 5-14.
- [17] DOI : 10.3406/medit.2002.3253
- [18] <http://www.maxwellsci.com/jp/abstract.php?jid=RJASET&no=553&abs=08>
- [19] Kherrafi, M. A., Benseddik, A., Saim, R., Bouregueba, A., Badji, A., Nettari, C., ... & Bensaha, H. (2023). Performance enhancement of indirect solar dryer with offset strip fins: Experimental investigation and comparative analysis. *Solar Energy*, 266, 112158.
- [20] MADR. (2002). La nouvelle politique de développement agricole et rural : Choix stratégiques, mise en oeuvre et perspectives. Ministère de l'agriculture et du développement rural. Alger
- [21] MADR. (2008). Le Renouveau de l'Economie Agricole & le Renouveau Rural. Ministère de l'agriculture et du développement rural. . Alger
- [22] MADR. (2012). Le Renouveau agricole et rural en marche, revue et perspectives". Alger: Ministère de l'Agriculture et du Développement Rural.
- [23] Mosher, A. T. (2017). The development problems of subsistence farmers: a preliminary review. *Subsistence agriculture and economic development*, 6-11.
- [24] Olivier de Sardan J.-P., (2001). « Les trois approches en anthropologie du développement », *Revue Tiers Monde*, t. 42, no 168, p. 729-754. http://www.persee.fr/doc/tiers_1293-8882_2001_num_42_168_1546
- [25] Rouabhi, A., Mekhlouf, A., Mokhneche, S., & Elkolli, N. (2016). Farming transitions under socioeconomic and climatic constraints in the southern part of Sétif, Algeria. *Journal of Agriculture and Environment for International Development (JAEID)*, 110(1), 139-153.



Advanced Network Voltage Control for Grid-Connected PV Systems Using Smart PV Inverter Capabilities

Ismail Bendaas ^{*1}, Salim Bouchakour ¹, Kada Bouchouicha ¹, Saliha Boulahchiche ¹, Abdelhak Razagui ¹, Amar Hadj Arab ¹, Smail Semaoui ¹, Kamel Abdeladim ¹.

¹ Centre de Développement des Energies Renouvelables Algiers, Algeria.

i.bendaas@cder.dz, s.bouchakour@cder.dz, k.bouchouicha@cder.dz, s.boulahchiche@cder.dz, a.razagui@cder.dz, a.hadjarab@cder.dz, s.semaoui@cder.dz, k.abdeladim@cder.dz

*Corresponding author: Ismail Bendaas, *Email Address:* i.bendaas@cder.dz

Abstract

Photovoltaic (PV) systems integrated into low-voltage distribution networks (LVDNs) can induce voltage violations, raising concerns regarding their penetration limits. Although grid-connected PV systems (GCPV) offer advantages such as reduced production costs and enhanced efficiency, managing their voltage impact remains essential. To mitigate the need for grid reinforcements, distribution network operators must develop innovative control strategies that facilitate cost-effective PV integration. Advanced control techniques, including volt-watt control (VWC), volt-var control (VVC), and their coordinated combination (VWC-VVC), can effectively manage voltage violations by absorbing or injecting reactive power, or by curtailing active power output. This study evaluates inverter performance in GCPV systems subject to considerable voltage fluctuations due to high PV penetration. Real operational data from a GCPV system at the Centre for Renewable Energy Development (CDER) validate the proposed simulation methodology. Results demonstrate the effective application of PV inverters for LVDN integration and quantify the benefits of enhanced voltage management achieved through VWC and VVC functionalities.

Keywords: Advanced Control capabilities; Grid-connected PV system; Network voltage control; Smart PV inverters; Voltage violations.

<https://doi.org/10.63070/jesc.2025.038>

Received 10 July 2025; Revised 08 November 2025; Accepted 09 December 2025;

Available online 24 December 2025.

Published by Islamic University of Madinah on behalf of *Islamic University Journal of Applied Sciences*.

This is a free open access article under the Creative Attribution (CC.BY.4.0) license.

1. Introduction

Several conventional resources face limitations or phase-out due to environmental issues. Renewable energy sources such as wind, solar, hydropower, and biomass will become increasingly crucial. In Algeria, solar energy is now increasingly available by solar plants connected to the medium voltage grid [1][2]. GCPV have an influence on: the protection policy, the energy quality, or the voltage violation due to a high PV penetration [3][4]. However, the characteristics, operation, and disturbances of the distribution network can affect the performance of PV systems. Depending on the capabilities and connection points of the PV generators and the network characteristics, the voltage at the node can fluctuate and may frequently exceed the acceptable limits ($\pm 10\%$) as defined by standards such as EN 50160, VDE 0126-1-1, and IEC 61727 [5][6][7]. A variety of approaches presented in the literature have successfully addressed the issue of voltage violation in LVDNs. Some suggest increasing cable diameter to lower line impedance, however this is not economically possible. Furthermore, these approaches are insufficient for responding to changing operational circumstances or external disruptions such cloud cover. On-load tap-changing transformers (OLTC) are a more practical option for changing tap positions and controlling voltage levels. The main limitation of these systems is that their control functions discretely and on a slower period of minutes, rendering them unsustainable in locations with high PV penetration and rapid cloud transients witnessed on a timescale of seconds[8][9]. To mitigate the issue, [10][11] propose integrating OLTC with fast-response devices including Battery Energy Storage (BES) and D-STATCOM. However, these approaches may improve system-wide performance, their real-time deployment and economic viability are uncertain due to the communication infrastructure requirements and the time necessary to tackle the majority of these issues. However, we focus on VWC and VVC capabilities, which are generally faster, easier to implement, and capable of responding to sudden external disturbances in GCPVs. Among the many functions of PV inverter, voltage reactive power control and voltage active power control have attracted attention due to their efficiency. We used these two advanced functionalities in this work to improve voltage violations in an LVDN. The advantages of improved voltage control in LVDN when PV inverters use new control strategies such as VWC and VVC are well known and have previously been investigated in the literature by works [8][9]. Consequently, this study focuses on the inherent capabilities of smart PV inverters, namely Volt-Watt Control (VWC) and Volt-Var Control (VVC). These functionalities are generally faster, easier to implement, and capable of responding to sudden external disturbances in GCPV systems. Among the many functions of a PV inverter, voltage-reactive power control and voltage-active power control have attracted significant attention due to their operational efficiency for local voltage management.

The main contribution of this work lies in the development and evaluation of a novel coordinated control strategy, combining the VWC and VVC functionalities of smart inverters. Unlike isolated applications of these controls, our generic VWC-VVC approach aims to orchestrate the entire fleet of inverters on the network to optimize voltage regulation. It is specifically designed for critical scenarios of high PV penetration and low demand, where overvoltage is most likely. The mechanism prioritizes reactive power adjustment VVC first; when this proves insufficient, it progressively activates active power curtailment VWC. This prioritization maximizes energy injection while ensuring compliance with voltage standards. The effectiveness of this strategy, as well as conventional VWC and VVC methods, is rigorously tested through simulations based on real load and solar profiles from Algeria, applied to a standard IEEE network model. Thus, this study proposes methodologies directly applicable to strengthening the integration of PV systems into Algerian low-voltage networks. The study aims to assess the effectiveness of PV inverters in mitigating voltage violations under high PV penetration. It focuses on an Algerian LV network context that faces significant voltage fluctuations and load demand variations. Real monitored data from the Centre de Développement des Energies Renouvelables (CDER) forms the basis of a detailed case study, with the LV distribution network modeled after the IEEE European test feeder in OpenDSS software.

2. Voltage sensitivity analysis

The power flow solution determines voltage amplitudes, phase angles, active and reactive power flows, and losses across all network buses, assuming balanced stability conditions and using phase analysis with a positive sequence system representation. This analysis is crucial for network planning, operation, economic scheduling, utility energy exchange, and various studies including stability and contingency analysis. Voltage sensitivity analysis helps identify the most efficient locations and amounts of reactive power support from solar inverters to maintain network voltage. Solving power flow requires formulating complex linear equations connecting bus voltages and currents through an admittance matrix, as depicted in equation (1).

$$[V_{bus}] = Y_{bus}^{(-1)} [I_{bus}] \quad (1)$$

The bus admittance matrix $[Y_{bus}] = [Z_{bus}]^{(-1)}$ is fundamental in electrical systems, representing the inverse of impedance. In practice, powers are more known than currents. Thus, replacing the current vector in equation (1) with power vectors forms nonlinear equations solved via the Newton-Raphson method. Solving for powers Eq (2) and (3) yields the voltage sensitivity matrix S. The Jacobian matrix is updated iteratively until convergence, and its inversion computes S [10]. Figure 1 illustrates a two-bus power flow.

$$P_i = |V_i| \sum_{j=1}^{N_{bus}} |V_j| |Y_{ij}| \cos(\theta_{ij} - \delta_i + \delta_j) \quad (2)$$

$$Q_i = -|V_i| \sum_{j=1}^{N_{bus}} |V_j| |Y_{ij}| \sin(\theta_{ij} - \delta_i + \delta_j) \quad (3)$$

$$\begin{bmatrix} \Delta\theta \\ \Delta V \end{bmatrix} = \begin{bmatrix} S_{\theta P} & S_{\theta Q} \\ S_{VP} & S_{VQ} \end{bmatrix} \begin{bmatrix} \Delta P \\ \Delta Q \end{bmatrix} \quad (4)$$

$$S = \begin{bmatrix} S_{\theta P} & S_{\theta Q} \\ S_{VP} & S_{VQ} \end{bmatrix} = J^{-1} \quad (5)$$

where i is the index of a three-phase bus in a balanced network, The green color denotes the nominal voltage zone (1.0 pu). The ANSI/IEEE-style diagram illustrates a simplified two-bus LV network

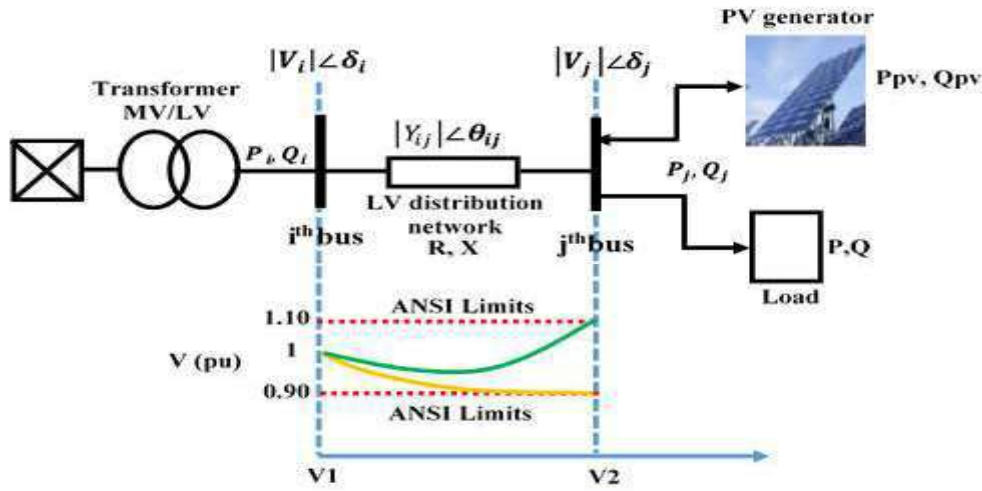


Figure 1. Effects of voltage increase in LVDN

3. Control capabilities of smart PV inverters

GCPV systems use inverters to convert DC power to AC for grid connection. These inverters can also control voltage at the point of common coupling (PCC) by altering reactive power or reducing active power [12]. Inverters' rated capacity limits their ability to inject or absorb reactive power, as determined by the following condition:

$$\sqrt{P_{out}^2 + Q_{inj}^2} \leq S_{rated} \quad (6)$$

S_{rated} : Inverter apparent power rating

3.1 Active power control

Active power curtailment reduces the inverter's generated active power, lowering the PV voltage at the PCC without actively altering the reactive power output. Users can set individual active power

output points (x, y) for various voltage levels (see Figure 2). When the network's maximum voltage exceeds 10% of the nominal level as defined by EN50160, active power is limited to P_{\max} . This limit is determined by points (V1, P1) and (V2, P2) on a given curve:

$$P_{\max} = \begin{cases} P_1 & ; V < V_1 \\ P_1 - \frac{(V - V_1)(P_1 - P_2)}{(V_1 - V_2)} & ; V_1 < V < V_2 \\ P_2 & ; V > V_2 \end{cases} \quad (7)$$

The actual PV inverter operation is limited by available solar PV resources giving:

$$P_{out} \leq P_{APC} = \min(P_{\max}, P_{avail}) \quad (8)$$

VWC strategies are employed during high distribution-level penetration, when high PV output and low loads cause voltage to rise excessively.

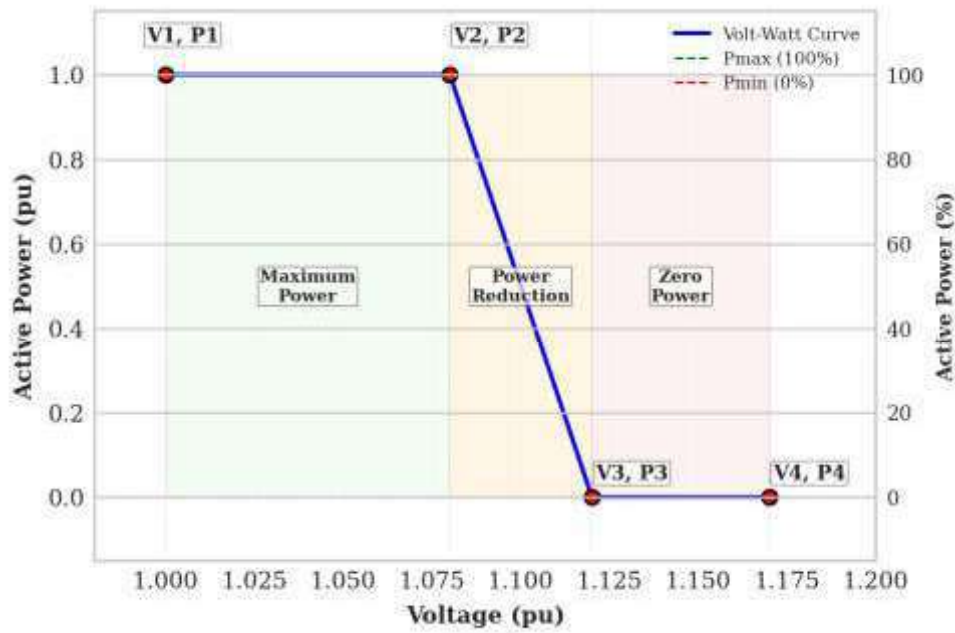


Figure 2. Typical curve of Volt-Watt voltage control

3.2 Reactive power control

The volt-var functionality ensures that the PV system voltage remains within EN50160 standards despite changing conditions. Reactive power exchange begins when the voltage exceeds a set upper limit (as shown in Figure 3). Conversely, if the voltage drops below the rated level, the inverter can inject reactive power into the distribution network to help stabilize them. Users can designate many points in a volt/var curve to select the angle points (V1, Q1), (V2, Q2), (V3, Q3), and (V4, Q4), (Qop) denotes reactive power exchange: negative for absorption, positive for injection Figure 3.:

$$Q_{op} = \begin{cases} Q_1 & V > V_1 \\ Q_1 + \frac{(V - V_1)(Q_2 - Q_1)}{(V_2 - V_1)}; & V_2 < V < V_1 \\ Q_2 + \frac{(V - V_2)(Q_3 - Q_2)}{(V_3 - V_2)}; & V_3 < V < V_2 \\ Q_3 + \frac{(V - V_3)(Q_4 - Q_3)}{(V_4 - V_3)}; & V_4 < V < V_3 \\ Q_4; & V > V_4 \end{cases} \quad (9)$$

Achieving desired reactive and active power operating points simultaneously may be limited by the inverter's rated apparent power, ensuring compliance with Eq (10).

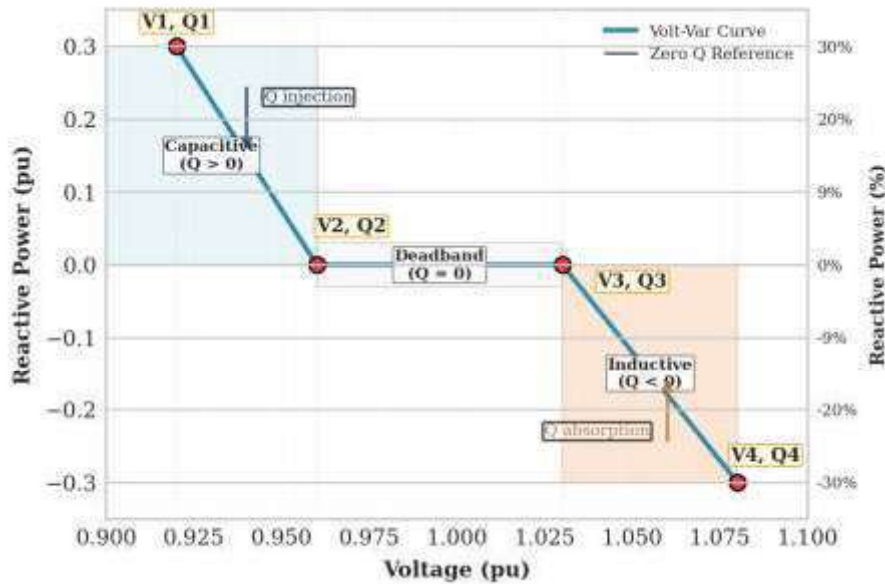


Figure 3. Typical curve of Volt-Var voltage control

3.3 Design of proposed coordination approach

The new approach investigates the interaction of two parameters: an active control voltage target level (V2) and an overvoltage threshold for Reactive Power Control (VVC) (V1). Using hierarchical control, separate sets of V1 and V2 are defined for various PV inverters along the feeder in a coordinated and efficient way. Figure 4. shows the suggested VWC-VVC control strategy for an inverter to solve overvoltage issues. According to references [13], the VVC algorithm may be ineffective for voltage control at the feeder's end when reactive power exchange is limited to specified voltage levels. In contrast, VWC improves voltage control methods. According to the proposed VWC-VVC algorithm: The inverter's reactive power is defined by the expression (10) and (11):

$$Q = \begin{cases} 0 & V \leq V_1 \\ Q_0 + \frac{(Q_{\max} - Q_0)(V - V_1)}{(V_2 - V_1)}; & V_1 < V \leq V_2 \\ \text{Change_to APC} & V > V_2 \end{cases} \quad (10)$$

$$P = \begin{cases} P_{\max} + \frac{(P_{\text{out}} - P_{\max})(V - V_2)}{(V_3 - V_2)}; & V_2 \leq V \leq V_3 \\ P_{\text{out}}; & V > V_3 \end{cases} \quad (11)$$

$$\begin{cases} Q_{\text{inj}} = Q_0 + \frac{(Q_{\text{out}} - Q_{\max})}{(V_3 - V_1)} ; V > V_2 \\ P_{\text{out}} = \sqrt{S_{\text{rated}}^2 - Q_{\text{inj}}^2} \end{cases} \quad (12)$$

According to, when line voltages exceed V_2 and reactive power exchange is exhausted, the control strategy shifts from VVC to VWC. Reactive power injected to maintain voltages above V_2 is calculated using equation (12). Adjustments in active power output follow based on the calculated injected reactive power. If line voltage drops below V_2 , the strategy reverts to VVC from VWC. This VWC-VVC approach enhances PCC level voltage control and enhances inverter capacity utilization across network points by managing injected reactive power for voltage control while curtailing active power.

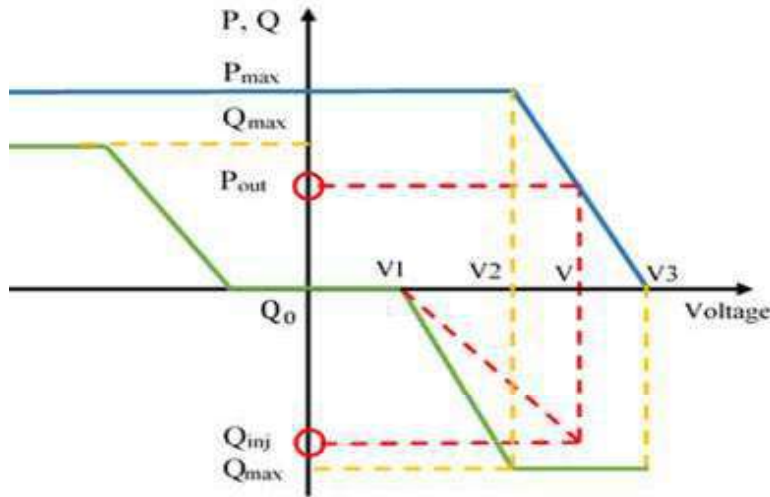


Figure 4. Typical curve of coordinate VWC-VVC voltage control

4. Voltage network control under integration of PV systems

An illustrative case study is presented to demonstrate how the advanced features of new PV inverters can be utilized to enhance the integration of a PV plant into an existing LVDN with high PV penetration.

4.1 Distribution network

To assess the PV system's impact on the LV distribution network, various power flow simulation tools are available, capable of solving both balanced and unbalanced distribution grids effectively. Standardization across platforms is crucial for comparative analysis. IEEE provides defined test feeders that include essential electrical components for analyzing voltage impacts in GCPV systems, usable across different software platforms.

Table 1. Summary of LV European test feeder left and right variables used in the simulations.

Grid characteristic	
Four-wire wye	Type of Feeder
residential	Type of settlement
906	Number of line
11, 0.416	Nominal voltage (kV)
800/800	Transformer rated power (kVA)
radial	Grid topology
1.5	Average distance between transformer and houses (km)
2c*007, 2c*0225, 2c*16, 35-SAC-XSC, 4c*06, 4c*1, 4c*35, 4c*185, 4c*70, 4c-95-SAC-XC	Feeder cable types

This study utilized the IEEE LV European Test Feeder, a three-phase radial grid with 0.416 kV nominal voltage and 50 Hz frequency, connected to an 11 kV medium voltage system via an 0.8 MVA step-down transformer [14]. Figure 5 depicts our representation of the IEEE network's single-line diagram. The network comprises 906 nodes and 55 single-phase loads distributed across three phases at 0.23 kV with a power factor of 0.95 in a Wye connection. The model was implemented using OpenDSS, an open-source software for electricity distribution systems developed by EPRI. Table. 1. show our variables used in simulations.

4.1 PV power and load profiles

Algerian data was used to create load profiles over a 24-hour period with 5-minute measurement intervals. Based on a day in July 2020, a specific type of load profile was generated (referring to July 7, 2020). This information is derived from the CDER monitoring system. The load profile and the power generated by the PV generator, are shown in Figure 6.

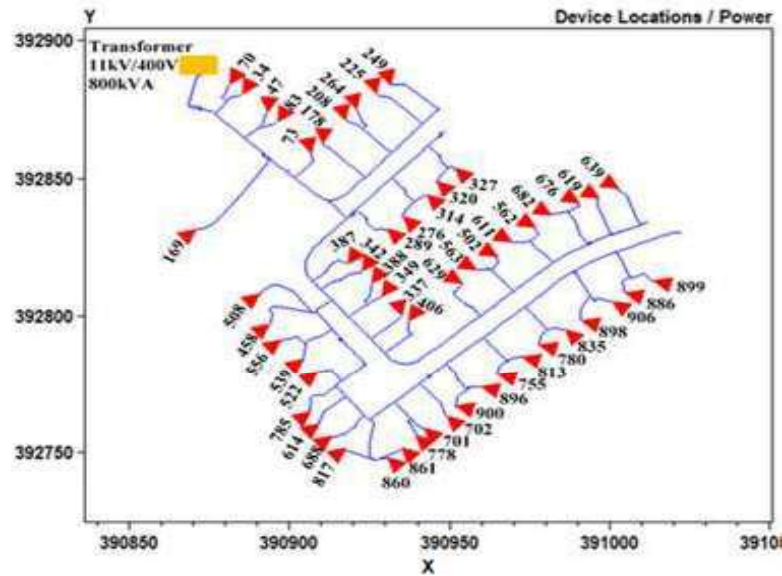


Figure 5. Single line diagram of the European LV test feeder

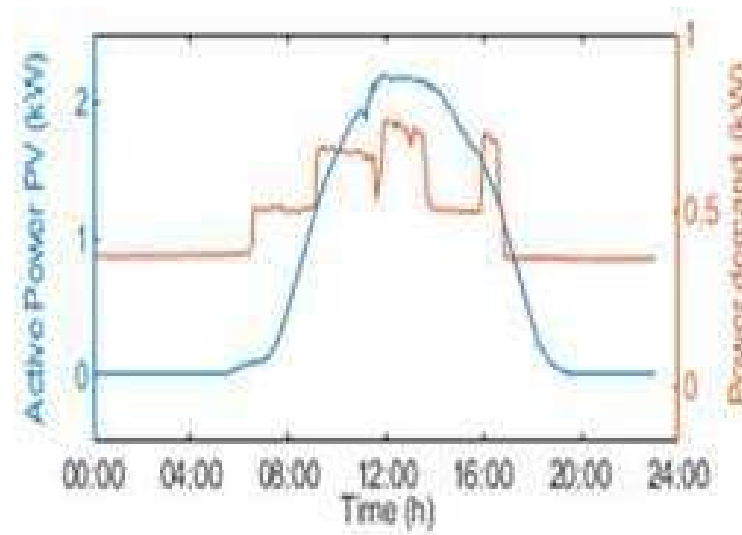


Figure 6. Daily load and PV profile

5. Results and discussions

To demonstrate the impact of GCPVs, the study used input data from the described demand load and PV generation for power-flow analysis of the test network. The stochastic nature of consumer load demand was simplified by using a generalized daily load curve for all consumers. Each GCPV system had a consistent output profile, with individual PV power limited to 2.16 kW. Figure 6 illustrates the PV output and generalized load demand curves. Scenarios included simulations with and without PV installations, and with/without voltage control. Increasing numbers of randomly connected GCPV generators were tested to identify voltage violations (voltage exceeding 1.10 pu). OpenDSS software

performed successive 5-minute interval load flow calculations (288 intervals per day) on the LV network, using the Newton-Raphson algorithm to address flow problems.

5.1 PV system's impact on the LV test network

The study focused on an LV distribution network (LVDN) under extreme conditions, depicted in Figure 5. Details on the network modeling are in Section 4.

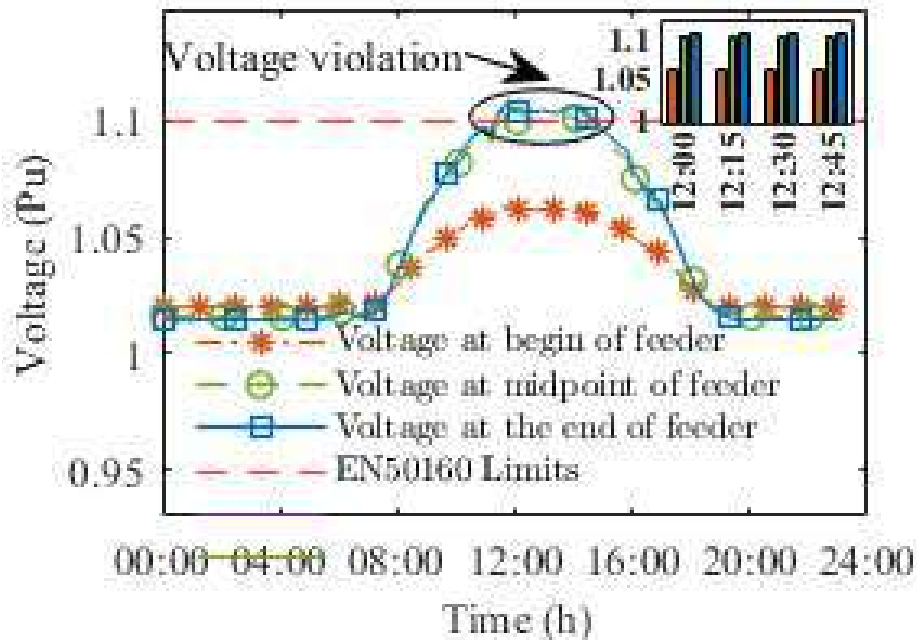


Figure 7. Daily voltage profile

Table. 2 summarizes the different voltage values at the different network PCCs.

Table 2. LV voltage variation under deferent PV penetration

Penetration (%)	Max LV Voltage at beginning of feeder (Pu)	Max LV Voltage at midpoint of feeder (Pu)	Max LV Voltage at the end of feeder (Pu)
0%	1,0198	1,0159	1,0145
10%	1,0206	1,0176	1,0163
25%	1,0226	1,0215	1,0202
35%	1,0243	1,0249	1,0238
50%	1,0268	1,0299	1,0293
100%	1,0350	1,0465	1,0472
200%	1,0507	1,0779	1,0808
280%	1,0628	1,1021	1,1068

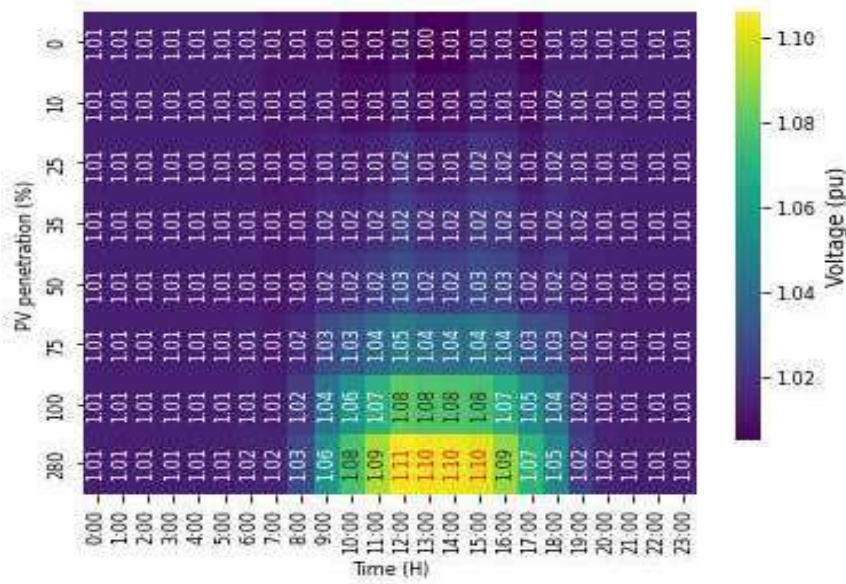


Figure 8. Heatmaps voltage violations at the end of feeder

The network includes a randomly dispersed set of single-phase PV systems connected to various customers. PV generator penetration levels were varied to assess their impact on voltage levels, guided by EN50160 standards. The transformer operates without an on-load tap-changer (OLTC), maintaining a fixed voltage configuration. Voltage profiles at different network nodes (start, middle, end) and voltage violation heatmaps at the PCC level are illustrated in Figure 7 and Figure 8. These figures highlight voltage violations occurring at maximum PV penetration levels, particularly at the feeder's end (Figure 7).

5.2 Mitigation of overvoltage

Therefore, to enhance the technical performance of GCPV systems using advanced photovoltaic inverter capabilities, this study incorporates the control strategies detailed in Section 4. These voltage control methods are applied to address voltage violations across the entire LV network, which is balanced with 55 GCPVs and 55 loads. By integrating of all PV arrays at maximum penetration causes voltage exceedances at the feeder end. For a detailed analysis of each method's effectiveness in mitigating PCC voltage violations, refer to Figure 9a, Figure 9b and Figure 9c. All three methods demonstrate significant improvements in local voltage control. Notably, the coordinated VVC and VWC-VVC strategies exhibit reduced voltage fluctuations compared to VWC approaches alone.

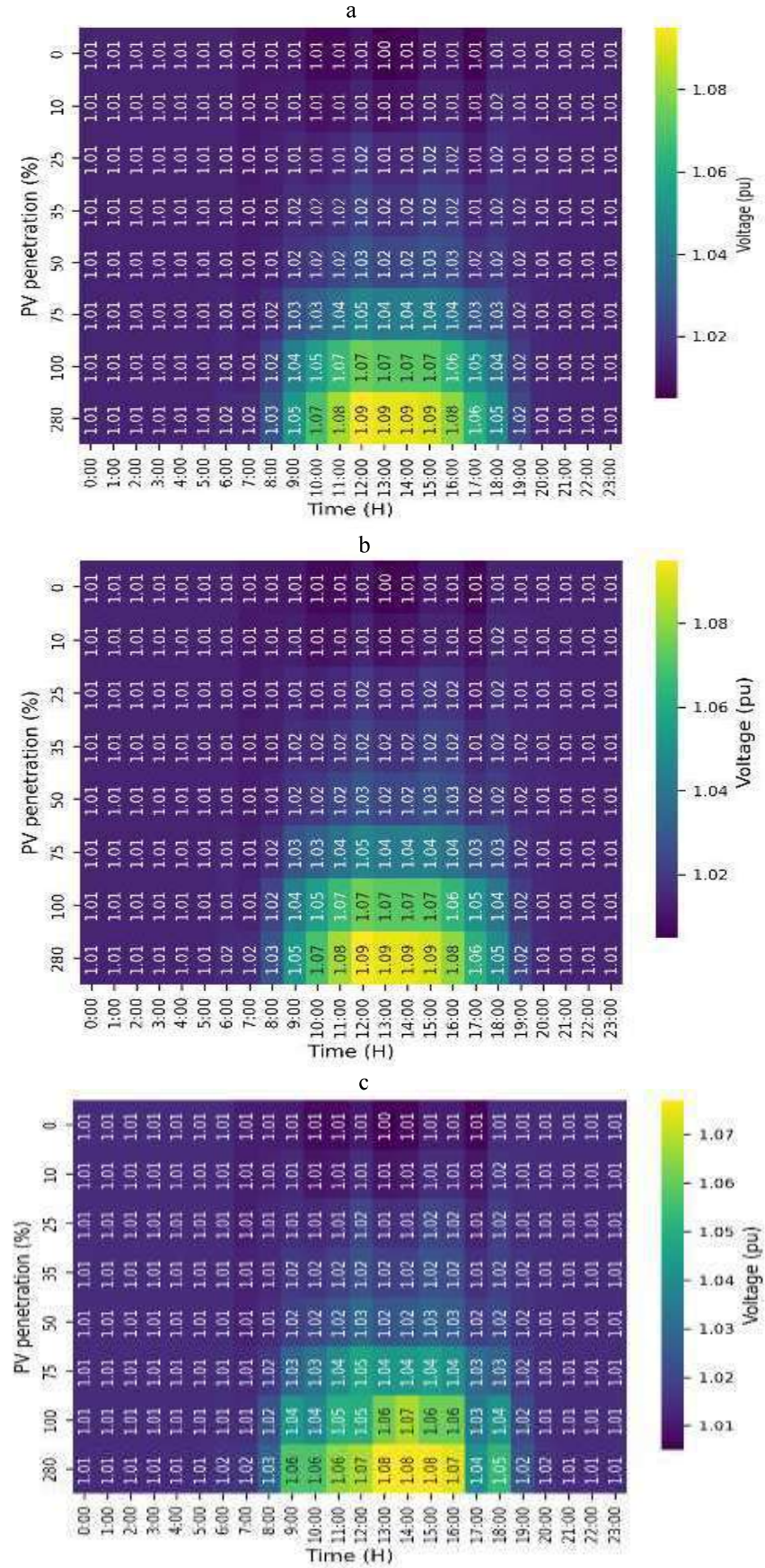


Figure 9. Mitigation of voltage violation a) Heatmaps of VWC control. b) Heatmaps of VVC control. c) Heatmaps of VWC-VVC control.

6. Conclusion

With the increased deployment of GCPVs, overvoltage at the PCC becomes a major issue. This study discusses voltage control enhancements for GCPVs with enhanced PV inverter capabilities. Three decentralized voltage control approaches VWC, VVC, and a proposed coordinated VWC-VVC strategy are used based on simulated models. When voltage violations detected, these methods cause reactive power absorption or injection while limiting active power injection to ensure conformity with EN50160 standards. However, a significant disadvantage is their potential inefficiency in using the full capacity of PV inverters, particularly those located further away from transformers working at higher capacities than those closer. The results of this study are useful for distribution system operators who are comparing the VWC-VVC approach to local control approaches. Proposals to standardize advanced PV inverter functionalities in the Algerian grid aim to improve existing systems.

References

- [1] I. Bendaas, K. Bouchouicha, S. Semaoui, A. Razagui, S. Bouchakour, S. Boulahchiche, Performance evaluation of large-scale photovoltaic power plant in Saharan climate of Algeria based on real data, *Energy Sustain. Dev.* 76 (2023) 101293, doi: 10.1016/j.esd.2023.101293.
- [2] Bendaas et al., Monitoring Assessment of a Large-Scale Solar Power Plant in Algeria's desert Climate, *Proc. - 2025 3rd Int. Conf. Electron. Energy Meas. IC2EM 2025*, 2025, doi: 10.1109/IC2EM63689.2025.11101224.
- [3] S. Boulahchiche et al., PERFORMANCE INVESTIGATION OF SINGLE-PHASE TRANSFORMERLESS PV INVERTER CONNECTED TO LOW VOLTAGE NETWORK, *Rev. Roum. DES Sci. Tech. — SÉRIE ÉLECTROTECHNIQUE ÉNERGÉTIQUE* 69(1) (2024) 55–60, doi: 10.59277/RRST-EE.2024.1.10.
- [4] S. Boulahchiche et al., Impact of a power ramp event on photovoltaic system power quality under different weather conditions and operating powers, *Electr. Eng.*, 2024, doi: 10.1007/s00202-024-02467-9.
- [5] E. Demirok, P.C. González, K.H.B. Frederiksen, D. Sera, P. Rodriguez, R. Teodorescu, Local reactive power control methods for overvoltage prevention of distributed solar inverters in low-voltage grids, *IEEE J. Photovoltaics* 1(2) (2011) 174–182, doi: 10.1109/JPHOTOV.2011.2174821.
- [6] J. Widén, E. Wäckelgård, J. Paatero, P. Lund, Impacts of distributed photovoltaics on network voltages: Stochastic simulations of three Swedish low-voltage distribution grids, *Electr. Power Syst. Res.* 80(12) (2010) 1562–1571, doi: 10.1016/j.epsr.2010.07.007.
- [7] I. Bendaas et al., Effect of a New Smarts Photovoltaic Inverters Connected with a Distribution Networks in Algeria, in: *SIENR 2021 - 6th International Symposium on New and Renewable Energies*, IEEE, 2021, doi: 10.1109/SIENR50924.2021.9631923.
- [8] R. Tonkoski, L.A.C. Lopes, T.H.M. El-Fouly, Coordinated active power curtailment of grid connected PV inverters for overvoltage prevention, *IEEE Trans. Sustain. Energy* 2(2) (2011) 139–147, doi: 10.1109/TSTE.2010.2098483.

- [9] C.V. Chandran, M. Basu, K. Sunderland, S. Pukhrem, J.P.S. Catalão, Application of demand response to improve voltage regulation with high DG penetration, *Electr. Power Syst. Res.* 189 (2020) 106722, doi: 10.1016/j.epsr.2020.106722.
- [10] L. Xiaohu, A. Andreas, L. Liming, L. Hui, Coordinated Control of Distributed Energy Storage System With Tap Changer Transformers for Voltage Rise Mitigation Under High Photovoltaic Penetration, *IEEE Trans. Smart Grid* 3(2) (2012) 897–905.
- [11] S. Khan, P. Zehetbauer, R. Schwalbe, Evaluation of sensitivity based coordinated volt-var control and local reactive power for voltage regulation and power exchange across system boundaries in smart distribution networks, *Electr. Power Syst. Res.* 192 (2021) 106975, doi: 10.1016/j.epsr.2020.106975.
- [12] I. Bendaas et al., Impact of Maximum PV Penetration on the Voltage Violation in Grid-Connected PV System, in: B.S. Adel Mellit, H. Belmili (Eds.), *Proceedings of the 1st International Conference on Advanced Renewable Energy Systems*, Springer, Singapore, 2024, pp. 167–176, doi: 10.1007/978-981-99-2777-7_19.
- [13] S. Pukhrem, M. Basu, M.F. Conlon, K. Sunderland, Enhanced network voltage management techniques under the proliferation of rooftop solar PV installation in low-voltage distribution network, *IEEE J. Emerg. Sel. Top. Power Electron.* 5(2) (2017) 681–694, doi: 10.1109/JESTPE.2016.2614986.
- [14] K.P. Schneider et al., Analytic Considerations and Design Basis for the IEEE Distribution Test Feeders, *IEEE Trans. Power Syst.* 33(3) (2018) 3181–3188, doi: 10.1109/TPWRS.2017.2760011.



Experimental Investigation on Vapor Condensation and Removal in a Box Solar Cooker Using a Pressure Cooker Integrated with a Flexible Pipe

Lobna Reciouï¹, Yettou Fatiha², Amor Gama^{3,*}

¹ Material, Energy Systems Technology and Environment Laboratory, Faculty of Science and Technology, Université de Ghardaïa, BP 455, 47000 Ghardaïa, Algeria

² Unité de Recherche Appliquée en Energies Renouvelables, URAER, Centre de Développement des Energies Renouvelables, CDER, 47133, Ghardaïa, Algeria

³ Unité de Recherche Appliquée en Energies Renouvelables, URAER, Centre de Développement des Energies Renouvelables, CDER, 47133, Ghardaïa, Algeria, gama.amor@gmail.com

Abstract

Solar cookers represent an environmentally friendly and sustainable technology for cooking applications, as they rely on solar energy, a clean, renewable, and widely available resource. This study investigates the effect of vapor condensation on the glass cover of a solar box cooker and its impact on thermal efficiency. Experimental investigations were conducted through controlled stagnation and sensible heat tests under two operating configurations: a conventional simple cooking pot and a pressure cooker equipped with a flexible pipe to vent steam outside the cooker enclosure. Experimental results showed that, when using the simple pot, vapor condensed on the inner surface of the glass cover, leading to reduced solar transmittance, increased thermal losses, and a gradual decrease in absorber plate temperature. In contrast, the pressure cooker configuration successfully discharged steam through the flexible pipe, preventing condensation on the glass surface and maintaining stable absorber temperatures during operation. The thermal performance of the cooker was evaluated using standard figures of merit, which were determined to be 0.11 m²C/W and 0.427. These findings confirm that mitigating vapor condensation improves thermal performance and demonstrate that integrating a pressure cooker with an external steam-release system enhances solar box cooker efficiency and reliability.

Keywords: Solar box cooker; Pressure cooker; Flexible pipe; Thermal performance.

<https://doi.org/10.63070/jesc.2025.039>

Received 10 July 2025; Revised 10 November 2025; Accepted 11 December 2025;
Available online 24 December 2025.

Published by Islamic University of Madinah on behalf of *Islamic University Journal of Applied Sciences*.
This is a free open access article under the Creative Attribution (CC.BY.4.0) license.

1. Introduction

Cooking serves as a significant and routine component of household life. The reliance on fossil sources such as LPG, Coal, and gas for cooking has major environmental, health, and socioeconomic impacts. While these fuels are convenient and energy-dense, they contribute to air pollution, climate change, and public health issues, particularly in low- and middle-income nations where access to clean energy is limited. By harnessing solar energy, solar cookers heat and cook meals without the need for electricity or gas. This sustainable technique reduces fuel costs, minimizes pollution, and is ideal for sunny regions. Solar cookers come in different designs, such as parabolic cookers, where by harnessing sunlight to convert it into heat at a point to cook food (Mekonnen et al, Maurice Ky et al) [1,2], and indirect cooking using a fluid to transfer the heat through it into the cooking chamber (Hosseinzadeh et al) [3]. A hybrid solar cooker incorporates base solar energy with another energy source, for instance, electricity, biomass, and LPG (Saxena and Agarwal; Reciouei et al) [4, 5]. Each is suited for various cooking needs (Yettou et al) [6]. Solar cooking requires abundant insolation and clear weather to succeed in the cooking operation. Nevertheless, these dependencies can limit its reliability in regions with frequent cloud cover or seasonal variability. Solar box cookers are insulated enclosures with transparent covers that admit sunlight. Under optimal conditions, solar box cookers achieve steady-state temperatures ranging from 120°C up to 150°C, a thermal regime particularly suited for slow-cooking methods, including boiling, steaming, and stewing. Tawfik et al [7] constructed an inclined box cooker that was incorporated with a parabolic reflector. Furthermore, an evaluation was performed to examine the thermal efficiency in both scenarios: with a parabolic reflector and without one, and the authors revealed that the cooker recorded an intermediate temperature of about 140–150 °C and overall efficiency with and without a parabolic reflector to be 10.7% and 12.5%, and additionally, lessen cooking time by 36 min. Goyal and Eswaramoorthy [8] analyzed and tested a solar box oven. Where use an optimized cooking container incorporated with a triangular fin affixed to its exterior surface, aimed at augmenting the process of heat transfer through convection. The results of the simulation indicated that heat losses were in the top, bottom, and side 4.26, 0.77, & 0.64 W/m², and at experiments the box oven achieved in the test load (1.5 Kg) a cooking power was 77.06 W, and efficiency augmented from 36.16 % up to 40.55 % and reduce cooking time from 95 min to 85 min hence the augmentation of the surface area of a cooking vessel through the implementation of a triangular fin configuration significantly enhances the convective heat transfer. Verma et al [9] constructed and developed a solar box oven comprising two identical parts and conducted a comparative study by utilizing black matt paint and five material mixed paints such as CuO, TiO₂

(titanium oxide), activated carbon (copper oxide), Tungsten, and mica mixing with black paint on the absorber tray in order ameliorate the thermal performance of the cooker. Furthermore, experimental tests were performed with a water load and without it by using different coating materials. Titanium oxide TiO_2 and Mica blended with paint were proven effective in enhancement by ameliorating 5-7 °C, and during tests without load gave the absorber plate difference of about 1-14°C, and water load difference of about 1-7 °C for two box ovens. Ademe and Hameer [10] performed and assessed a box cooker with a glazing wiper mechanism. Furthermore, the cooker was tested with and without the wiper mechanism. The results indicated that the figures of merit, standard cooking power, and the boiling duration of 1.43 kg of water fresh in mode without vapor mechanism were 0.123 Km^2/W , 0.540, 36 W, and 88.84 minutes, as well as in mode with vapor mechanism were 0.123 Km^2/W , 0.827, 51 W, and 53.54 minutes respectively. Goyal and Eswaramoorthy [11] analyzed and tested a box cooker that used the waste marble pieces as integrated sensible thermal storage to enhance the potential of evening cooking. The researchers proposed which uses sensible heat storage (marble) with an aluminum sheet cover, matte black coated, and without. The aluminum was used under glass to reduce top heat losses. The experimental findings, a power and efficiency without sheet cover and with were 56.62 W, 48.21 W, 25.79 %, and 31.19 %, respectively, as well as the sheet cover can lessen top heat losses and marble as a heat storage capable in evening cooking. Based on most literature reviews of the relevant, which particularly utilized methods and techniques to optimize the performance of a cooker, the enhancements, also modifications, involved particularly the cooking pot, coating, reflectors, and wiper mechanism to reduce vapor on the glass. In this research work, a thorough experimental investigation was carried out on a box cooker, with emphasis on the integration of a flexible pipe system designed to minimize or prevent vapor condensation on the indoor surface of the glass cover, thereby improving the overall thermal efficiency and visibility during operation.

<https://doi.org/10.63070/jesc.2025.xxx>

Received xxxx 2025; Revised xxxx 2025; Accepted xxxx 2025.

Available online xxxx 2025.

Published by Islamic University of Madinah on behalf of *Islamic University Journal of Applied Sciences*. This is a free open access article under the Creative Attribution (CC.BY.4.0) license.

2. Materials and Methods

2.1 Description of System

The experiment was conducted using a Box solar cooker, which was evaluated both with a cooking container & without it. The cooking vessels utilized in the experiment included a simple cooking pot and a pressure cooker. Figure 1 demonstrates a trial procedure of the solar cooker, which incorporates a flexible pipe connected to the vent pipe of the pressure cooker, facilitating the release of vapor through it. The readings have been recorded by the measuring instruments and are stated in Table 1.

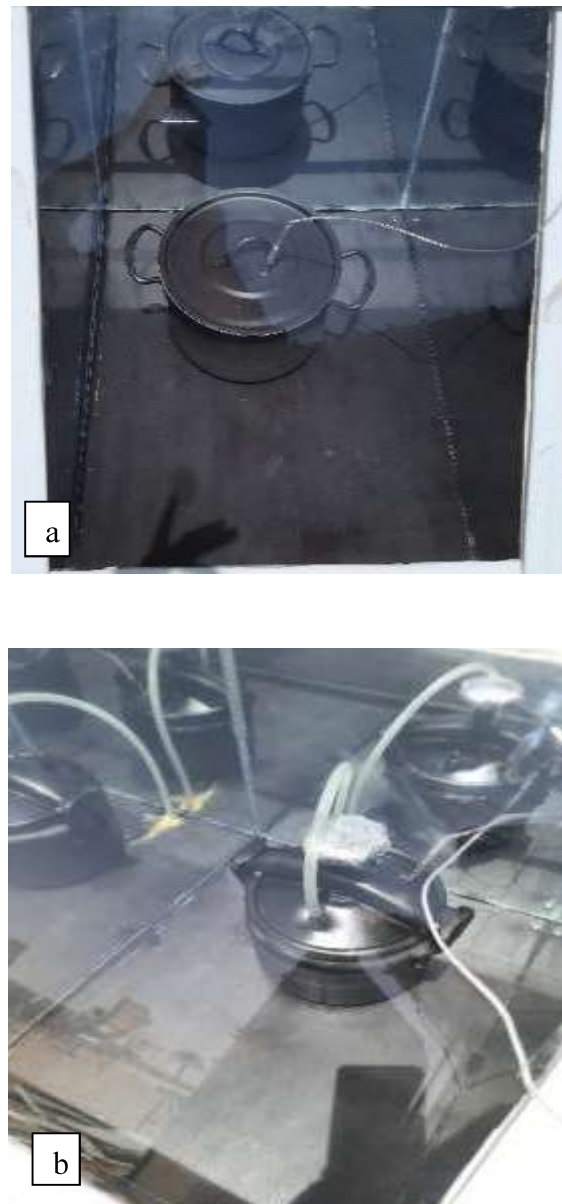


Figure 1. Experimental procedure on a box cooker: (a) a simple cooking pot ;(b) a pressure cooker with a flexible pipe.

Table 1. Specifications of measuring gadgets

Characteristic	Type	Range	Accuracy
----------------	------	-------	----------

Solar Irradiation	Pyranometer CMP6	0 – 1500 W/m ²	±2%
Wind Velocity	Anemometer	0 – 40 m/s	±0.5
Temperature measurement	The Campbell CS215	-40 up to 70	±0.4°C
	Thermocouple type K	-50 – 1250 °C	±2.2°C
Data Acquisition	AGILENT 34972A	-	-

3. Performance Measures

3.1 The figures of Merit

The two parameters assess the performance of the cooker, where F_1 (m² °C/W) represents the optical efficiency to the heat loss. In addition, F_2 is identified under complete load conditions and can be articulated both through the expression provided as follows [12]:

$$F_1 = \frac{\eta_0}{U_L} = \frac{T_{p_s} - T_{a_s}}{I_s} \quad (1)$$

$$F_2 = \frac{Mc_p \cdot F_1}{t \cdot A} \cdot \ln \left[\frac{\left(1 - \left(\frac{1}{F_1} \right) \cdot \left(\frac{T_{w_i} - \bar{T}_a}{\bar{I}_s} \right) \right)}{\left(1 - \left(\frac{1}{F_1} \right) \cdot \left(\frac{T_{w_f} - \bar{T}_a}{\bar{I}_s} \right) \right)} \right] \quad (2)$$

Where T_{p_s} , a_s (°C), are the temperatures of the absorber and ambient, and I_s is the solar irradiation (W/m²). Furthermore, T_{w_i} , T_{w_f} are the temperatures of water (initial, final), t is the time required (min), and A is the aperture area (m²).

4. Results and Discussion

The experiment of the first configuration and the sensible testing concerning the simple cooking pot and the pressure cooker were performed in May 2025.

4.1 First configuration (Stagnation test)

As seen in Figure 2, the stagnation test was performed (no load condition). The graph illustrates solar irradiation and ambient, trapped air temperature, as well as their impact on the stagnation temperature recorded on the absorber of the cooker. The highest temperature recorded for the absorber was 130.4 °C, achieved after a duration of 2 hours and 20 minutes, specifically at 12:20. The associated insolation value at that time was 932 W/m². F_1 estimated 0.11 m² °C/W by using Equation 1, where the ambient, absorber temperature, and solar irradiation at stagnation were 129 °C, 27°C, and 918.5 W/m².

The initial figure of merit ranges from 0.10 to 0.14 [12]. A higher F_1 value signifies better optical efficiency as well as a reduced heat loss. The solar cooker we have developed exhibits a satisfactory value of the parameter F_1 ($0.11 \text{ m}^2\text{°C/W}$) due to the good interception of solar rays, a consequence of the inclined receiving surface design realized. The significant temperature of 80 °C , which is appropriate for cooking an item, was achieved merely 1 hour after the commencement of the trial. This impressive efficiency can be ascribed to the characteristics of every element within the constructed box cooker.

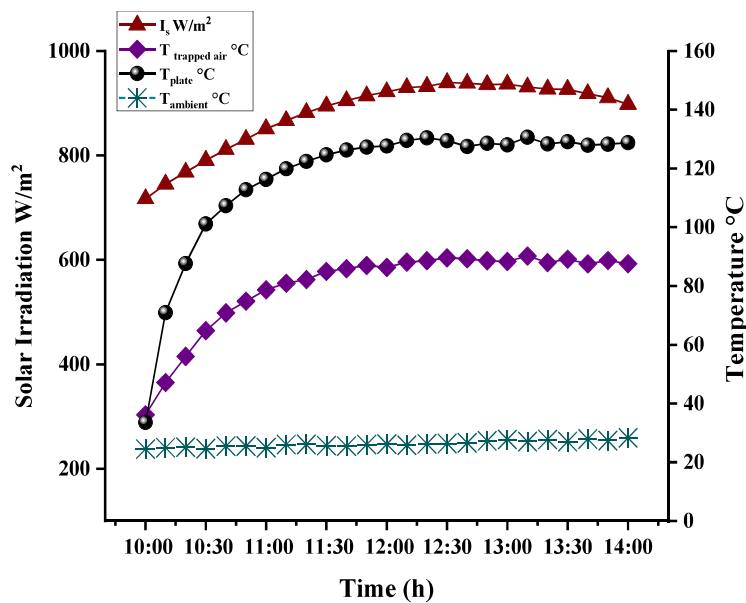


Figure 2. Stagnation testing of the box cooker configuration 1.

4.2 Second configuration (Sensible heat test)

The sensible testing was implemented under the full load conditions, where 1 kg of water is considered the cooking medium.

As depicted in Figure 3, the profile temperature of the absorber, water, ambient, and trapped air temperature in the case used a simple vessel. The maximum absorber temperature reached was 113.3 °C , while T_w , T_a , $T_{\text{trapped air}}$, and I_s have been found to be 96 °C , 30 °C , 84.6 °C , and 938.3 W/m^2 (around 12:40 hrs).

During the experimental evaluation, significant vapor condensation was observed across the entire inner surface of the solar cooker's glass cover, as illustrated in Figure 4. This condensation phenomenon adversely affected the thermal performance by progressively reducing the absorber plate temperature from an initial peak of 113.3 °C to a lower value of 103.8 °C . Subsequently, a second

figure of merit, denoted as F_2 , was computed using the established formula (2) and found to be 0.427, where the aperture area is 0.24 m^2 . This value indicates an improved thermal performance and confirms that the cooker meets the minimum performance standards outlined in the Bureau of Indian Standards (BIS) criteria based on the figures of merit. Furthermore, the duration required to reach a water boiling (98.3°C) was recorded at approximately 180 minutes, corresponding to around 13:00 hrs, under a solar irradiance level of 936.6 W/m^2 .

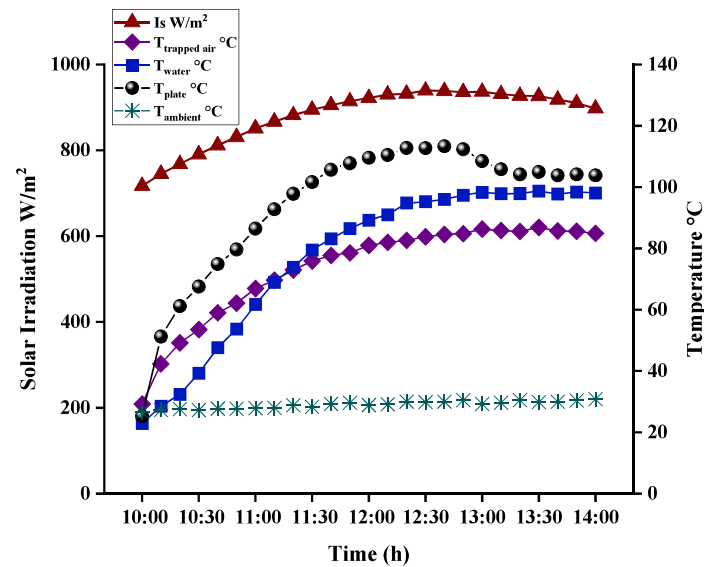


Figure 3. Sensible testing of the box cooker with a simple cooking pot.



Figure 4. A photo illustrates vapor condensation on the glass cover of a box cooker. As illustrated in Figure 5, the temperature variation was analyzed for the configuration in which a pressure cooker was used in conjunction with a flexible pipe to redirect steam. The highest

temperature achieved by the absorber reached $112.5\text{ }^{\circ}\text{C}$, while the corresponding water temperature (T_w) and the trapped air temperature ($T_{\text{trapped air}}$) were measured as $95.2\text{ }^{\circ}\text{C}$ and $73\text{ }^{\circ}\text{C}$, respectively, around 13:10 hours, under a solar irradiation of 930.367 W/m^2 . Notably, the duration needed for the water temperature to attain $95.25\text{ }^{\circ}\text{C}$ was approximately 160 minutes, corresponding to around 12:40 hours under a surrounding temperature of $30.01\text{ }^{\circ}\text{C}$. A key observation in this experiment was the successful elimination of steam condensation on the internal surface of the glass, which contributed to maintaining the absorber's thermal performance without any noticeable temperature decline, thus enhancing the overall efficiency of the cooking process.

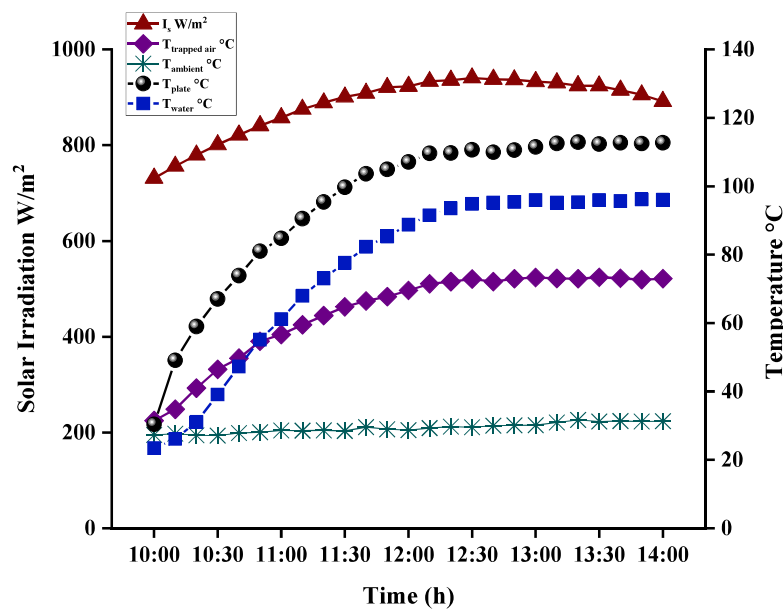


Figure 5. Sensible testing of the pressure cooker with a flexible pipe of the box cooker.

5. Conclusion

According to the findings of an experimental investigation implemented on a solar box cooker, the system underwent evaluation under two different configurations to assess its thermal performance. In the first configuration, the cooker was tested using a conventional simple pot, while in the second configuration, a pressure cooker was employed, equipped with a flexible pipe designed to direct and release hot vapor outside the cooking chamber. This design aimed to mitigate the effects of steam condensation on the inner surface of the glass cover. In the simple pot configuration, the peak temperature recorded by the absorber reached $130.4\text{ }^{\circ}\text{C}$, as well as the figures of merit were identified to be $0.11\text{ m}^2\text{ }^{\circ}\text{C/W}$ & 0.427 . Notably, the occurrence of vapor condensation on the glass significantly

impacted the performance by reducing the efficiency of heat transfer to the absorber, which in turn influenced both the effectiveness of cooking and the thermal storage capacity. However, the integration of the pressure cooker with a flexible pipe successfully prevented condensation, maintained higher absorber temperatures, and demonstrated a promising enhancement in the overall efficiency of a box cooker, rendering it a viable solution for enhanced solar cooking applications.

6. References

- [1] Mekonnen Bassazin A, Liyew Kassa Wudineh & Tigabu M T. Solar cooking in Ethiopia: Experimental testing and performance evaluation of SK14 solar cooker. *Case Studies in Thermal Engineering* 2020: (22), (100766).
- [2] Ky, Thierry Sikoudouin M, Brice A Zoungrana, Drissa Boro, Boureima Dianda, Salifou O, Adama O, Sié K, & Dieudonné J Bathiébo. Conception, realization and testing of a solar cooker built with a spherical reflector in Burkina Faso. *Solar Energy* 2024 ; (272), (112497).
- [3] Hosseinzadeh Mohammad, Reza Sadeghirad, Hosein Zamani, Ali Kianifar, and Seyyed Mahdi Mirzababae. The performance improvement of an indirect solar cooker using multi-walled carbon nanotube-oil nanofluid: An experimental study with thermodynamic analysis. *Renewable Energy* 2021: 165, 14-24.
- [4] Saxena Abhishek, & N Agarwal. " Performance characteristics of a new hybrid solar cooker with air duct ". *Solar Energy* 2018, (159), (628-637).
- [5] Reciou, L., Yettou, F., Gama, A., & Benbaha, A. (2025). *Experimental Study of Solar Box Cooker Preheated by an Electric Energy Source*. (pp. 133-137). Cham: Springer Nature Switzerland.
- [6] Yettou Fatiha, Azoui Boubakeur, Malek Ali, Gama Amor , and Panwar Narayan Lal. Solar cooker realizations in actual use: An overview. *Renewable and Sustainable Energy Reviews* 2014; 37, (288 -306).
- [7] M.A Tawfik, Sagade Atul A, Palma-Behnke Rodrigo, El-Shal Hanan M and W E Abd Allah. Solar cooker with tracking-type bottom reflector: An experimental thermal performance evaluation of a new design. *Solar Energy* 2021; 220, (295-315).
- [8] Goyal, Ravi K. and Eswaramoorthy Muthusamy. " Thermal performance enhancement on a box-type solar cooker using a triangular fin over a conventional cooking pot ". *Solar Energy* (2023); 258, (339-350).
- [9] Verma V, Shringi K, Sharma S, Sengar N, & Giri, N. C. Experimental thermal performance studies on solar hot box cooker with different absorber coating materials. *Materials Today* 2023; 92, (1369-1373).
- [10] Ademe Zeleke & Sameer Hameer. Design, construction and performance evaluation of a Box type solar cooker with a glazing wiper mechanism. *AIMS energy* 2018, 6(1).
- [11] Goyal Ravi Kumar, & Eswaramoorthy M. Theoretical and experimental analysis of box-type solar cooker with sensible heat storage. *Solar Energy* (2024), (268).
- [12] Mullick S. C, Kandpal T. C, & Saxena A. K. Thermal test procedure for box-type solar cookers. *Solar energy* 1987, 39(4), 353-360.



Relationship between geometric shapes of hollow bricks and their thermal efficiency: Case of a single-family house in hot desert climates

Nacira BENAROUBA¹, Sifia BELGHERRAS¹, Sidi Mohammed El Amine BEKKOUCHE², Mohamed Kamal CHERIER², Maamar HAMDANI²,

¹ Materials, Energy Systems Technology and Environment Laboratory MESTE, Faculty of Science and Technology, University of Ghardaïa, BP 455 Airport Road, Noumerate, Ghardaïa, Algeria

² Unité de Recherche Appliquée en Énergie s Renouvelables, URAER, Centre de Développement des Energies Renouvelables, CDER, 47133, Ghardaïa, Algeria

*Corresponding author: (Nacira BENAROUBA), *Email Address:* nacirabenarouba@gmail.com

Abstract

Air cavities play a crucial role in energy efficiency. Well-designed air cavities serve as an insulating barrier and minimize thermal bridges. The investigation aims to explore several aspects, including the impact of the number of cavities and their geometric shapes on thermal resistance. The calculation guidelines have been established by the standards outlined in the Algerian Regulatory Technical Document DTR.C3-4. The number of test cases for a hollow brick in a vertical position will consist of 12 configurations, all with the same external dimensions of 20 cm × 15 cm × 30 cm. The goal is to prioritize the design of air cavities within the hollow bricks to improve their thermal efficiency. The internal structure and the number of cavities significantly impact thermal resistance. Cavity columns are typically better suited for hollow bricks, as they enhance load distribution and offer superior thermal and compressive resistance, crucial for masonry structures. The multiple cross walls in hollow bricks might create thermal bridges, which can enhance heat transfer between the sides of the brick.

Keywords: Air cavities; Geometric shapes; Hollow bricks; Electrical analogies; Thermal resistance; Energy needs.

<https://doi.org/10.63070/jesc.2025.040>

Received 10 July 2025; Revised 11 November 2025; Accepted 12 December 2025;

Available online 24 December 2025.

Published by Islamic University of Madinah on behalf of *Islamic University Journal of Applied Sciences*.

This is a free open access article under the Creative Attribution (CC.BY.4.0) license.

1. Introduction

Energy requirements for cooling and heating are responsible for nearly 40% of the total electric energy consumption in Algeria [1-2]. This situation is typical in regions of harsh climatic conditions with extremely hot and cold climates [3]. Building envelopes made of hollow bricks with air cavities are an innovative approach. These materials are designed to enhance thermal insulation, reduce energy consumption, and improve overall building performance. Hollow bricks, often made from clay or concrete, feature internal voids that create air cavities, which serve as thermal barriers. This design helps to minimize heat transfer between the interior and exterior of a building, contributing to energy efficiency [4-6]. Bekkouche et al. [1] highlighted that, in arid regions, hollow bricks offer an optimal balance of thermal comfort compared to heavy stone and cinderblock. Similarly, Bellahcene et al. [7] emphasized that the thermal performance of hollow bricks largely depends on the number and geometric configuration of their cavities, which significantly influence the insulation and thermal resistance of walls. Consequently, hollow bricks exhibit favorable thermal and physical properties, effectively minimizing heat transfer through the building envelope and reducing energy consumption across all seasons.

According to previous studies [8], it can be inferred that several factors must be taken into account when designing façade walls. These include the thickness of the bricks, the configuration of the air cavities, and their overall arrangement, all of which are crucial for optimizing thermal insulation performance. Cavity columns are typically better suited for hollow bricks due to their advantages in load distribution. They enhance thermal performance and compressive strength, both of which are crucial for the integrity of masonry structures. Additionally, their design contributes to more efficient weight distribution and improved resistance to thermal fluctuations, making them an ideal choice for such applications. Cavity lines may also be utilized, but they are frequently less efficient regarding resistance and stability. The large number of cross walls in hollow bricks can lead to thermal bridging, making it easier for heat to transfer from one side of the brick to the other. It is precisely at this point that the idea of this work is situated. We want to change several configurations of air cavity bricks to observe the influence of thermal bridges on the thermal characteristics of this building material. For this, 12 geometric shapes for hollow bricks, based on steady-state heat transfer, have been suggested. The purpose of the investigation was focused on the effect of the cavities number and their geometric shape on their thermal resistances.

The distinctive nature of this study is also linked to an Algerian computational technique that produces innovative results, enriching the understanding of building physics. The calculation guidelines have been developed to meet the standards mandated by the Algerian thermal regulation (Regulatory Technical Document DTR.C3-4). The second goal is to optimize the cavity configuration, which reduces heat loss through the walls and consequently improves energy management in the building. However, by intelligently optimizing the geometry of internal cavities, effective insulation of cavity walls can capture warm or cold air and inhibit the circulation of undesired air through the cavity. This approach significantly enhances building performance and interior comfort. The energy needs calculation method assesses the energy required for heating and cooling. The resulting data will be utilized to evaluate the energy efficiency of these cavity walls in comparison to a standard single wall.

2. Materials and Methods

A refined methodology, rooted in established classical formulas and aligned with standards endorsed by the scientific community and official technical documentation, was employed to fulfill the outlined objectives. Hollow bricks were purposefully selected as the subject of the investigation to assess the influence of internal voids on thermal performance. These bricks are crafted from terracotta, a natural composite of clay and sand undergoing a meticulous process of grinding, moistening, molding, and drying, followed by firing at high temperatures ranging between 900°C and 1200°C for approximately thirty hours.

A. Thermal and electrical analogies

The electrical-thermal analogy has been established as a practical approach for determining equivalent thermal resistances. The thermal resistance R ($\text{m}^2\cdot\text{K}/\text{W}$) is influenced by both the geometric configuration and the thermal properties of the materials making up the hollow brick. In this context, the material layers are assumed to be uniform, stacked vertically, and aligned perpendicularly to the direction of heat transfer. The terms $1/h$ ($\text{m}^2\cdot\text{K}/\text{W}$) and e/λ ($\text{m}^2\cdot\text{K}/\text{W}$) represent the thermal resistances of an air layer and a flat wall, respectively where e is thickness, λ is thermal conductivity, and S is surface area. The convective heat transfer coefficient, h , quantifies the exchange between the air cavity and the adjacent vertical surface. The procedure used to estimate the air cavity's equivalent resistance follows the guidelines outlined in the Regulatory Technical Document [9]. This approach is approximate, assuming one-dimensional heat flow and incorporating empirical formulas to account for natural convection and radiative heat exchange within and between cavity surfaces. Thermal

resistance values for air layers can be referenced from the chart presented in Table 1. The thermal conductivity of the terracotta that constitutes the hollow brick is 1.15 W/m.K.

Table 1. Thermal Resistance of the Air Layer as a Function of its Thickness.

Air gap thickness (mm)	5 to 7	8 to 9	10 to 11	12 to 13	14 to 300
Thermal resistance value $m^2.K/W$	0.11	0.13	0.14	0.15	0.16

Figure 1 below depicts the electrical diagram of the hollow brick.

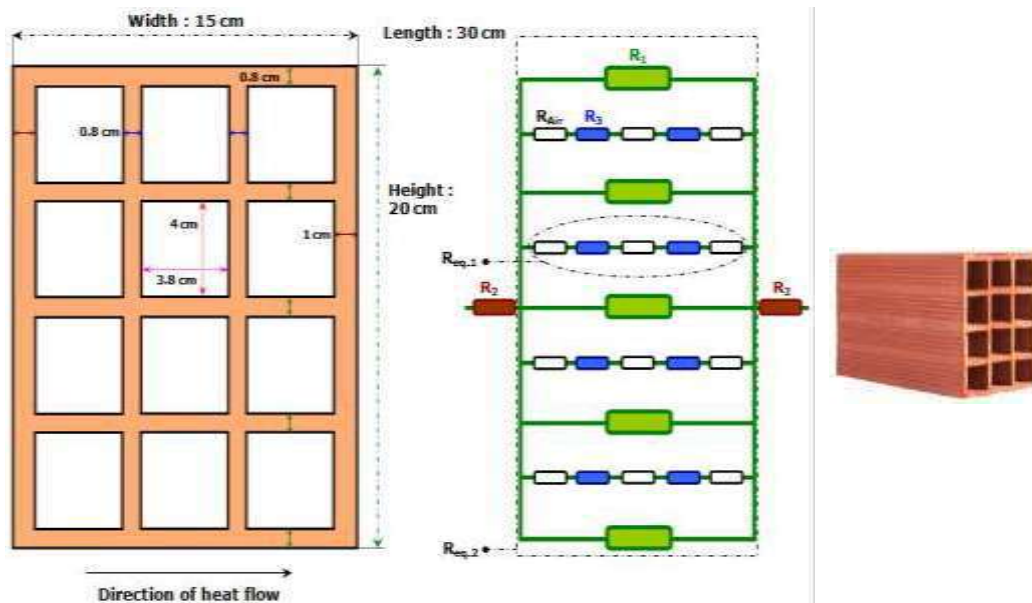


Figure 1. Configuration of the masonry unit and resistor network, case of a hollow brick with 12 identical vertical rectangular cavities of dimensions 4 cm x 3.8 cm

B. Geometric configurations of the studied hollow bricks

The number of test cases for a hollow brick in a vertical position will be 12 configurations. As illustrated in Figure 2, were analyzed, all sharing identical external dimensions of 20 cm × 15 cm. The

objective of this analysis is to offer a systematic basis for prioritizing the design of air cavities in hollow bricks, thereby enhancing their thermal performance. The assumptions made are:

- Heat transfer across the walls is considered unidirectional, moving perpendicular to the brick's vertical facades.
- Heat transfer occurs by conduction in the solid body and by convection in the air cavities.
- The temperature distribution on the external and internal surfaces of the bricks is assumed to be uniform, in accordance with the principle of the nodal method.
- It is also assumed that the thermo-physical properties of the bricks remain constant throughout the process.

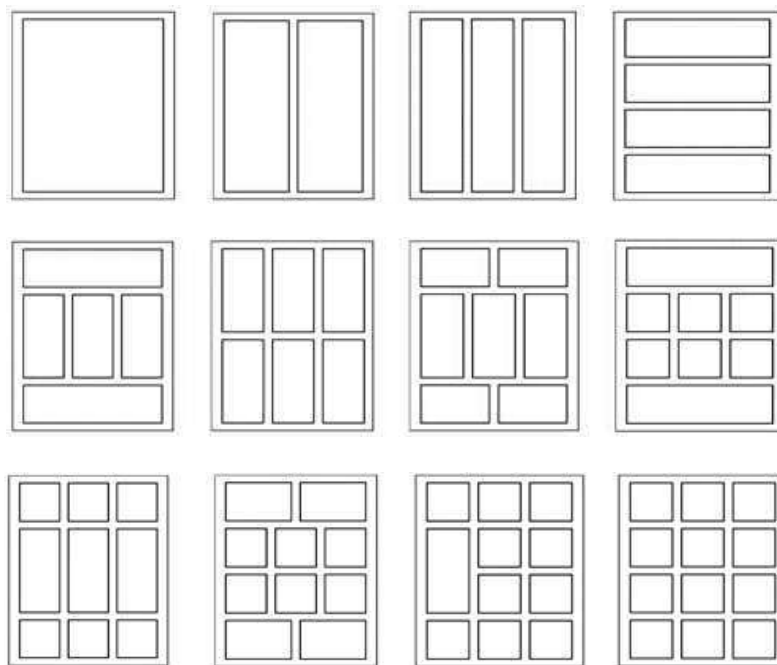


Figure 2. Pre-suggested configurations

C. Summary calculation method for heating and cooling requirements

The energy efficiency of a building is defined by its thermal balance, which involves managing heat gains and losses to maintain comfortable indoor conditions. The calculation of the building's energy needs (Wh) for heating and cooling is mainly based on the following basic equations. The building's energy needs for heating and cooling, typically expressed in kilowatt-hours (kWh), are calculated on the basis of the following basic equations [10-12]:

$$E_{\text{Envelope}} = 24 \text{ Heating and cooling degree days} \times \text{HL}_{\text{Envelope}} \pm \text{Internal heat gain} \pm \text{Passive solar gain} \quad (1)$$

$\text{HL}_{\text{Envelope}}$ is the sum of heat losses through walls, windows, doors, ceilings and roofs, thermal bridges, floors and ventilation, in W/K. represents the total heat losses occurring through walls, windows, doors, ceilings, roofs, thermal bridges, floors, and ventilation, calculated in watts per kelvin (W/K).

$$\text{HL}_{\text{Envelope}} = \text{HL}_{\text{Walls}} + \text{HL}_{\text{Ceilings and Roofs}} + \text{HL}_{\text{Windows}} + \text{HL}_{\text{Doors}} + \text{HL}_{\text{Thermal bridges}} + \text{HL}_{\text{Floors}} + \text{HL}_{\text{Ventilation}} \quad (2)$$

Each building component's heat loss can be assessed through the following general expression:

$$\text{HL}_{\text{Building element}} = \sum_{i=1}^n b_{\text{Building element}-i} S_{\text{Building element}-i} U_{\text{Building element}-i} \quad (3)$$

The variable n represents the total number of thermal zones within the building. The variable i denotes the thermal zone number. The variable $S_{\text{Building element}_i}$ indicates the total surface area of the building element (m^2). The thermal transmittance, indicated by $U_{\text{Building element}_i}$, is quantified as the U-value ($\text{W}/\text{m}^2.\text{K}$). Finally, $b_{\text{Building element}_i}$ serves as the coefficient that measures heat loss reduction.

D. Overview of the building masonry and its thermal-physical characteristics.

This house has a total floor area of 126.69 m^2 and includes a living or dining area, kitchen, two bedrooms, a bathroom, and a toilet as depicted in Figure 3. It is not equipped with an air-conditioning system (for cooling or heating) nor with a mechanical ventilation system. The technical specifications, particularly the composition of the masonry and the thermo-physical properties of the building elements, are detailed in Table 2.

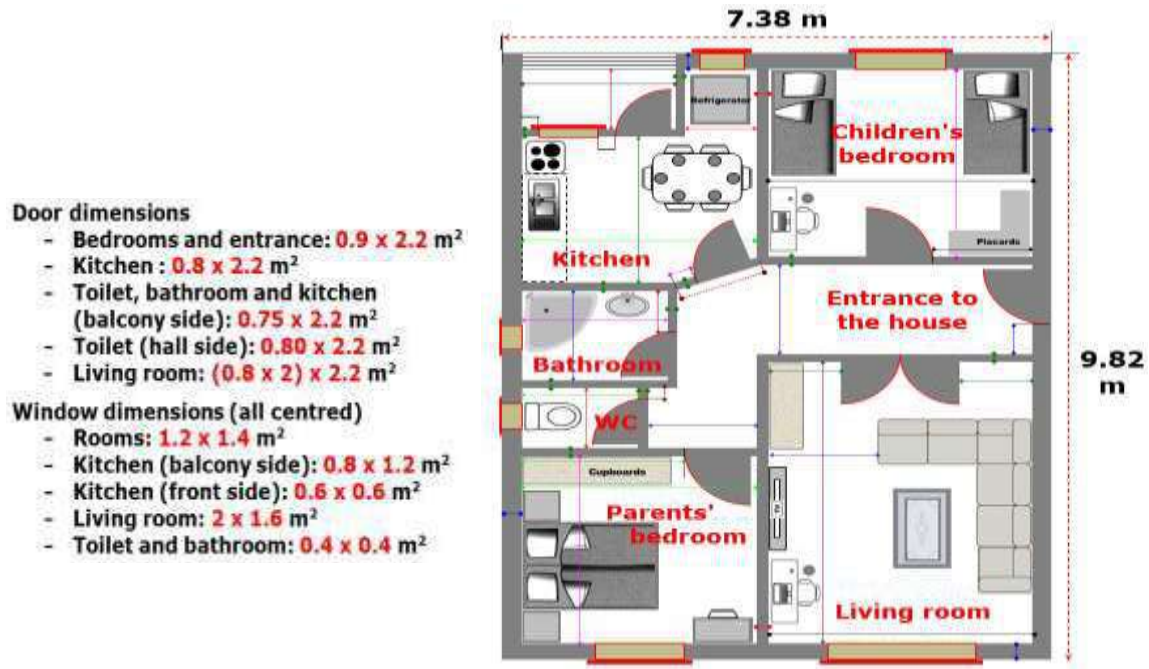


Figure 3. Residential plan illustration

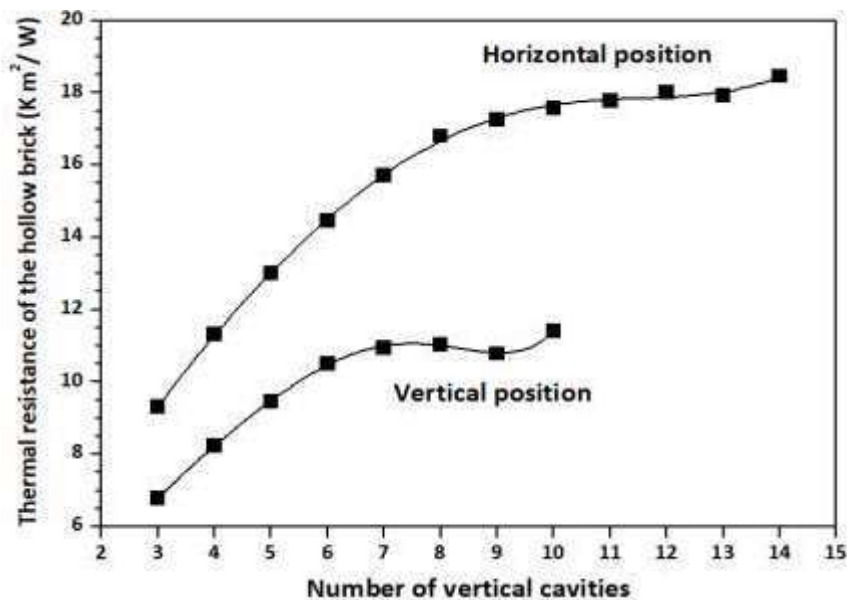
Table 2. Masonry Materials Used in Buildings and Their Thermal Properties

Masonry materials		Thickness mm	Thermal conductivity W/m K	U-value W/m ² .K
Building façades	Exterior rendering	18	1.40	According to the case study
	Bricks designed with cavities	/	/	
	Indoor surface cladding	10	1.40	
	Plaster smoothing layer	02	0.35	
Upper-level roofing	Cement-based mortar screed	50	1.40	2.80
	Hollow core slab 20 x 16 x 53 cm ³	200	1.45	
	Cement mortar rendering	10	1.40	
	Finishing plaster for sleek surfaces	02	0.35	
Floor on solid ground	Granite layer for flooring	20	2.1	1.14
	Cement mortar screed	30	1.4	
	Reinforced concrete slab	200	1.75	
	Ground: Firm foundation	/	/	
Single-glazed windows				5.00
Metal entrance door				5.80

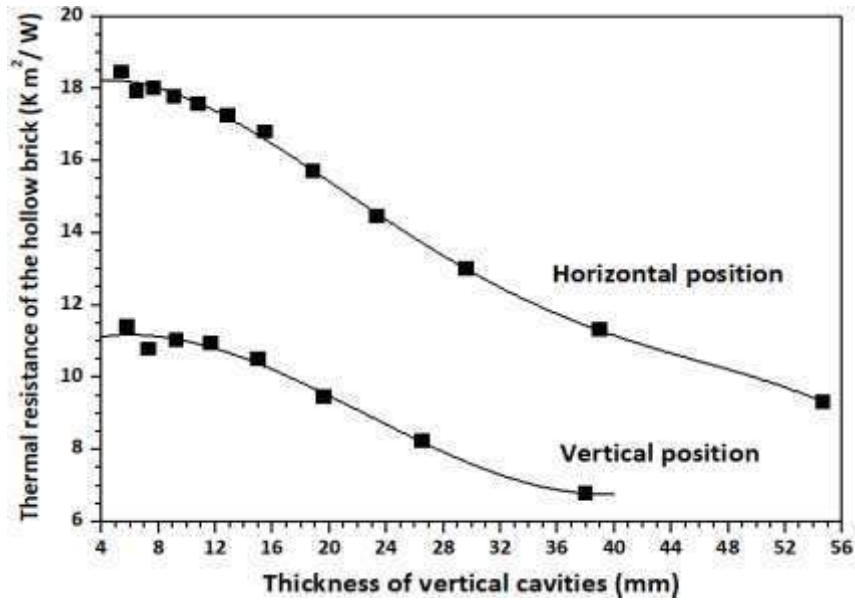
3. Findings and Analysis

In the building construction industry, enhancing thermal resistance in bricks can be achieved through several strategies, including reducing heat transfer and innovating the design of bricks. The findings presented in this section indicate that thermal resistance improves as the number of cavity columns increases, irrespective of the number of cross-sectional walls that are oriented perpendicular to these columns. Additionally, it is important to note that increasing the width of the cavity will consistently lead to a decrease in thermal resistance. Hollow bricks are among the building materials that exhibit good thermal resistance, due to their composition and geometry.

Figure 4 below illustrates a hollow brick that lacks cross-sectional walls; however, as the number of cross-sectional walls increases, the thermal resistance is notably compromised.



(a)



(b)

Figure 4. Variation in thermal resistance in relation to: (a) the number of air cavity columns, (b) the air cavity width, case of a hollow brick without cross-sectional walls [8].

To provide a comparison, Figure 5 illustrates the thermal resistance of a hollow brick that includes three cavity columns. The corresponding thickness of the air cavity is 38 mm if the brick is in the vertical position and 54.67 in the horizontal position.

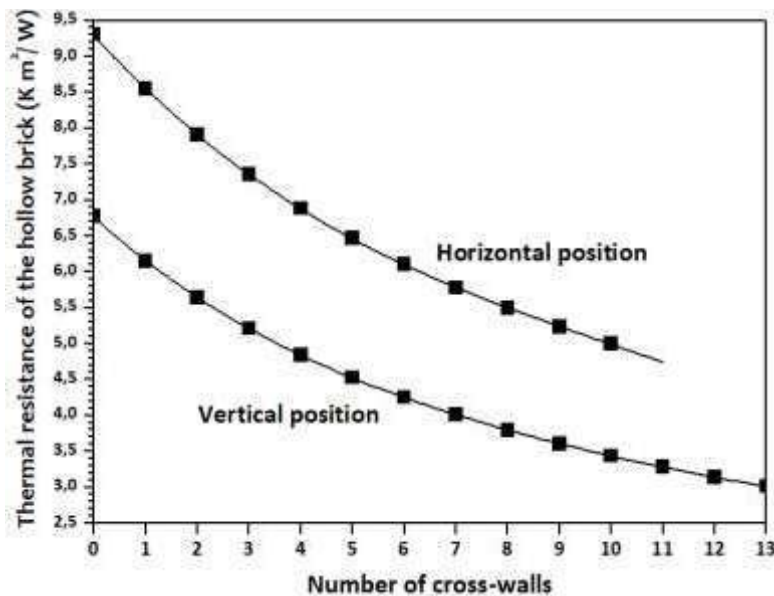


Figure 5. Variation in thermal resistance according to the number of cross-sectional walls, case of a hollow brick with 3 air cavity columns [8].

The bar graphs the effect of the geometric shape of hollow bricks on their thermal resistance. According to the bar graphs (Figure 6), the results obtained in this section show that the number of cavities and their geometric arrangement significantly influence thermal resistance. The key takeaway is that incorporating vertical air cavities, aligned perpendicularly to the direction of heat flow, is more effective in enhancing the bricks thermal resistance.

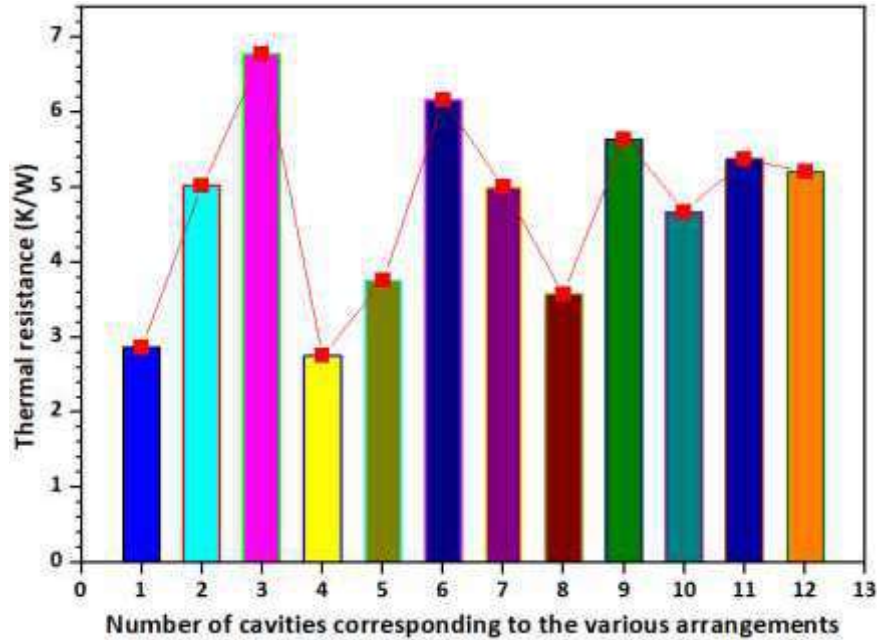


Figure 6. Thermal resistances of hollow bricks according to the various configurations, expressed by the number of air cavities.

As a result, and in line with all previous cases, the findings indicate that the engineering of hollow bricks plays a significant role in enhancing the thermal performance of walls, thereby contributing to a reduction in energy consumption. This is evident in the monthly heating and cooling energy demands, as illustrated in Figure 7.

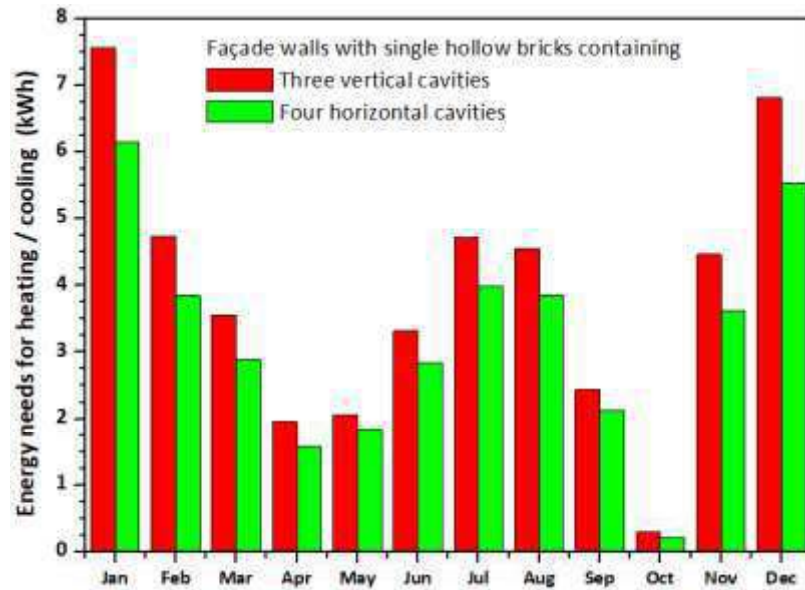


Figure 7. Monthly energy requirements for a temperature between 20 and 28 °C

The results clearly demonstrate that the thermal performance of walls is highly influenced by the geometry of hollow bricks. As illustrated in the bar charts, using 3-cavity hollow brick walls instead of 4-cavity ones led to a notable 17.16% reduction in heating and cooling energy requirements. Hollow bricks enhance both thermal and acoustic insulation, contributing significantly to indoor comfort. This improvement is primarily due to the air trapped within the cavities, which reduces heat conduction and enhances the overall energy efficiency of buildings. To further optimize thermal insulation, alternative geometric configurations can be explored and developed based on the current findings, aiming to increase thermal resistance and reduce the U-value of walls. Such advancements would help ensure better thermal comfort and lower energy consumption, ultimately reducing heating and cooling costs.

4. Conclusion

A well-designed building envelope considers local climatic conditions, thermal performance, and environmental sustainability. In many buildings, overheating is primarily caused by heat absorbed through the walls. The number and shape of cavities in hollow bricks are crucial in improving insulation and thermal resistance.

Cavity design is significant; properly sized and evenly distributed cavities can enhance insulation, whereas oversized or poorly configured cavities may diminish its effectiveness. The internal structure and the number of cavities significantly impact thermal resistance. Cavity columns are typically better

suited for hollow bricks, as they enhance load distribution and offer superior thermal and compressive resistance, crucial for masonry structures. The cavity lines can also be used, they tend to be less effective regarding strength and stability. Additionally, the numerous cross walls in hollow bricks may lead to thermal bridges, facilitating easier heat transfer between the brick's sides.

References

- [1] S.M.A. Bekkouche, T. Benouaz, M.K. Cherier, M.Hamdani, N.Benamrane, and M.R.Yaiche, “Thermal resistances of local building materials and their effect upon the interior temperatures case of a building located in Ghardaïa region” *Construction and Building Materials*, vol. 52, pp. 59-70, Feb. 2014.
- [2] A.M. Omer, “Renewable building energy systems and passive human comfort solutions”, *Renewable and Sustainable Energy Reviews*, vol. 12, no. 6, pp. 1562–1587, Aug. 2008.
- [3] Y. Zhang, G. Ma, G. Wu, S. Liu and L. Gao, “Thermally adaptive walls for buildings applications: A state of the art review”, *Energy and Buildings*, vol. 271, pp. 112314, Sep. 2022.
- [4] M. Dlimi, R. Agounoun, I. Kadiri, R. Saadani and M. Rahmoune, “Thermal performance assessment of double hollow brick walls filled with hemp concrete insulation material through computational fluid dynamics analysis and dynamic thermal simulations”, *e-Prime - Advances in Electrical Engineering, Electronics and Energy*, vol. 3, pp. 100124, Mar. 2023.
- [5] R. Fioretti and P. Principi, “Thermal performance of hollow clay brick with low emissivity treatment in surface enclosures”, vol. 4, pp.715-731, Oct. 2014.
- [6] S. Vera, C. Figueroa, S. Chubretovic, J.C. Remesar and F. Vargas, “Improvement of the thermal performance of hollow clay bricks for structural masonry walls”, *Construction and Building Materials* vol. 415(9), pp. 135060, Feb. 2024.
- [7] L. Bellahcene, M. Teggat, S.M.A. Bekkouche, Z. Younsi and A. Cheknane, “Numerical study of thermal behavior of different cavity section incorporates a phase change material”, *Model. Meas. Control C*, vol. 79(2), pp. 40–45, Jun. 2018.
- [8] N. Benarouba, S. Belgherras, S.M.A. Bekkouche, M. Hamdani and M.K. Cherier, “Main pathways for the emergence of optimized air cavity brick walls”, *Thermal Science.*, in press.
- [9] M.B. Rebzani et al., “Réglementation Thermique du Bâtiment C 3.2 et C 3. 4”, *Document Technique Réglementaire CNERIB*, Ministère de l’habitat., Algérie, Jun-2011.

- [10] S. Belgherras, S.M.A. Bekkouche, T. Benouaz and N. Benamrane, “Prospective analysis of the energy efficiency in a farm studio under Saharan weather conditions”, *Energy Build.*, vol. 145, pp. 342-353, Jun. 2017.
- [11] S. Bendara, S.M.A. Bekkouche, T. Benouaz, S. Belaid, M. Hamdani, M.K. Cherier, A. Boutelhig, N. Benamrane, “Energy efficiency and insulation thickness according to the compactness index case of a studio apartment under saharan weather conditions”, *J. Sol. Energy Eng.*, vol. 141(4), pp. 041011, February 19, 2019.
- [12] Méthode de calcul 3CL-DPE 2021 (Logements existants), https://rt-re-batiment.developpementdurable.gouv.fr/IMG/pdf/consolide_annexe_1_arrete_du_31_03_2021_relatif_aux_methodes_et_procedures_applicables.pdf



Performance Enhancement of Solar Modules in Arid Climates: Dust Mitigation Strategies in Ghardaïa, Algeria

Reski Khelifi^{1*}, Tawfiq Chekifi¹, Abdelkader Si Tayeb¹, Mohamed Lebbi¹, Sofiane Kherrou¹, Lyes Boutina¹, Khaled Touafek¹

¹Unité de Recherche Appliquée en Energies Renouvelables, URAER, Centre de Développement des Energies Renouvelables, CDER, 47133, Algeria, razikoresk@gmail.com

²University of Ghardaia, razikoreski@gmail.com

*Corresponding author: (Reski Khelifi), *Email Address:* razikoresk@gmail.com

Abstract

This study explores how different dust reduction and cleaning methods affect the performance of monocrystalline silicon solar modules in the harsh desert conditions of Ghardaia, Algeria. Six identical solar modules with maximum power point tracking (MPPT) technology were tested to compare three cleaning techniques: water cleaning, cloth cleaning, and a mixture of water and sodium bicarbonate. The water-sodium bicarbonate solution proved highly effective, improving cleaning efficiency by 75% over 10 days. This significant improvement is due to the solution's ability to thoroughly remove dust and dirt that can reduce solar panel performance. The study highlights the importance of choosing the right cleaning methods and scheduling them properly to boost energy output, lower maintenance costs, and ensure reliable solar energy production in dry and dusty environments

Keywords: Solar; Desert conditions; MPPT; Experimental platform

<https://doi.org/10.63070/jesc.2025.041>

Received 10 July 2025; Revised 12 November 2025; Accepted 13 December 2025;

Available online 24 December 2025.

Published by Islamic University of Madinah on behalf of *Islamic University Journal of Applied Sciences*.

This is a free open access article under the Creative Attribution (CC.BY.4.0) license.

1. Introduction

Global warming has become one of the most pressing issues of the 21st century, with rising global temperatures serving as a stark reminder of the ongoing impacts of climate change. Since the Industrial Revolution, average global temperatures have increased by approximately 1.1 degrees Celsius, causing significant disruptions to ecosystems and human livelihoods. In response to these challenges, the transition to renewable energy sources has gained momentum, with solar power playing a pivotal role in reducing greenhouse gas emissions.

Desert regions, characterized by abundant sunlight and vast open spaces, are ideal for the installation of large-scale solar power plants. However, these environments present unique challenges, particularly the accumulation of dust on photovoltaic (PV) modules. Dust deposition can severely impair the performance of solar panels, reducing energy output and increasing maintenance requirements. This issue is especially prevalent in arid regions such as the Middle East and North Africa, where frequent cleaning is essential to maintain efficiency.

To address this problem, various cleaning techniques have been developed, including water-based methods, mechanical brushing, anti-soiling coatings, air-blow cleaning, and advanced solutions such as electrostatic cleaning. The effectiveness of these methods depends on multiple factors, such as dust particle size, weather conditions, module orientation, and local industrial activities.

This study focuses on evaluating the performance of Mono- Si solar modules under harsh desert conditions. It examines the impact of three cleaning methods: water-cleaning, cloth cleaning, and cleaning with a water-sodium bicarbonate mixture, on the efficiency and durability of PV modules. By identifying the most effective cleaning strategies, this research aims to enhance the performance of solar installations in arid climates and contribute to the sustainable development of solar energy systems in challenging environments.

2. Materials and Methods

The experimental platform was established at the Applied Research Unit in Renewable Energies (URAER) in Ghardaïa, southern Algeria (coordinates: 32°34' N, 3°41'55" E), situated 15 km from the city center. This region experiences a dry and hot climate during summer and cold conditions in winter, with temperatures ranging from -5°C to 50°C. The area also receives significant solar radiation, ranging from 800 to 1100 W/m², making it an ideal location for testing solar energy equipment under harsh environmental conditions [6].

The platform features six photovoltaic (PV) modules utilizing monocrystalline silicon (Mono-Si) technology. These modules were installed and evaluated on an experimental photovoltaic system

located at URAER (Figure 1). The modules were mounted on supporting structures with a southward orientation and a tilt angle of 32° , corresponding to the site's latitude. The technical specifications of the PV modules, as provided by the manufacturer, are summarized in Table 1.

TABLE I. Electrical Characteristics of the PV Modules

Parameters	Value
Maximum power (Pmax)	155 W
Optimum operating current (Imp)	8.45 A
Optimum operating voltage (Vmp)	19.54 V
Short circuit current (Isc)	9.03 A
Open circuit voltage (Voc)	23 V
Weight	12 kg
Dimensions	1482*674*45 mm



Figure 1. Experimental test bench (URAER)

These three units were tested under identical conditions at the site, with each panel cleaned separately and manually over a short period, from 05/01/2025 to 19/01/2025. The cleaning methods were allocated as follows: one panel was cleaned with a water-sodium bicarbonate mixture (PV1), the second with a cloth (PV2), and the third with water only (PV3). Additionally, a battery charge controller utilizing the MPPT algorithm was employed to regulate the power output from each PV

module under study. This setup ensured that the maximum power was extracted from each module and efficiently stored in the battery system.

2.1. Performance Analysis of the PV Modules

The performance of each PV panel included in the study was evaluated using technical indicators derived from onsite data collection. These indicators were developed based on the guidelines established by the International Energy Agency (IEA) as part of the Photovoltaic Power Systems Program, originally outlined in the IEC standard 61724 [7,8,9]. This section provides a detailed explanation of the key performance indicators utilized in this study for analyzing the efficiency and effectiveness of the PV panels.

2.2. Energy Output E_{DC}

The total energy produced, E_{DC} , is the sum of the power measured by the module under real outdoor conditions during the measurement sampling period (τ).

$$E_{DC} = \tau \sum_{t=1}^N P_{mes,I} \quad (1)$$

Where τ is the sampling time of the measurements; $P_{mes,I}$ is the maximum power measured at interval of time.

2.3. PV Module Efficiency

The efficiency of a photovoltaic (PV) module is the ratio of the energy produced by the module to the solar incident radiation on its overall surface. This efficiency can be expressed using the following:

$$\eta = \frac{E_{DC}}{G * S} \quad (2)$$

Where E_{DC} is the output energy of the PV module, G is the global solar radiation incident on the surface of the module (W/m^2) and S is the total surface of the module (m^2).

3. Results and Discussion

The study presented in this paper focuses on the presentation and analysis of onsite data collected for three photovoltaic cleaning methods during the observation period. The technology under investigation involved Mono-Si modules. These modules were installed with a southward orientation and a tilt angle of 32° at the designated site.

The analysis was conducted based on specific measurements, including daily average solar radiation, daily average energy efficiency, and performance ratio. Figure 2 illustrates the daily solar radiation at the module level the period from 05/01/2025 to 19/05/2025.

The analysis of the daily solar radiation data reveals an average value of 310.38 W/m^2 during the observation period. The minimum solar radiation recorded was 122.45 W/m^2 on 12/01/2025, while the maximum value reached 361.04 W/m^2 on 11/01/2025, resulting in a radiation range of 238.60 W/m^2 . This significant variability in solar radiation highlights the fluctuating environmental conditions at the site, which can have a considerable impact on the performance of photovoltaic systems. Understanding these variations is crucial for optimizing the efficiency and reliability of solar energy systems under real-world operating conditions.

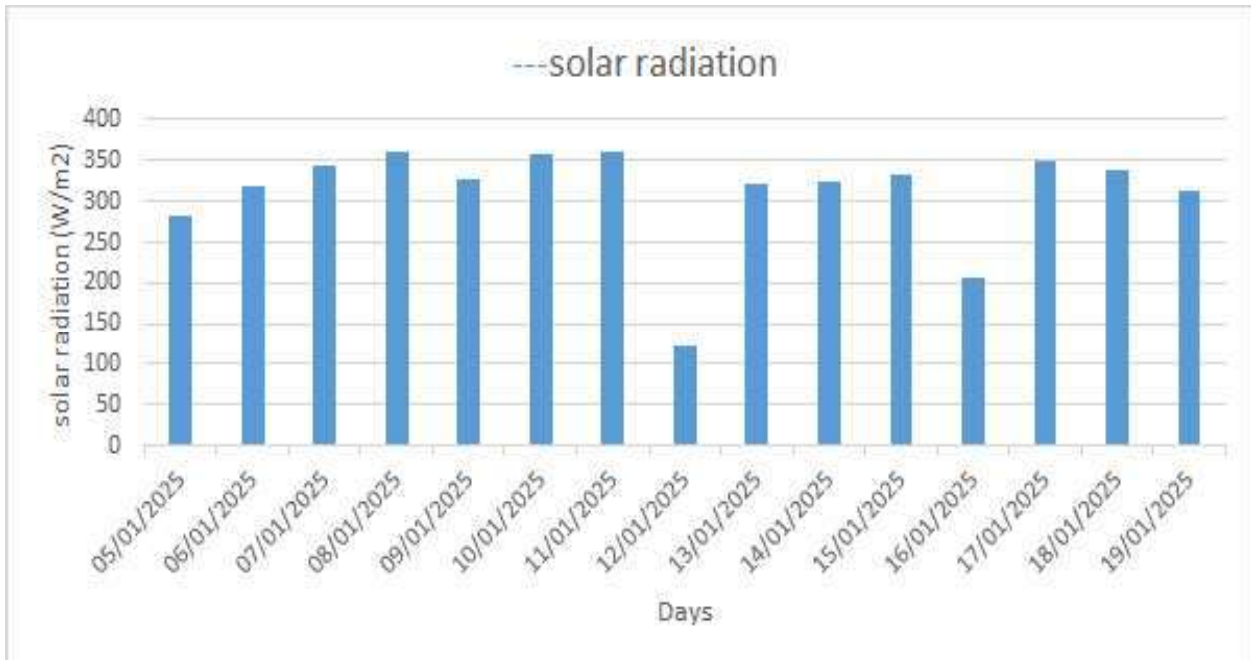


Figure 2. Daily average solar radiation in Ghardaia

Figure 3 illustrates the analysis of the performance data for the three cleaning methods. The water-sodium bicarbonate mixture (P1) proves to be the most effective, with an average performance of 114.40, a maximum of 134.3, and a minimum of 89.63.

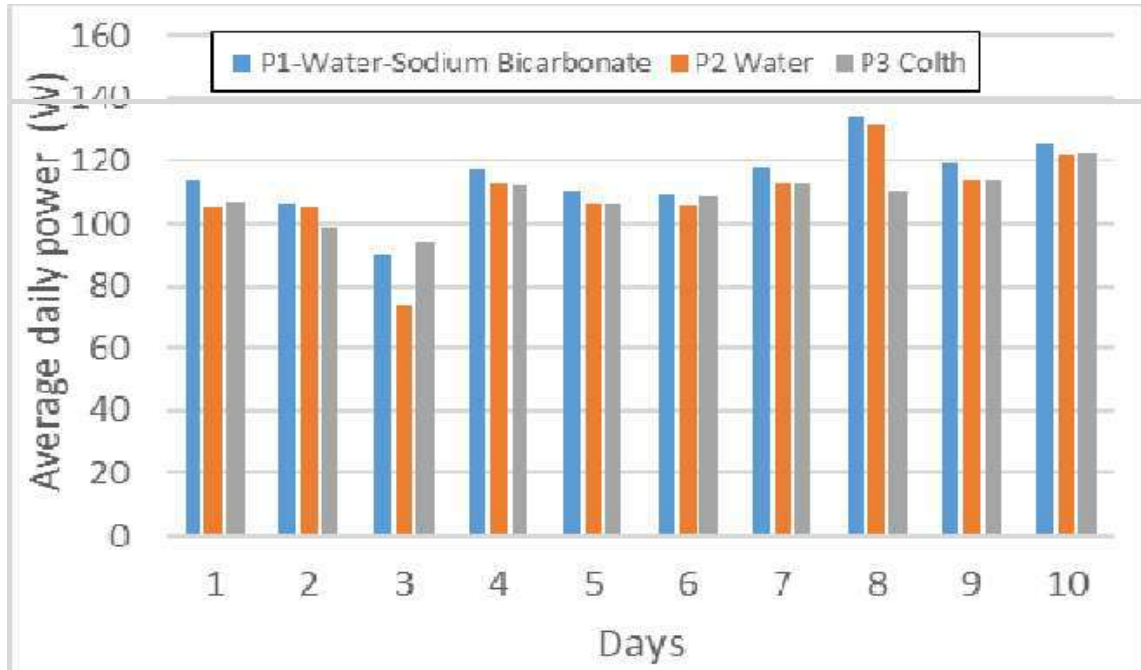


Figure 3. Comparison of daily energy outputs of three Mono-Si photovoltaic panel-cleaning technologies

In comparison, the water cleaning method (P2) demonstrates an average performance of 108.85, with a maximum of 131.4 but a lower minimum of 73.91, indicating greater variability. The cloth cleaning method (P3) achieves an average performance of 108.67, a maximum of 122.7, and a relatively stable minimum of 93.82. These findings indicate that the P1 method not only provides the highest average performance but also achieves the highest maximum values.

Meanwhile, the P3 method is noted for its consistent performance. This analysis confirms that the water-sodium bicarbonate mixture is the most effective solution for enhancing the efficiency of solar panels under the studied conditions.

Figure 4 presents a comparative analysis of the performance of photovoltaic (PV) modules based on three cleaning methods: P1 (Water-Sodium Bicarbonate), P2 (Water Cleaning), and P3 (Cloth Cleaning). The results show that P1 achieved the highest average daily output power of 114.40 W, outperforming P2 and P3, which recorded 108.85 W and 108.67 W, respectively. This highlights the superior effectiveness of the water-sodium bicarbonate mixture in maintaining panel performance under harsh environmental conditions. Similarly, in terms of efficiency,

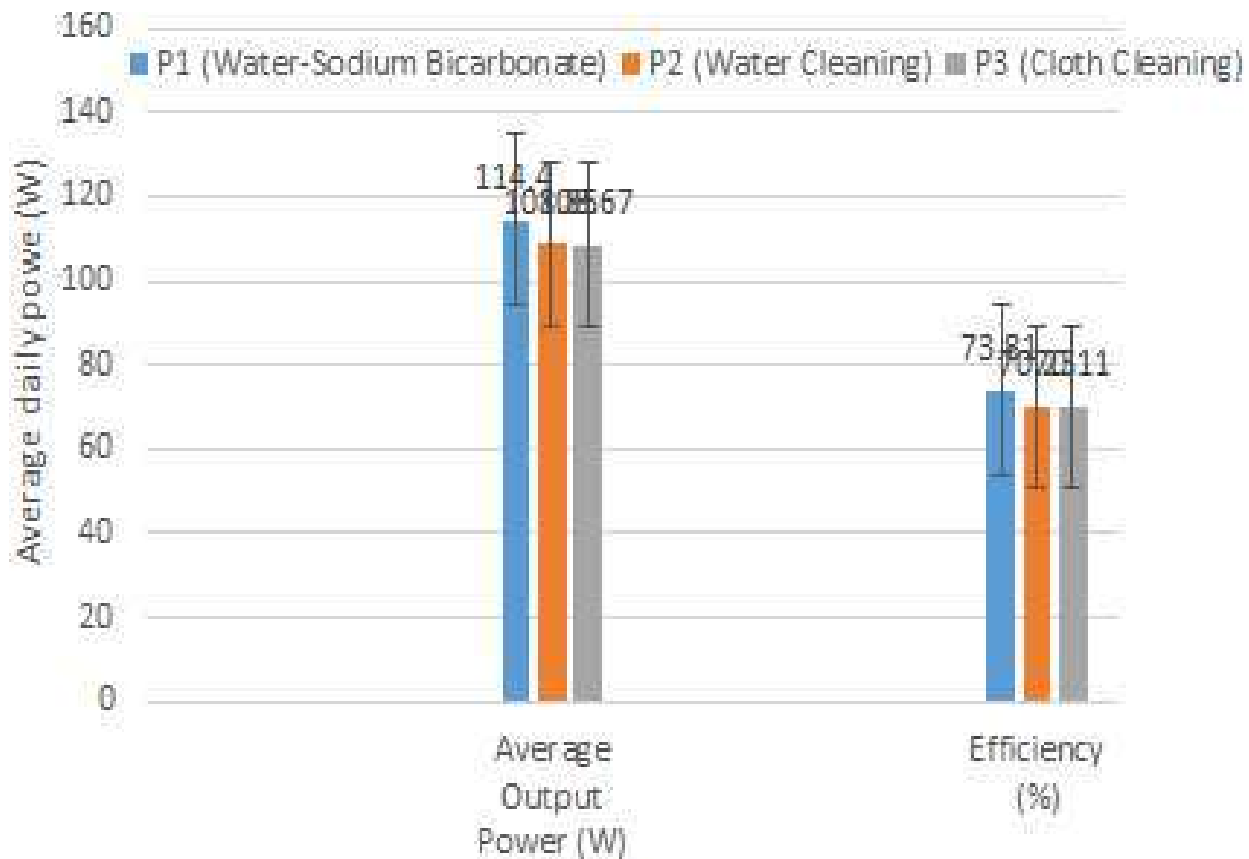


Figure 4. Comparative Analysis of Average Daily Output Power and Efficiency of PV Modules Using Different Cleaning Methods

P1 reached the highest value of 73.81%, while P2 and P3 achieved slightly lower efficiencies of 70.23% and 70.11%, respectively. The error bars indicate variability in performance, with P1 demonstrating less variability compared to P2 and P3, suggesting a more consistent cleaning outcome over the observation period. These findings confirm that the water-sodium bicarbonate mixture is the most effective cleaning method for enhancing PV module performance, particularly in desert-like environments where dust accumulation poses significant challenges.

4. Conclusion

This study underscores the critical role of effective cleaning methods in maintaining and enhancing the performance of photovoltaic (PV) modules, particularly in harsh desert conditions such as those in Ghardaia, Algeria. Among the three cleaning methods examined, the water-sodium bicarbonate mixture (P1) emerged as the most effective, delivering the highest average daily output power (114.40 W) and efficiency (73.81%). This method outperformed water cleaning (P2) and cloth cleaning (P3) in terms of both performance and consistency, as evidenced by the lower variability in results. The findings highlight the importance of using innovative and efficient cleaning techniques to mitigate the adverse effects of dust accumulation, thereby optimizing energy output, reducing maintenance costs, and ensuring reliable operation of solar energy systems in arid and dusty regions. These insights can contribute to the development of sustainable solutions for maximizing the performance and longevity of solar installations in challenging environments.

References

- [1] International Energy Agency (IEA), Photovoltaic Power Systems Program," IEC Standard 61724, 2016.
- [2] M. Mani and R. Pillai, "Impact of dust on solar photovoltaic (PV) performance: Research status, challenges, and recommendations," *Renewable and Sustainable Energy Reviews*, vol. 14, no. 9, pp. 3124–3131, 2010.
- [3] R. Khelifi, M. Guermoui, B. Laouar.: A Novel Hybrid Model for PV Power Forecasting Using Support Vector Machine and Grasshopper Optimization Algorithm: Case Study, 6th International Symposium on New and Renewable Energy (SIENR), Ghadaia, Algeria, pp.1-4 (2021).
- [4] S. Said, M. Hassan, and A. Walwil, "The effect of environmental factors and dust accumulation on photovoltaic modules and dust- accumulation mitigation strategies," *Renewable and Sustainable Energy Reviews*, vol. 82, pp. 743–760, 2018.
- [5] E. Sarver, A. Al-Qaraghuli, and L. Kazmerski, "A review of cleaning methods for solar panel surfaces in desert environments," *Solar Energy Materials & Solar Cells*, vol. 132, pp. 124–135, 2015.
- [6] A. Benatallah et al., "Experimental performance evaluation of monocrystalline PV modules under arid climate conditions," *Applied Solar Energy*, vol. 53, no. 1, pp. 55–61, 2017.
- [7] D. Singh and J. Singh, "Investigation on the performance of photovoltaic systems considering environmental parameters," *International Journal of Energy Research*, vol. 45, no. 7, pp. 937–952, 2021.
- [8] T. Maghami, H. Hizam, C. Gomes, et al., "Impact of dust on solar energy generation based on

actual performance," *Energy Reports*, vol. 2, pp. 129–134, 2016.

[9] J. He, H. Chen, and R. Wennersten, "Effectiveness of sodium bicarbonate solution for cleaning photovoltaic systems," *Journal of Renewable and Sustainable Energy*, vol. 11, no. 5, pp. 054702, 2019.



Hybrid MPPT - Simple boost control of Z source inverter integrated in standalone PV systems

Boukebbous Seif eddine ^{1(*)}, Kerdoun Djallel ¹, Benbaha Nouredine ², Hachemi ammar ²,
Bouchakour Abdelhak ², Kolai meriem ³, Goumidi imen ³

¹ Department of electrotechnics, Laboratory of Electrical Engineering of Constantine (LGEC),
University of Constantine 1 frères mentouri, Algeria

² Unité de Recherche Appliquée en Energie Renouvelable, URAER, Centre de Développement des
Energies Renouvelables, CDER, 47133, Ghardaïa, Algeria

³ Master students at department of electrotechnics, University of Constantine 1 frères mentouri,
Algeria

* Email: boukebbous.seif@gmail.com, boukebbous.seif@umc.edu.dz

Abstract

This study gives a hybrid strategy control of standalone system based on Z source inverter and powered by photovoltaic generators and electrochemical batteries. In off grid application, the most challenge is obtain voltage stability with a higher power quality in all really conditions (meteorological conditions, load variations). The Z-source inverter (ZSI) provides an alternative solution for the conventional voltage source inverter (VSI) by eliminating de DC/DC converter, and replace it by LC network design, this solution reduce the switching power number, losses and cost. In this work, a combined P&O MPPT technique and simple boost control strategy will be integrated in the Z sourec inverter to elaborate the shoot through situations. Many simulation results expose clearly in different situations the reliability and the robustness of the proposed control.

Keywords: Photovoltaic; Maximum power point tracker (MPPT); Z source inverter; Simple boost control; Battery; Standalone system.

<https://doi.org/10.63070/jesc.2025.042>

Received 10 July 2025; Revised 13 November 2025; Accepted 14 December 2025;

Available online 24 December 2025.

Published by Islamic University of Madinah on behalf of *Islamic University Journal of Applied Sciences*.

This is a free open access article under the Creative Attribution (CC.BY.4.0) license.

1. Introduction

With the decrease of conventional energy sources and the growing problem of environmental pollution, the research and utilization of the renewable energy, such as solar energy, wind energy as so on, has been concerned with more and more attention [1], [2]. Photovoltaic power is becoming more prevalent as its cost is becoming more competitive with traditional power sources. However, the utilization of dedicated energy storage systems needs to be taken into account because of the intermittent nature of the PV generation. Energy storage systems can open the possibility to employ renewable energy sources able to operate in standalone mode, grid-connected mode, and mode transitions from stand-alone to grid, or vice versa in micro-grid systems [3], [4].

The power electronics converters have a very important role in integration, control and management of photovoltaic systems. The usually standalone system includes two converters: The first is DC/DC converters which ensure the adaptation of photovoltaic impedance (MPPT). The second is DC/AC converter (inverter) used for create the three phase system. Another structure can be studied using the Z source inverters [5], [6], [7], [8]. By this converter we can reduce the number of switches (losses, and price), also, the input voltage is increased to the necessary value requested.

This paper presents a combined strategy control between MPPT and simple boost control to generate the shoot through and non-shoot through states of the Z source inverter as shown in Figure 1. The batteries are connected directly in parallel with Quasi Z source inverter capacitor C_1 , it makes it possible to regulate the DC bus of the inverter and ensure a free power flow between PV generator and electrical loads. Feasibility and reliability of this control are verified by many rigorous simulation tests in different realistic conditions.

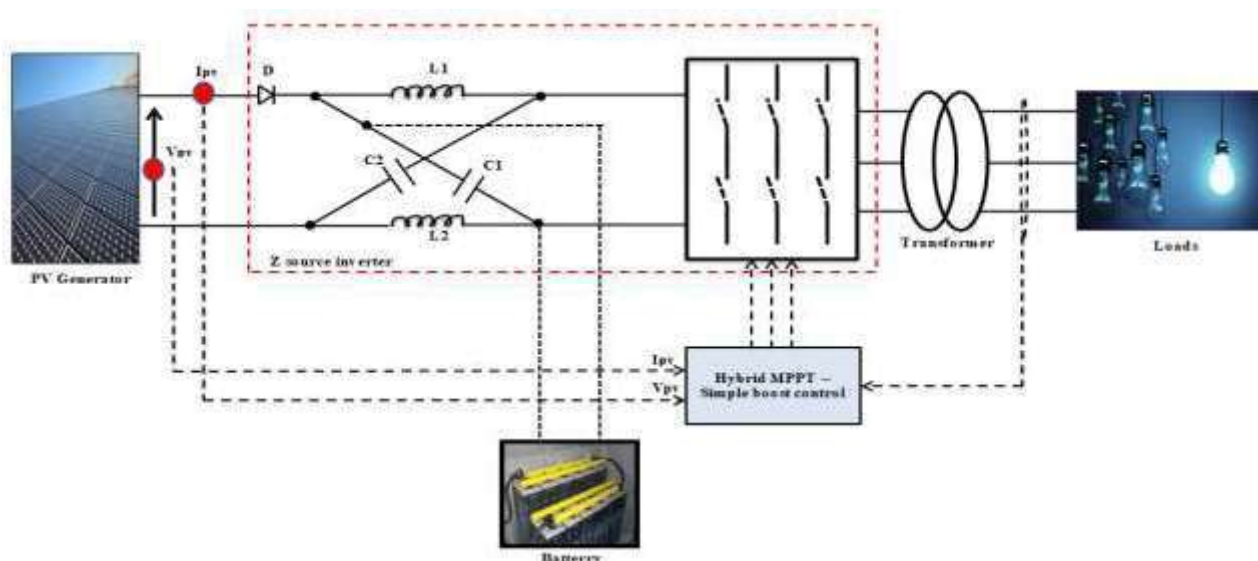


Figure 1. Studied standalone photovoltaic system.

2. Photovoltaic generator model

The photovoltaic cell is modeled like an ideal current source “Fig.2”; its current I_{ph} is proportional to the incident illumination, also, connected with diode which represent P-N junction, R_s and R_{sh} are used for modeling series connecting circuit and parallel current leakage [9], [10], [11].

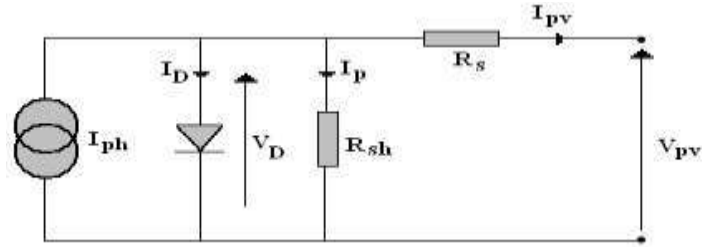


Figure 2. Simple model of the photovoltaic cells.

From this circuit, the PV cell current can be expressed such as:

$$I_{pv} = I_{ph} - I_D - I_p \quad (1)$$

I_D expression being deduced from the semiconductor diode theory, the above relation may be detailed as:

$$I_{pv} = I_{ph} - I_o \left(\exp\left(\frac{V_{pv} + R_s I_{pv}}{nKT/q}\right) - 1 \right) - \frac{V_{pv} + R_s I_{pv}}{R_{sh}} \quad (2)$$

Where, I_{ph} is the light generated current (A), I_o the PV cell saturation current (A), q the electron charge ($q = 1,6 \cdot 10^{-19}$ C), K the Boltzmann constant ($K = 1,38 \cdot 10^{-23}$ J/K), n the cell ideality factor, T the cell temperature. R_{sh} and R_s are pure parasitic resistances characterizing respectively parallel current leakage and series connecting circuit.

In general, for a PVG involving an array of N_s cells connected in series and N_p in parallel, its output voltage current relation may be deduced from the basic cell equation (2) as follows [10], [11]:

$$I_{pv} = N_p I_{ph} - N_p I_o \left(\exp\left(\frac{q(V_{pv} + \frac{N_s}{N_p} R_s I_{pv})}{nKT N_s}\right) - 1 \right) - \frac{V_{pv} + \frac{N_s}{N_p} R_s I_{pv}}{\frac{N_s}{N_p} R_{sh}} \quad (3)$$

3. Z source inverter model

The structure of ZSI used in this study is shown in “Fig.3”.

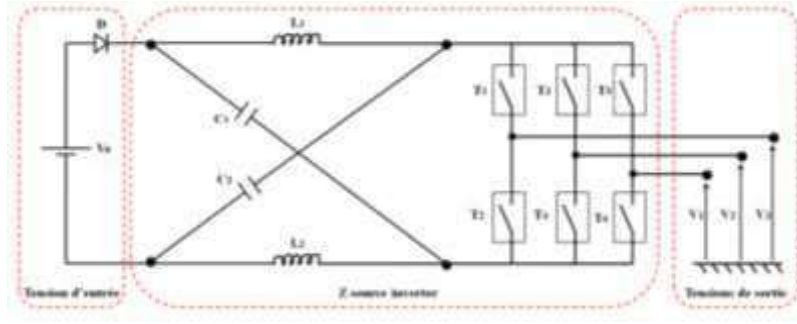


Figure 3. Structure of Z source inverter

From this circuit, we can define two operation modes: shoot through states and non shoot through states. The system equation can be expressed the following equations:

In steady state, the capacitor and inductor voltages are given by:

$$\begin{cases} V_{c1} = V_{c2} = V_c \\ V_{L1} = V_{L2} = V_L \end{cases} \quad (4)$$

The switching period T is divided into two intervals, the first is intended for the shoot states noted T_0 and the second noted T_1 for the traditional active states. Therefore the total switching period becomes:

$$T = T_0 + T_1$$

In shoot states period T_0 :

$$\begin{cases} V_L = V_c \\ V_d = 2V_c \\ V_{dc} = 0 \end{cases}$$

In traditional states period T_1 :

$$\begin{cases} V_L = V_e - V_c \\ V_d = V_e \\ V_{dc} = V_c - V_L = 2V_c - V_e \end{cases}$$

In the total switching period T :

$$V_L = \bar{v}_L = \frac{T_0 V_c + T_1 (V_e - V_c)}{T} = 0$$

So:

$$\frac{V_c}{V_e} = \frac{T_1}{T_1 - T_0}$$

By a similar analysis, the DC voltage can be expressed in steady state such as:

$$V_{dc} = \bar{v}_{dc} = \frac{T_0 \cdot 0 + T_1 (2V_c - V_e)}{T}$$

So:

$$V_{dc} = \frac{T_1}{T_1 - T_0} V_e = V_c$$

The max DC voltage is defined by the following equation:

$$\hat{V}_{dc} = \frac{T}{T_1 - T_0} V_e$$

With:

$$B = \frac{T}{T_1 - T_0} = \frac{1}{1 - 2\frac{T_0}{T}} = \frac{1}{1 - 2D} \geq 1$$

B : amplification factor

D : Shoot- through duty ratio

The max AC output voltage delivered by the Z source inverter is given such as:

$$\hat{V}_{ac} = M.B \frac{V_e}{2}$$

With M is the modulation index expressed by this equation:

$$M = (1 - \frac{T_0}{T})$$

From the previous equations, the capacitor C₁ and C₂ voltages in steady state, can be expressed by the following equation:

$$V_{c1} = V_{c2} = V_c = \frac{1 - \frac{T_0}{T}}{1 - 2\frac{T_0}{T}} V_e = \frac{1 - D}{1 - 2D} V_e$$

$$V_{C1} = \frac{1 - D}{1 - 2D} u_{pv}, \quad V_{C2} = \frac{1 - D}{1 - 2D} u_{pv} \quad (5)$$

The DC-link voltage average value is:

$$V_{dc} = u_{C1} = \frac{1 - D}{1 - 2D} u_{pv} \quad (7)$$

The studied standalone system power flow consists of PV generator power which is controlled by MPPT algorithm and requirement load power, the batteries are used to compensate the nodd power occurred directly in any conditions, so its power is established such as:

$$P_{batt} = P_{pv} - P_{load} \quad (8)$$

4. Principle of control

The Hybrid control diagram of the standalone PV system with batteries energy storage based on Z-source inverter is shown in “Fig.4”.

4.1. MPPT control

When ignoring the voltage drop on the internal resistance, the voltage u_{C1} is approximate to the battery voltage V_{batt} , so from “equation (7)”, we obtain [8], [12]:

$$V_{batt} = u_{C1} = \frac{1-D}{1-2D} u_{pv} \quad (9)$$

$$u_{pv} = \frac{1-2D}{1-D} V_{batt} \quad (10)$$

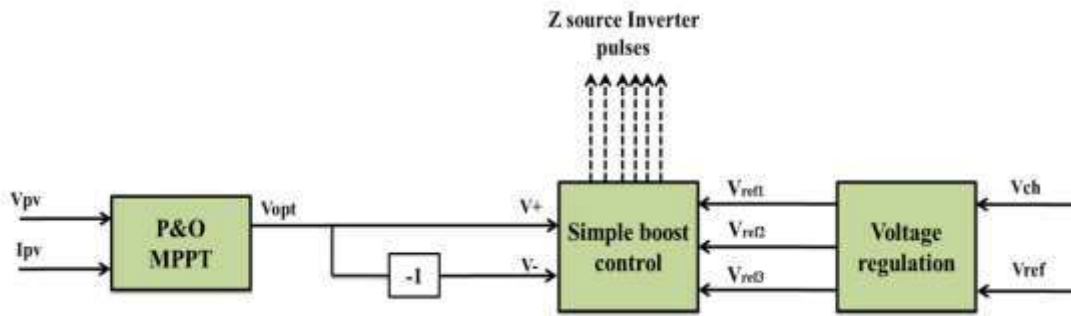


Figure 4. Hybrid control of Z source inverter

From “equation (9)” and “equation (10)” we find:

- By varying the shoot through time in one switching cycle, the input voltage can be boosted.
- The input voltage V_{pv} increases when the shoot-through time is decreased, and decreases when the shoot-through time is increased.

From this equation we can also remark that the maximum power point voltage (V_{opt}) can be tracked by adjusting the shoot-through duty ratio D . For that, the perturbation and observation (P&O) algorithm can be used to determinate the optimal voltage necessary for elaborate the straight positive and negative lines ($V+$, $V-$) commonly used for generate the shoot through states in simple boost control methods.

4.2. Simple boost control

From literature we can find three types of Z source inverter PWM control algorithm: simple boost control (SBC), maximum boost control (MBC), constant boost control (CBC) [13], [14], [15]. In this

study, the first method was adopted, this control strategy inserts shoot through in all the PWM traditional zero states during one switching period. This maintains the six active states unchanged as in the traditional carrier based PWM. Two straight lines are employed to realize the shoot through duty ratio (D_0).

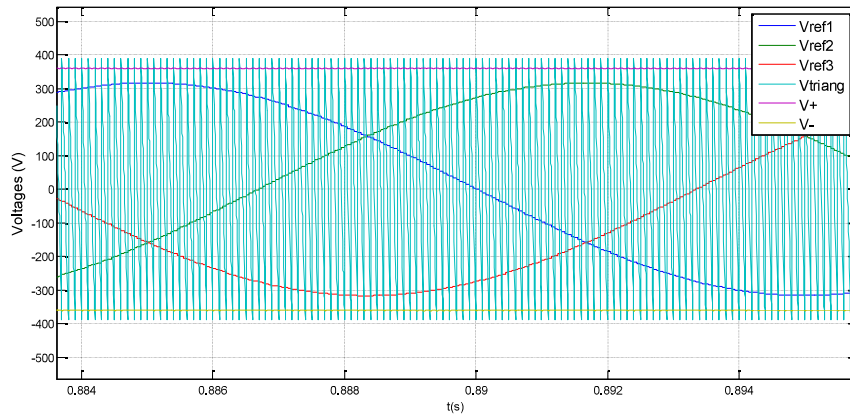


Figure.5. Simple boost control .

The PV voltage reference becomes the shoot-through reference signal (V_+ , V_-). If V_+ is lower than the carrier signal, then all the switches in the three arms will be in the on position. Also if V_- is higher than the carrier signal, then all the switches will be in the on position.

5. Simulation results and discussions

Several numeric simulations are accomplished in MATLAB/SIMULINK for evaluate our system in different conditions (Weather, rapid load variation). The most important results obtained are presented in “Fig.6” to “Fig.12”.

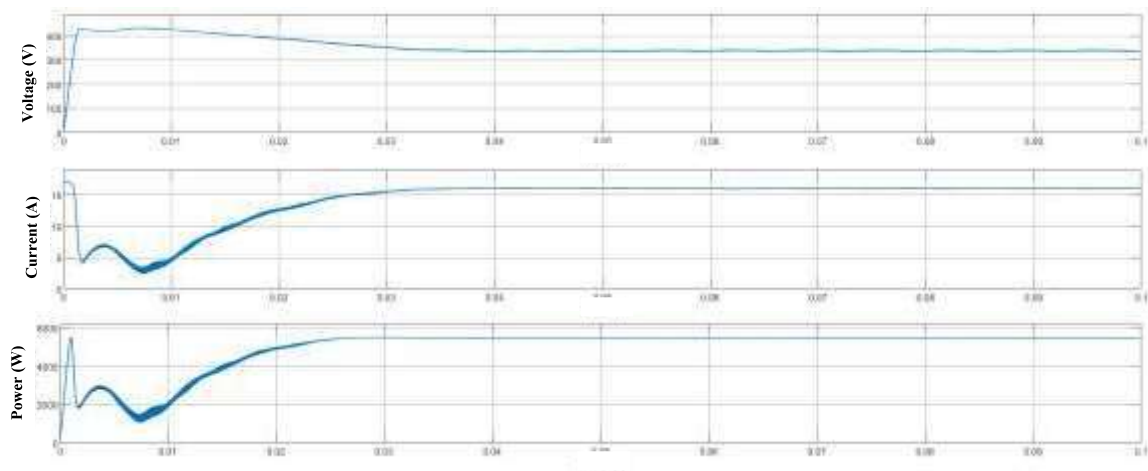


Figure.6. Electrical characteristics of the PV generator

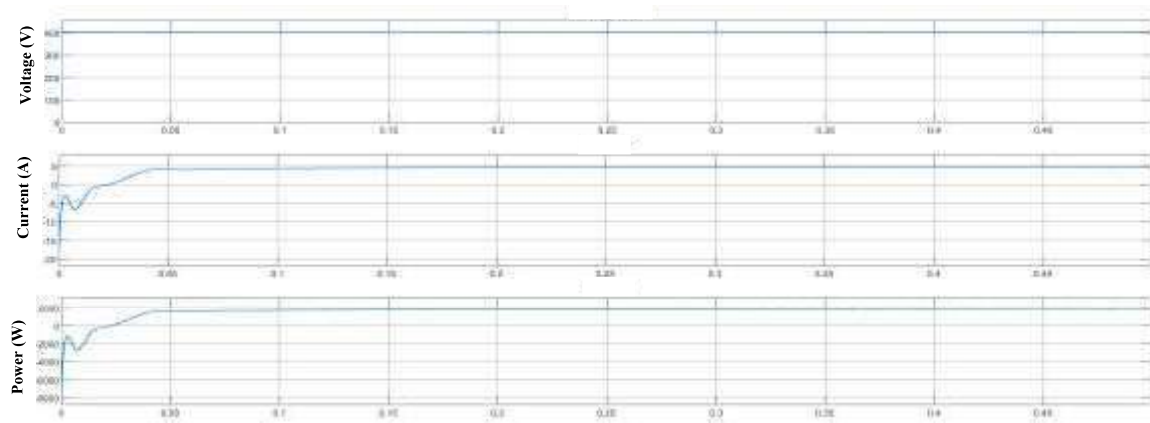


Figure.7. Electrical characteristics of the storage system

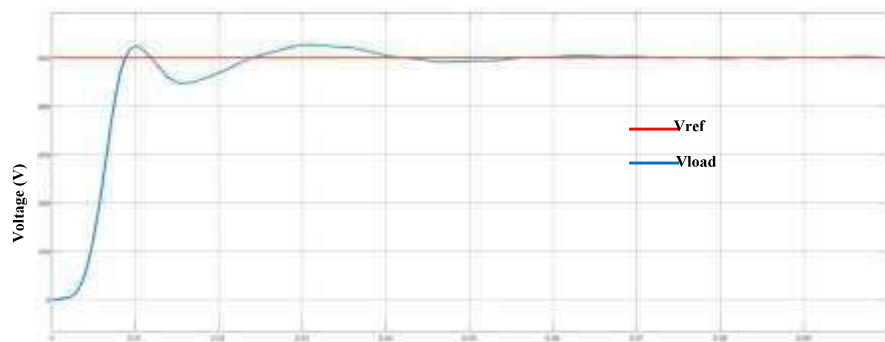


Figure.8. voltage regulation of the standalone PV system

If we have a variable loads fixed by the profile presented in Figure 9, the behavior of the system is expressed by the following results:

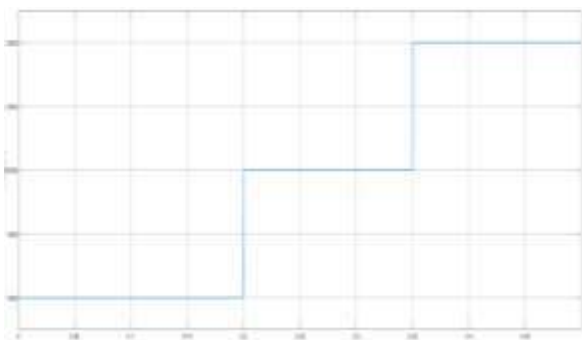


Figure 9. Load profile

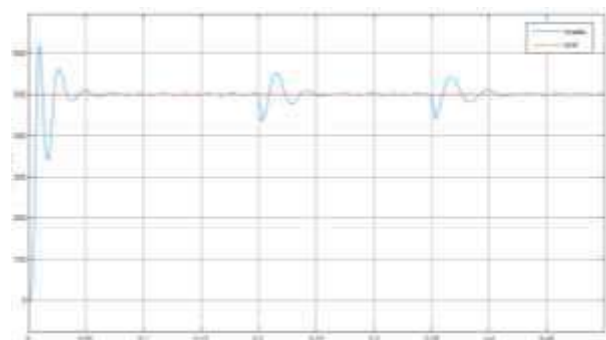


Figure 10. Voltage regulation of the standalone PV system

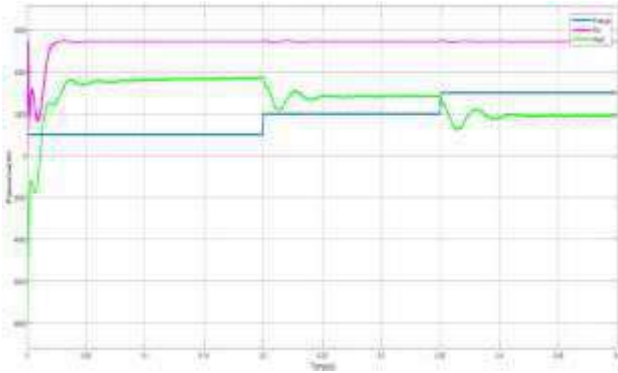


Figure 11. power exchange in the standalone PV system

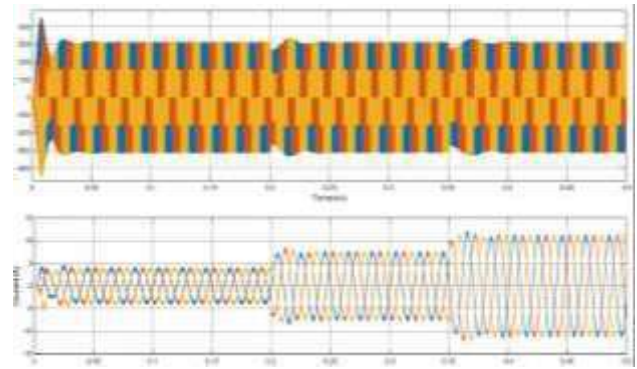


Figure 12. Variation of the load voltages and currents

The electrical characteristics of the PV generator are presented in Figure.6. In standards conditions, the adopted P&O MPPT algorithm follows the maximal point with very acceptable dynamic. In other hand, remarkable power oscillations can be observed in steady state due to the used technics. As presented in Figure.7. The storage system (batteries) absorbs the power surplus produced by PV generator (2kW), so the batteries are in charge mode. From Figure 8, it is clear to observe that, the real load voltage V_{load} follow the fixed values ($V_{ref}=500V$) with very high dynamic.

The voltage regulation exhibits a good performance to fast load variation, like presented in Figure 10, the real load voltage is correctly controlled to follow the reference despite the rigorous situations created at 0.2s and 0.35s. Also, the output simple voltage of the Z source inverter (Figure. 12) confirms the stability and the robustness of the control.

If the load power change from 1 kW to 2kW at 0.2s and from 2kW to 3kW at 0.35s as indicated in Figure 8. The load currents are similar to the classical inverter currents and change with the variation of the power (Figure. 12). In other hand, the P&O algorithm adopted follow exactly the maximum power point of the photovoltaic generator in various illumination conditions, so the totally power produced is transmitted to load and batteries. When the produced photovoltaic energy is higher than that demanded by electrical loads, more energy is stored in the batteries, in the contrary case; the battery intervenes (the batteries transmit energy to loads).

6. Conclusion

The paper presents a hybrid control of standalone PV system based on Z source inverter. The objective is to ensure a robust load voltage regulation and an efficient power management between source (PV), storage (batteries) and load. The MPPT technic and simple boost controls are simultaneously integrated to generate the shoot through states of the Z source inverter. Many simulation results

obtained in several rigorous realistic conditions confirm the validity and reliability of the proposed control system.

References

- [1] W. Cai, H. Ren, Y. Jiao, M. Cai, and X. Cheng, "Analysis and simulation for grid-connected photovoltaic system based on matlab", IEEE International conference electrical and control engineering, pp. 63-66, 2011.
- [2] S. Boukebbous, Dj. Kerdoun, N. Benbaha, H. Ammar, A. Bouchakour, « Quasi Z source inverter output voltage regulation of standalone system powered by photovoltaic generators and batteries », 5th International renewable and sustainable congress IRSEC2017, 04-07 December, Tangier, Morocco, 2017.
- [3] S. Boukebbous, Dj. Kerdoun, "Power control of grid connected photovoltaic system assisted by batteries and water pumping energy storage in desert location", International journal of renewable energy research, in press.
- [4] S. M. Park, and S. Y. Park, "Power weakening control of the photovoltaic-battery system for seamless energy transfer in microgrids", IEEE In Applied Power Electronics Conference and Exposition, pp. 2971-2976, 2013.
- [5] S. Boukebbous, N. Benbaha, A. Bouchakour, H. Ammar, D. Rezzak, "Hybrid PV-battery pumping system based on quasi Z source boost and bidirectional dc-dc converters", International Conference on Advanced Renewable Energy Systems (ICARES'22) Algeria - December 18 -20, 2022.
- [6] C. Rivera, G. Jorge, Y. Li, S. Jiang, and F. Z. Peng, "Quasi-Z-source inverter with energy storage for photovoltaic power generation systems", IEEE In applied power electronics Conference and Exposition, pp. 401-406, 201.
- [7] S. Boukebbous, Dj. Kerdoun, "New strategy control of bidirectional quazi Z source inverter with batteries and supercapacitors energy storage in grid connected photovoltaic system", International journal of power electronics and drive systems, Vol. 8, No.1, pp.335-343, 2017.
- [8] G. Baoming, H. Abu-Rub, F. Z. Peng, Q. Lei, A. T. Almeida, F. J. T. E. Ferreira, D. Sun, and Y. Liu, "An energy-stored quasi-Z-source inverter for application to photovoltaic power system", IEEE transactions on industrial electronics, vol. 60, no. 10, pp. 4468-4481, October 2013.
- [9] M. Khelif, A. M'raoui, and A. Malek, "Simulation, optimization and performance analysis of an analog, easy to implement, perturb and observe MPPT technique to be used in a 1.5 kWp photovoltaic system", IEEE In renewable and sustainable energy conference, pp.10-17, march 2013.
- [10] L. T. Huan, C. T. Siang, and Y. J. Su, "Development of generalized photovoltaic model using matlab/simulink", In proceedings of the world congress on engineering and computer science, Vol.8, pp.1-6, San Francisco 2008.
- [11] M. Francisco, and G. Longatt, "Model of Photovoltaic Module in Matlab™", The 2nd latin american congress of electrical engineering students, electronics and computing, pp.1-5, cibelec, 2005.

- [12]B. Subudhi, and R. Pradhan, “ A Comparative Study on Maximum Power Point Tracking Techniques for Photovoltaic Power Systems”, IEEE transactions on sustainable energy, vol. 4, no. 1, pp. 89-98, january 2013.
- [13]F. Z. Peng, “ Z-source inverter”, IEEE transactions on industry applications, Vol. 39, No. 2, pp-504-410, march-april 2003.
- [14]B. Su, H. Gu, Y. Wang, and W. Zhao, “ Research on the composite control for PV grid-connected and energy-storage based on Quasi-Z-source inverter”, IEEE In Power Electronics and Application Conference and Exposition, pp. 572-577, 2014.
- [15]S. Thangaprakash, “ Unified MPPT Control Strategy for Z-Source Inverter Based Photovoltaic Power Conversion Systems”, Journal of Power Electronics, Vol. 12, No. 1, pp. 172-180, January 2012.



Heat Transfer Enhancement in Solar Air Heaters Using Porous Ribs

Kherrou Sofiane^{1*}, Boutina Lyes¹, Lebbi Mohamed¹, Zarrit Rida¹, Khelifi Reski¹, Dadda Bachir¹

¹ Unité de Recherche Appliquée en Energies Renouvelables URAER, Centre de Développement des Energies Renouvelables, CDER 47133, Ghardaïa, Algeria,

*Corresponding author: (Sofiane Kherrou), Email Address: sofianekherrou@gmail.com

Abstract

Solar air heaters (SAHs) suffer from inherently low thermal efficiency due to poor convective heat transfer between the absorber plate and airflow. This study numerically investigates a novel passive enhancement technique: integrating periodically placed porous ribs on the absorber plate. A comprehensive computational fluid dynamics (CFD) analysis was conducted using ANSYS Fluent to model turbulent flow (Reynolds number range: $3000 \leq Re \leq 12000$) and heat transfer within a rectangular SAH duct. The finite volume method (FVM) solved the governing equations, employing the validated RNG k- ϵ turbulence model and the Darcy-Brinkman-Forchheimer model for the porous rib regions. The primary objectives were to quantify the impact of porous ribs on heat transfer and fluid flow characteristics compared to both smooth ducts and conventional solid ribs, and to optimize key geometric parameters: relative rib height (e/D), relative rib pitch (P/e), and rib porosity. Results demonstrate that porous ribs significantly enhance thermal performance.

Keywords: Porous Ribs; Solar Air Heater; Heat Transfer Enhancement; Thermo-hydraulic Performance.

<https://doi.org/10.63070/jesc.2025.043>

Received 10 July 2025; Revised 14 November 2025; Accepted 15 December 2025;

Available online 24 December 2025.

Published by Islamic University of Madinah on behalf of *Islamic University Journal of Applied Sciences*.

This is a free open access article under the Creative Attribution (CC.BY.4.0) license.

1. Introduction

Solar air heaters (SAHs) represent a vital technology for harnessing renewable energy for applications like space heating, drying, and ventilation. However, their widespread adoption is often limited by inherently low thermal efficiency, primarily stemming from poor heat transfer characteristics between the absorber plate and the flowing air stream [1]. To address this, numerous passive heat transfer enhancement techniques have been investigated over decades.

One of the most prevalent and effective passive methods involves artificially roughening the absorber surface, typically by attaching periodic ribs, baffles, or turbulators. These structures disrupt the laminar sub-layer, promote turbulence, and enhance fluid mixing near the hot surface, significantly improving convective heat transfer [2, 3]. Extensive research, such as the foundational work by Promvonge and Thianpong [4], has demonstrated the effectiveness of solid ribs (e.g., transverse, V-shaped, arc-shaped) in augmenting the Nusselt number (Nu), a key indicator of convective heat transfer performance. However, a critical drawback of solid ribs is the concurrent substantial increase in friction factor (f), leading to higher pumping power requirements [5]. Optimizing rib geometry (pitch (P), height (e), shape) is therefore essential to achieve the best thermo-hydraulic performance (THP), often characterized by parameters like the Performance Evaluation Criterion (PEC) balancing Nu and f enhancements [6, 7]. The computational domain and approach adopted in this work build upon established methodologies like those used by Yadav and Bhagoria [3].

Recently, the integration of porous media within thermal systems, including SAHs and solar dryers, has gained significant attention due to its potential for superior heat transfer augmentation [8, 9]. Porous materials (e.g., metal foams, packed beds, porous blocks) offer a high surface area-to-volume ratio and promote intense local mixing and thermal dispersion within the flow [10]. This characteristic makes them particularly attractive for enhancing energy absorption and transfer efficiency in solar thermal applications [11, 12]. Studies have suggested that porous inserts can lead to significant performance gains, potentially offering a more favorable trade-off between heat transfer enhancement and pressure drop compared to some solid turbulator configurations [13].

Despite the effectiveness of porous media, the specific application of porous ribs as discrete, periodic roughness elements on the SAH absorber plate remains relatively underexplored compared to continuous porous inserts or solid ribs. Porous ribs offer the potential to combine the boundary layer disruption mechanism of traditional ribs with the intense local mixing and extended heat

transfer surface inherent to porous structures, potentially leading to superior thermal performance without a proportional penalty in friction loss.

Motivated by this gap, the present study employs a rigorous numerical approach to investigate the heat transfer and fluid flow characteristics in a rectangular SAH duct equipped with porous ribs on the absorber plate. Where, the primary objectives are:

- To analyze the impact of porous ribs on key performance parameters: average Nusselt number (Nu), convection heat transfer coefficient, and friction factor.
- To systematically investigate the influence of critical geometric parameters, including relative rib height (e/D), relative rib pitch (P/e), and rib porosity.
- To compare the performance of porous ribs directly against conventional solid ribs under identical operating conditions.
- To identify optimal geometric configurations for maximizing the thermo-hydraulic performance of the SAH.

Utilizing the Finite Volume Method (FVM) within ANSYS Fluent, the study solves the governing Navier-Stokes equations coupled with the energy equation. Turbulence is modeled using the RNG $k-\epsilon$ model, validated against literature data for accuracy. Flow within the porous ribs is modeled using the Darcy-Brinkman-Forchheimer (DBF) approach. The computational domain follows established practices for SAH simulation, including entrance, test, and exit sections [3].

This work aims to provide valuable insights and design guidelines for the implementation of porous ribs as a novel and potentially highly efficient heat transfer enhancement technique for next-generation solar air heaters.

2. Methods and modelisation

2.1. System Presentation

The problem to be considered in this study is presented schematically in Figure 1. It involves the 2-D heat transfer and fluid flow characteristics of turbulent flow in rectangular duct of solar air heater with solid ribs and porous ribs, respectively.

The computational domain of an artificially roughened solar air heater is represented in 2D form by a rectangle. The computational domain used in this work has been adopted from the authors' previous study Yadav and Bhagoria (2013). The domain consisted of three sections, namely entrance section (L1), test section (L2), and exit section (L3). The internal duct cross section is $50 \text{ mm} \times 10 \text{ mm}$. The rib pitch (P) and rib height (e) were varied. The rib pitch to rib height ratio, P/e , varied from 4.46 to 8.57. The rib height to hydraulic diameter ratio, e/D , varied from 0.049 to 0.11, and Reynolds number (Re) varied from 3000 to 12000.

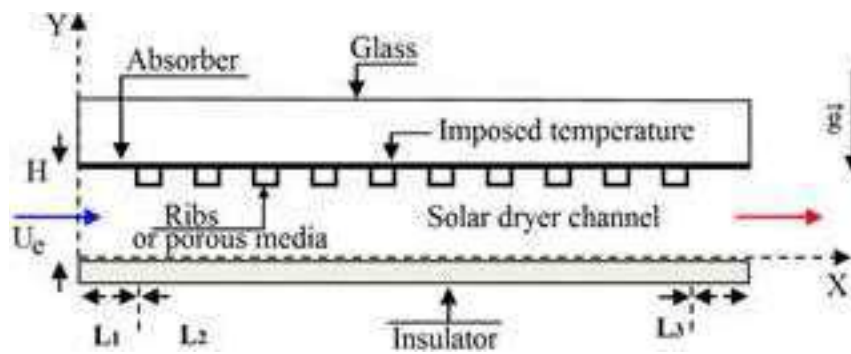


Figure 1. Schematic of 2D computational domain

2.2. Model Development

In this study, we based on the numerical optimization of geometric and physical parameters to improve the performance of a horizontal solar collector by integrating, on the one hand, solid ribs and on the other hand porous ribs. To achieve this objective, the flow and heat transfer in turbulent forced convection in the solar collector channel were analysed.

Consider a forced convection with turbulent flow inside a parallel plate heater. A porous rib is placed at the plate with thickness (e). The fluid (air) enters the domain with a uniform velocity distribution (U_e) and constant temperature (T_e). A constant and hot temperature (T_c) is used at the plate and it is uniform along the channel. Computational domain and coordinate system for the heater are shown in Figure 02. Numerical analysis was performed using ANSYS to solve the governing equations, Navier Stokes equations, and the Darcy- Brinkman Forchheimer model in the porous domain

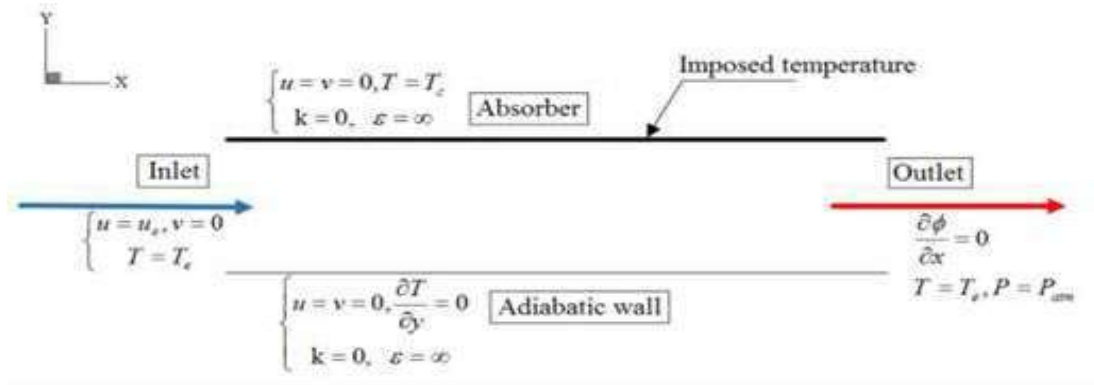


Figure 2. Computational domain for the heater

TABLE I. GOVERNING EQUATIONS

Equations	ϕ	Γ	S_ϕ
Continuity equation	1	0	0
Momentum equation	u	$\frac{(1+\nu_i^*)}{Re}$	$-\frac{\partial P^*}{\partial x^*} + \frac{1}{\varepsilon Re} \left[\frac{\partial}{\partial x_j^*} \left((1+\nu_i^*) \frac{\partial u_j^*}{\partial x^*} \right) \right]$ $-\frac{1}{Re Da} u_i^* - \frac{C_F}{\sqrt{Da}} \sqrt{u_i^2 + u_j^2} u_j$
	v		$-\frac{\partial P^*}{\partial y^*} + \frac{1}{\varepsilon Re} \left[\frac{\partial}{\partial x_j^*} \left((1+\nu_i^*) \frac{\partial u_j^*}{\partial y^*} \right) \right]$ $-\frac{1}{Re Da} u_i^* - \frac{C_F}{\sqrt{Da}} \sqrt{u_i^2 + u_j^2} u_j$
Energy	θ	$\frac{Re(1+\alpha_i^*)}{Pe}$	0
Turbulent energy	k	$\frac{1}{Re} \left(1 + \frac{\nu_i}{\sigma_k} \right)$	$\frac{1}{Re} (P_k^* + G_k^* - \varepsilon^*)$
Turbulent dissipation	ε	$\frac{1}{Re} \left(1 + \frac{\nu_i}{\sigma_\varepsilon} \right)$	$\frac{1}{Re} [C_{\varepsilon 1} (P_k^* + C_{\varepsilon 3} G_k^*) - C_{\varepsilon 2} \varepsilon^*] \frac{\varepsilon^*}{k^*}$

3. Results and discussions

Before presenting and discussing the results obtained, some simulations were carried out, in order to validate the calculation model considered in our numerical simulations, by comparing its results to the experimental data presented in the literature to give credibility to the performed work. Figure 03 shows the digital code validation. Noting that the deviation of the Nusselt number reaches 13.02% for the standard k- ε model, while it does not exceed 6.63% for the RNG k- ε model. Therefore, it is recommended to use the RNG k- ε model exclusively in the rest of the simulation process.

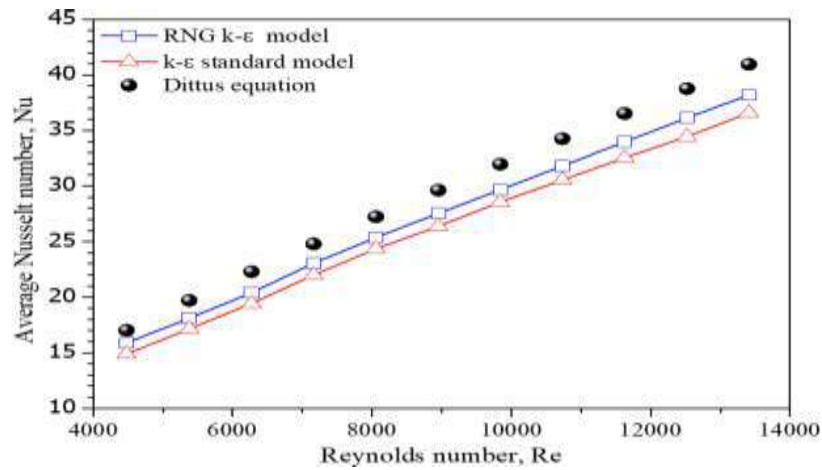


Figure 3. Validation of our numerical model

Figure 4 illustrates the evolution of the average Nusselt number as a function of mesh density, showing that the accuracy of the numerical results improves with an increase in the number of elements. Mesh independence is achieved at 93,092 elements, beyond which the Nu values stabilize (with variations of less than $\pm 1\%$). The selected non-uniform quadrilateral mesh, characterized by a first near-wall cell size of 1.46 mm, optimizes both the resolution of boundary layer effects and computational efficiency, thereby ensuring the numerical robustness of the simulations.

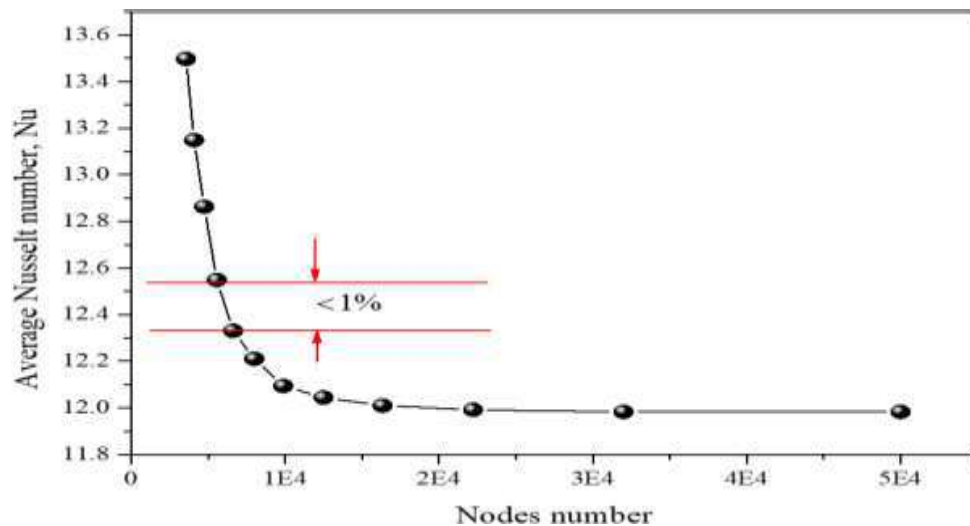


Figure 4. Evolution of the average Nusselt number according to the different meshes.

Figure 5 shows the variation of the heat transfer rate as a function of the relative roughness height (e/D). it is found that the Nusselt number (Nu) peak corresponds to $e/D = 0.055$ ($Re=8000$, $\Delta T=73.7^\circ C$). Below this height, ribs inadequately disrupt the thermal boundary layer. Above it, excessive flow blockage and recirculation zones reduce heat transfer. This identifies $e/D=0.055$ as the optimal height for maximizing thermal performance.

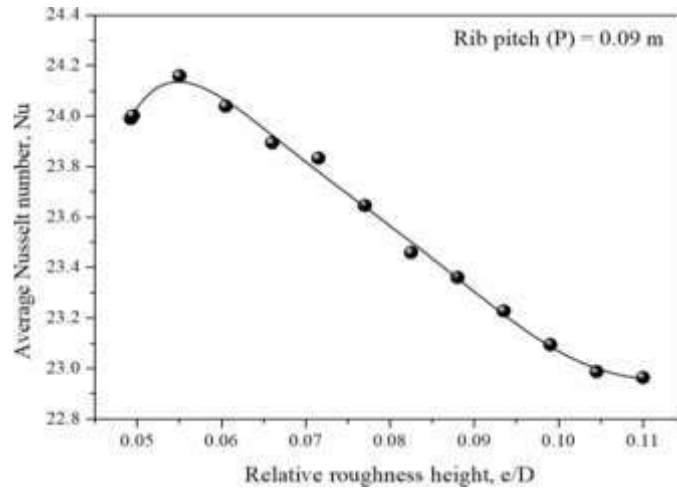


Figure 5. Variation of the average Nusselt number (Nu) as a function of the relative roughness height (e/D), ($\Delta T = 73.7^\circ C$ and $Re= 8000$)

Figure 6 shows the evolution of the average Nusselt number as a function of the relative roughness pitch (P/e). It is observed that the average Nusselt number (Nu) increases with P/e ($Re=8000$), achieving a 48.5% improvement compared to the smooth channel SAH. At lower P/e , the ribs are too close together, causing problems with flow reconnection; whereas, at higher P/e , turbulence generation is reduced. $P/e=0.05$ optimally balances boundary layer disruption and flow redevelopment.

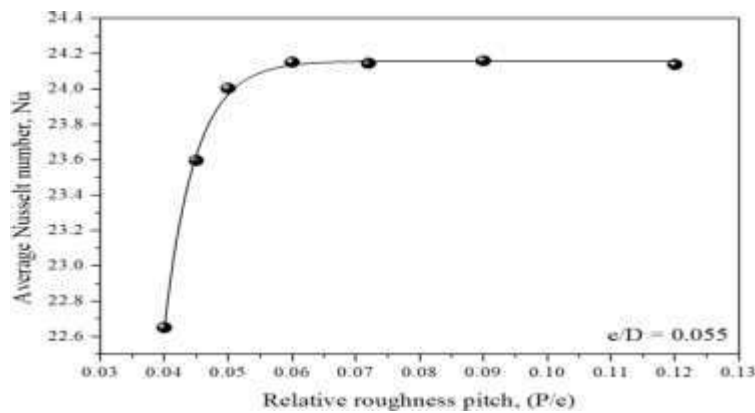


Figure 6. Variation of the average Nusselt number (Nu) as a function of the relative roughness pitch (P/e), ($\Delta T = 73.7^\circ C$ and $Re= 8000$)

Figure 7 shows the effect of porosity on the Nusselt number for the solar air heater absorber. This indicates that the average Nusselt number (Nu) decreases as porosity increases. Low- porosity ribs (high solid fraction) maximize conductive heat transfer through the solid matrix. High porosity (>75%) permits significant flow bypassing, reducing fluid-solid interaction. This highlights a trade-off, lower porosity boosts Nu but may increase weight/cost.

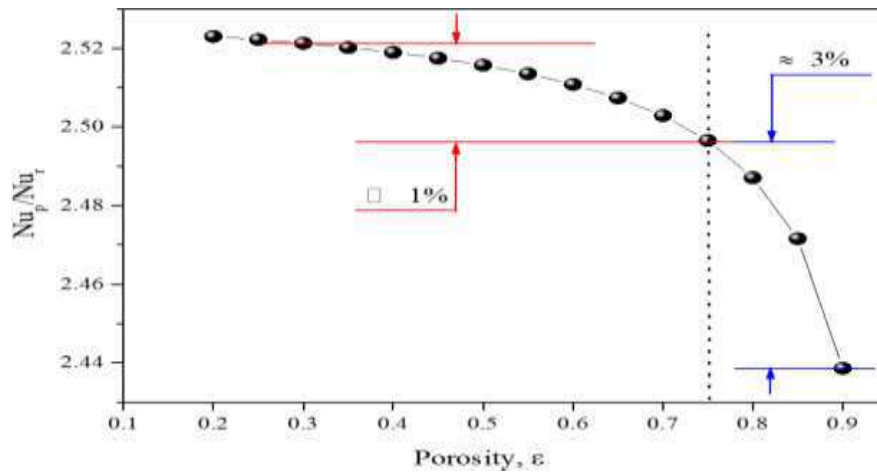


Figure 7. Variation of the average Nusselt number (Nu) as a function of the porosity, ($\Delta T = 73.7^\circ\text{C}$ and $Re = 8000$)

4. Conclusion

The numerical simulation of a solar air heater whose absorber plate has porous ribs is carried out in the present study. It is observed that the implementation of a porous ribs over the absorber plate significantly increases the heat transfer rate in the solar air heater duct. These results can be attributed to the turbulence effects within the porous ribs.

This numerical study demonstrates that integrating porous ribs onto the absorber plate of solar air heaters (SAHs) is a highly effective strategy for enhancing thermal performance while mitigating friction losses. Using a rigorously validated CFD model (RNG $k-\epsilon$ turbulence and Darcy-Brinkman-Forchheimer porous media treatment), we analyzed turbulent airflow ($Re: 3000-12000$) and optimized critical geometric parameters. Key findings reveal:

- Porous ribs increase the average Nusselt number by 20–50% across the Reynolds number range compared to conventional smooth-channel SAHs, confirming superior heat transfer intensification.
- Thermal performance peaks at the optimal geometric ratios, where the relative rib height e/D^*

= 0.055 and the relative rib pitch $*P/e* = 0.05$, achieving a 48.5% Nu enhancement at $Re=8000$.

- Porosity has an inverse relationship with heat transfer. As porosity increases Nu decreases, which suggests that lower porosity ribs (higher solid fraction) are best for maximizing thermal gain.
- Most importantly porous ribs have a lower friction when compared to solid rib turbulators at the same level of heat transfer enhancement, highlighting their superior thermo- hydraulic performance (THP).

These results provide actionable design guidelines for implementing porous ribs in SAHs. By strategically optimizing rib geometry ($*e/D*$, $*P/e*$) and porosity, engineers can develop significantly more efficient solar heating systems with lower pumping power requirements. This work advances passive heat transfer enhancement techniques for sustainable energy applications.

References

- [1]J. A. Duffie and W. A. Beckman, “Solar Engineering of Thermal Processes: Fourth Edition,” Solar Engineering of Thermal Processes: Fourth Edition, Apr. 2013, doi: 10.1002/9781118671603.
- [2]V. S. Hans, R. P. Saini, and J. S. Saini, “Performance of artificially roughened solar air heaters—A review,” Renewable and Sustainable Energy Reviews, vol. 13, no. 8, pp. 1854–1869, Oct. 2009, doi: 10.1016/J.RSER.2009.01.030.
- [3]A. S. Yadav and J. L. Bhagoria, “A CFD based thermo-hydraulic performance analysis of an artificially roughened solar air heater having equilateral triangular sectioned rib roughness on the absorber plate,” Int J Heat Mass Transf, vol. 70, pp. 1016–1039, Mar. 2014, doi: 10.1016/J.IJHEATMASSTRANSFER.2013.11.074.
- [4]P. Promvonge and C. Thianpong, “Thermal performance assessment of turbulent channel flows over different shaped ribs,” International Communications in Heat and Mass Transfer, vol. 35, no. 10, pp. 1327– 1334, Dec. 2008, doi: 10.1016/J.ICHEATMASSTRANSFER.2008.07.016.
- [5]Y. M. Patel, S. V. Jain, and V. J. Lakhera, “Thermo-hydraulic performance analysis of a solar air heater roughened with reverse NACA profile ribs,” Appl Therm Eng, vol. 170, p. 114940, Apr. 2020, doi: 10.1016/J.APPLTHERMALENG.2020.114940.
- [6]R. L . Webb and N.-Hyun. Kim, Principles of enhanced heat transfer, Second edition. Taylor & Francis, 2005. doi: <https://doi.org/10.1201/b12413>.

- [7] R. P. Saini and J. Verma, "Heat transfer and friction factor correlations for a duct having dimple-shape artificial roughness for solar air heaters," *Energy*, vol. 33, no. 8, pp. 1277–1287, Aug. 2008, doi: 10.1016/J.ENERGY.2008.02.017.
- [8] S. Singh, S. Chander, and J. S. Saini, "Heat transfer and friction factor correlations of solar air heater ducts artificially roughened with discrete V-down ribs," *Energy*, vol. 36, no. 8, pp. 5053–5064, Aug. 2011, doi: 10.1016/J.ENERGY.2011.05.052.
- [9] A. A. El-Sebaei and S. M. Shalaby, "Solar drying of agricultural products: A review," *Renewable and Sustainable Energy Reviews*, vol. 16, no. 1, pp. 37–43, Jan. 2012, doi: 10.1016/J.RSER.2011.07.134.
- [10] D. A. Nield and A. Bejan, "Convection in porous media," *Convection in Porous Media*, pp. 629–982, Jan. 2017, doi: 10.1007/978-3-319-49562-0/COVER.
- [11] A. J. Mahmood, L. B. Y. Aldabbagh, and F. Egelioglu, "Investigation of single and double pass solar air heater with transverse fins and a package wire mesh layer," *Energy Convers Manag*, vol. 89, pp. 599–607, Jan. 2015, doi: 10.1016/J.ENCONMAN.2014.10.028.
- [12] T. Alam and M. H. Kim, "Heat transfer enhancement in solar air heater duct with conical protrusion roughness ribs," *Appl Therm Eng*, vol. 126, pp. 458–469, Nov. 2017, doi: 10.1016/J.APPLTHERMALENG.2017.07.181.
- [13] K. Hooman and H. Gurgenci, "Porous Medium Modeling of Air-Cooled Condensers," *Transp Porous Media*, vol. 84, no. 2, pp. 257–273, Nov. 2010, doi: 10.1007/S11242-009-9497-8/METRICS.



Photocatalytic Hydrogen Production From TiO₂

Sabah Menia^{1*}, Fetta Danane¹, Mounia Belacel¹, Maroua Benlembarek²

¹ Centre de Développement des Energies Renouvelables BP. 62 Route de l'Observatoire
Bouzareah 16340 Algiers, Algeria, s.menia@cder.dz

² University of Sciences and Technology Houari Boumediene BP. 32 Bab Ezzouar, 16111
Algiers, Algeria

*Corresponding author: (Sabah Menia), Email Address: s.menia@cder.dz

Abstract

The production of hydrogen by photo-catalysis under solar irradiation is an attractive process for generating green hydrogen to reduce CO₂ emissions. Because of their specific physico-chemical properties, TiO₂ photo catalysts have generally been used for hydrogen production. However, their wide band gap, which can only be activated under UV light and the rapid recombination of charge carriers, limits their photo-catalytic applications. However, a number of approaches have been put forward to reduce the energy of its band gap for visible light activity. Among them, TiO₂ doping can be examined as an effective process not only for shifting light absorption towards the visible region, but also for reducing charge recombination. This study focuses on enhancing the photo catalytic activity of TiO₂. In addition, the synthesis processes used for doped TiO₂ were meticulously examined. In addition, a metal such as Cu and noble metals such as Au and Pt are the most widely studied dopants for TiO₂. In addition, nitrogen was also used as a non-metal because of its ability to decrease the band gap energy of TiO₂. The results also revealed that the sol-gel process is widely used in the synthesis of doped TiO₂ photo catalysts because of the crystallinity and high surface area of the nanoparticles obtained.

Keywords: hydrogen production; photo catalysis; renewable energy; TiO₂

<https://doi.org/10.63070/jesc.2025.044>

Received 10 July 2025; Revised 15 November 2025; Accepted 16 December 2025;
Available online 24 December 2025.

Published by Islamic University of Madinah on behalf of *Islamic University Journal of Applied Sciences*.
This is a free open access article under the Creative Attribution (CC.BY.4.0) license.

1. Introduction

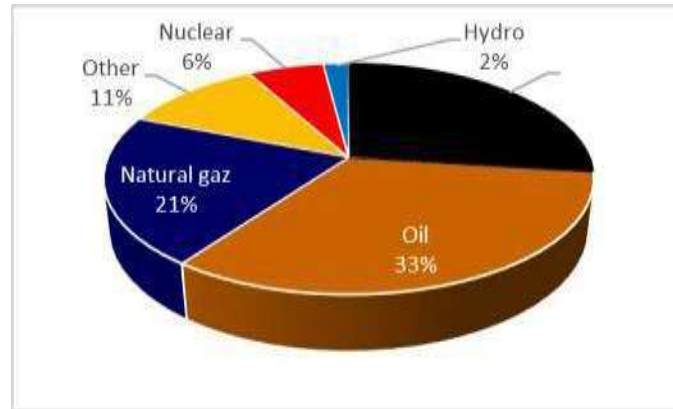
The growing population and improving living standards result in an increase in energy demand. To meet this demand, it is essential to increase energy production. Fossil fuels play an important role in solving energy problems, but they cannot be considered a powerful energy source because of their contribution to global pollution, as they release greenhouse gases. These oxides are toxic to human health and are one of the main causes of global warming. The depletion of fossil fuels also explains their unsatisfactory contribution to the achievement of energy objectives. These energy upheavals and the global pollution resulting from the consumption of fossil fuels are pushing us to seek an alternative path that must use a renewable energy source and provide an environmentally friendly solution to meet global energy needs. Renewable energies that produce fewer greenhouse gas emissions must replace fossil fuels.

Hydrogen is a formidable energy carrier, highly combustible and renewable, which plays a key role in solving the current energy crisis. Hydrogen can be produced from a wide range of sources, stored in different forms and converted into different fuels. Producing hydrogen from water or any other renewable resource will reduce the ecological damage caused by the energy zone, as there are no carbon emissions.

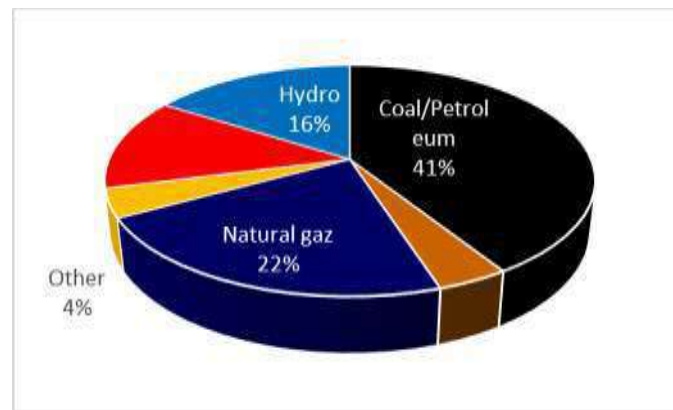
Hydrogen can be produced in several ways, such as steam reforming, coal gasification, thermochemical processes, and biological processes.

Photo catalysis of water using solar radiation is the most efficient method of producing hydrogen, which has the effect of preventing greenhouse gas pollution caused by the use of fossil fuels. This process shows several advantages, including better energy conversion efficiency, separate emission of hydrogen and oxygen and environmental friendliness. Reactors can be built on a small scale, increasing their commercial efficiency and restricting demand for photovoltaic installations.

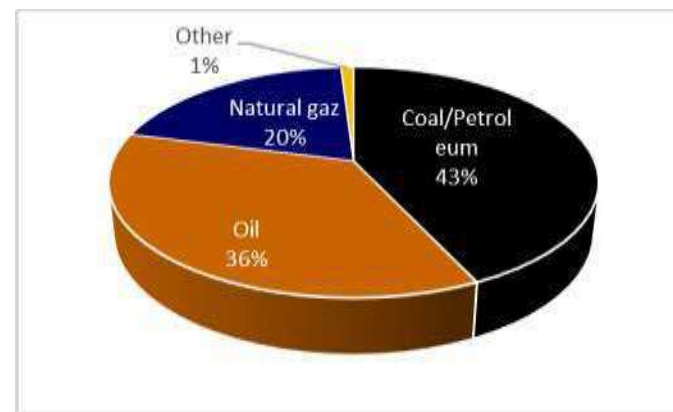
Water photo catalysis, also called "artificial photosynthesis", is based on the transformation of solar fuel into chemical form by exposure to solar radiation with the help of a suitable catalyst. The photo catalyst is never exhausted during the chemical reaction, but it participates in the dynamics of the photo catalytic reaction. The production of hydrogen on an industrial scale remains a major challenge that requires efficient and suitable methods for converting solar energy into fuel [1].



(a)



(b)



(c)

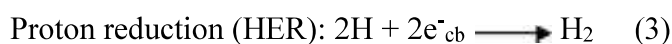
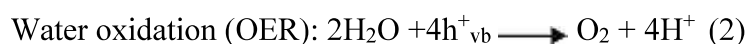
Figure 1. World's shares of fuel for (a) energy supply, (b) generation of electricity, and (c) emission of CO₂ emissions in 2020 [1]

2. Water Splitting

2.1. Basic Principle of Water Splitting

From a thermodynamic point of view, the separation of water is an endothermic process that requires an energy equivalent to $\Delta G^\circ = 237 \text{ kJ/mol}$ or a potential value of 1.23 eV for a single electron. A photon of adequate energy is captured to split water in order to meet this colossal criterion. The evolution of oxygen and hydrogen in the electrochemical splitting of water is based on a four-electron and two-electron process respectively, as shown in the following equations.

Absorption of light:



$$\Delta G^\circ = 237.2 \text{ kJ mol}^{-1}$$

It is interesting to use a suitable photo catalyst capable of producing e/h pairs by absorbing photons of an appropriate energy. These e/h pairs generated by the photo catalyst are responsible for the oxidation-reduction reactions of the water molecules on the surface of the catalyst with an energy of 1.23 eV to produce a photo excited e/h pair and carry out the oxidation-reduction reactions. [1]

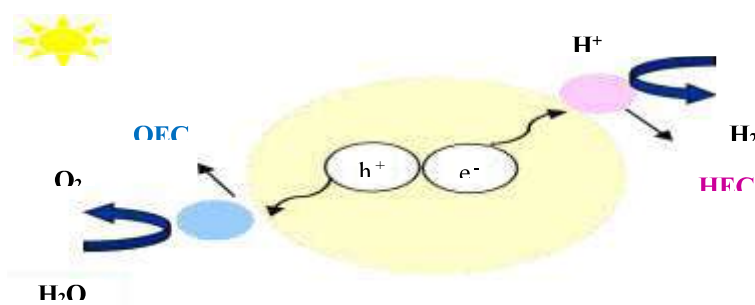


Figure 2. Photocatalytic splitting of H₂O [1]

2.2. Types of photo catalytic water splitting reaction

Photochemical water separation can be carried out on two types of photosystems: Particulate photo catalytic systems (PPS) and Photo-electrochemical cells (PEC).

The particulate system is a system in which the photo catalyst is poured into an aqueous solution in powder form. In this system, each particle acts as a microelectrode and is responsible for the oxidation-reduction reactions of the water on the surface of the photo-catalyst. As there is no pellica deposited in the PPS, no additional substrate is required, making it a simple and inexpensive water separation process. The second advantage associated with PPS is the larger surface area of the photo-catalyst, with more active sites. Although PPSs are simple and inexpensive, they are less efficient because of the lower productivity of charge separation and the difficulty of charge recombination, which results in a lower rate of hydrogen production.

The photo-catalytic separation of water in PPS consists of three phases: A photon of desirable energy, i.e. $h\nu$, equal to or greater than E_g of the photo-catalytic semiconductor, strikes the photo-catalytic surface and is absorbed by the semiconductor during the first phase. This $h\nu$ absorption causes charge acquisition on the photo-catalytic semiconductor substrate, with the conduction band (CB) becoming more electronegative while the valence band (VB) becomes more electropositive due to the production of negatively charged entities (electrons) in CB and positively charged entities (holes) photo-generated in VB. The second phase involves charge separation and transport, i.e. the movement of holes and electrons to the reaction sites of the photo catalytic semiconductor. Finally, chemical transformations occur at the surface of the photo catalytic semiconductor, in which the photo generated holes and electrons oxidize and reduce the water molecules adsorbed on the surface of the semiconductor. [1]

3. Types of reactions

There are two types of reaction by which hydrogen can be generated by photo catalysis of water: (i) photochemical cell reactions and (ii) photo electrochemical cell reactions. [2]

Photochemical reactions including the photo catalyst suspension in solution were studied by Liao et al and Jiang et al [3-4] as being accomplished by the direct use of energy for the occurrence of the chemical reaction. The variation in hydrogen and oxygen is the result of the division of water with the appropriate photo-catalyst after the absorption of sufficient light energy. Certain properties of the photo catalyst, such as its ability to absorb light during suspension, changes in the pH value of the reaction in progress, and the concentration of the substrate, become difficult to control. The hydrogen gas advances to the semiconductor-electrolyte junction, which acts as an interface to produce the

potential required for water splitting, but it is difficult to observe the experimental results because the kinetics of the reaction are influenced by these factors, making the operation quite laborious. [2]

4. TiO₂ AS PHOTO CATALYST

As a photo catalyst, TiO₂ is gaining in popularity and is the most studied photo catalyst due to its many advantages, such as its high thermal and chemical stability, low cost, high photo catalytic efficiency, high refractive index and non-toxicity. [5] Chong et al [6] examined the fundamentals of the photo catalyst, photo reactor development, process optimization, kinetic modelling and parameters that affect process efficiency. In another review, Schneider et al [7] have summarized certain aspects of TiO₂ photo catalysis, particularly charge carrier transport kinetics, new mechanistic aspects and exceptional doping methods to improve photo catalytic activities and extend the range of accessible wavelengths. Ni et al [8] have highlighted the transformation techniques and chemical additives used to improve the photo-catalytic activity of TiO₂ for hydrogen production. However, the efficiency of hydrogen production by photo catalysis is limited because of the energy of the wide band gap and the rapid recombination rate of charge carriers. As a result, a number of experiments have been developed not only to reduce its band gap energy but also to reduce charge carrier recombination, such as doping with a metal or non-metal to reduce the band gap energy and assembly with other semiconductors or loading with cocatalysts to improve charge separation. Titanium dioxide (TiO₂) comes in three types of crystals: anatase, rutile, and brookite. Anatase, whose band gap energy is equal to 3.2 eV, is the most active photo catalytic polymorph of titanium because of its greater kinetic stability. Unlike brookite, anatase is readily available in pure form. Rutile, which has the lowest band gap energy (around 2.96 eV), is the most stable form of titanium and is usually used as a white pigment. On the other hand, the brookite phase is not commonly used in photo catalysis because it cannot be obtained in a pure state like anatase or rutile [5].

5. Synthesis of TiO₂ Doped Materials

5.1. Sol-Gel Method

The sol-gel process is a fundamental low-temperature process generally used to prepare nanoparticles. It offers a number of advantages, including good homogeneity, a rapid process, low calcination temperature and minimal time. The nanoparticles obtained therefore have good crystallinity and a large specific surface area. In this process, the precursors of the substances obtained were dissolved in a solvent and the pH was checked until the sol was formed. The gel was then obtained by heating the solution containing the precursors; oxide or hydroxide nanoparticles were produced by hydroxylation and poly condensation reactions. Finally, the gel was calcined to

form nanoparticles at an ideal calcination temperature. An iron and chromium doped TiO₂ thin film using combined RT and soluble gel processes was successfully synthesized by Dholam et al [9]. The activities of doped TiO₂ photo-catalysts were tested for the evolution of hydrogen under visible light irradiation. The results showed that the doped substances have higher activities than undoped TiO₂, which is attributed to the role of chromium and iron, which act as electron trapping agents. The sol-gel process was used to prepare N-doped TiO₂ using ethylene diamine as the nitrogen source for hydrogen evolution and methyl orange degradation by Li et al [10]. The EDTA/TiO₂ ratio calcined at 500°C shows superior photo-catalytic performance. The decrease in band gap energy and the enhancement of light absorption are thought to be the cause of the improved activity of nitrogen-doped titanium.

The sol-gel process has been widely used as an encouraging and attractive process for the preparation of TiO₂ nanoparticles or thin films. In addition, the sol-gel process does not require a high temperature as in the case of the solid state reaction, nor does it require complex equipment as in the case of the microwave assistant process [5].

5.2. Hydrothermal/Solvothermal Method

The hydrothermal or solvothermal process is commonly used in inorganic chemistry for the synthesis of inorganic nanomaterial of various configurations for a variety of applications. The difference between these two processes lies in the prior use of water as a solvent. This method carries out a chemical reaction at controlled temperature and pressure in solvents enclosed in closed steel autoclaves. This method has two phases: nucleation and crystal growth. What's more, this system accurately controls a number of factors that influence synthesis, such as pH, temperature and additives. Subsequently, nanomaterial with high crystallinity and suitable granulometry and configuration were obtained. Silver and iron were successfully deposited on anatase TiO₂ by Sun et al using a solvothermal process. The photo catalytic activity of doubly doped metals was promoted in order to generate hydrogen. Among the various doped substances, the 4.5% Fe-4.5% Ag/TiO₂ mixture showed the most potent hydrogen production activity, due to improved light absorption and charge-breaking efficiency. N-doped Nano TiO₂ belts with co-exposed faces were successfully produced using the hydrothermal process by Sun et al [11]. The results showed that these co-exposed surface heterojunction faces of the N-doped Nano TiO₂ belts showed the highest activity for hydrogen variation. The separate load carrier break provided by this assembly was considered to be the cause of this highest activity. Wu et al. synthesized bismuth-doped titanium dioxide hydrothermally to generate hydrogen [12]. The hydrothermal method is generally used to

prepare different metal oxides in distinctive configurations because of its many advantages, such as improved chemical activity in aqueous media, better control of nanoparticle size and shape, and induced crystallization. However, the high cost of the closed autoclave, the inability to observe the reaction process and certain safety issues limit its application to the synthesis of nanomaterial [5].

5.3. Precipitation method

In addition to sol-gel and hydrothermal/solvothermal methods, precipitation is one of the most interesting processes for synthesizing Nano catalysts. This simple method produces a highly active photo catalyst with a large specific surface area and small grain size. In this process, the metal precursors are dissolved in a suitable solvent in a glass beaker. The mixture is then stirred and gently heated. Afterwards, the pH is accurately checked. The oxide photo catalyst can be obtained by centrifugation, filtration and repeated washing with water and alcohol. More recently, Fe(III)-doped TiO_2 has been synthesized by precipitation using TiCl_4 and iron nitrate as the titan and iron precursors, respectively by Ismael et al [13]. The photo catalytic activity of photo catalysts has been tested for the production of hydrogen and the degradation of organic pollutants. TiO_2 doped with Fe at 0.1% by mass showed the highest activity. It is important to note that increasing the amount of iron reduces the activity, which is attributed to the fact that iron acts as a recombination element in high concentrations. In their study, Yoong et al [14] used a combination of precipitation and impregnation processes to synthesize various concentrations of Cu-doped TiO_2 to generate hydrogen. They found that 10% by mass of Cu sintered at 300°C showed the highest activity. Enhancing light absorption and reducing band gap energy play a key role in improving photo catalytic activity. Ruiz et al [15] studied the production of hydrogen from gold deposited on the surface of TiO_2 . Photo catalysts were assembled by precipitation deposition at various calcination temperatures. The ideal gold loading on the TiO_2 surface was 0.5% by mass. The higher activity of doped TiO_2 compared with undoped TiO_2 was attributed to the function of the gold, which acts as an electron trap and hydrogen evolution site. The presence of gold nanoparticles improved the absorption of visible light. In addition, the photo catalysts were activated at various temperatures, revealing that at 500°C , the absorption spectrum and redshift were at their widest. A novel precipitation process for the synthesis of N-doped meso-macro TiO_2 with a specific structure was developed by Parida et al [16]. The photo catalytic activity of the synthesized photo catalysts was estimated for hydrogen production under visible light irradiation. The catalyst calcined at 400°C showed the highest activity, attributed to its mesoporous assembly and distinctive morphology, which aid charge transport and separation, as well as band gap reduction [5].

5.4. Microwave-Assisted Method

The microwave-assisted process is gaining notoriety in nanoparticle synthesis because of its high reaction speed, simplicity and rapidity, ecological specificity and energy transport efficiency. In this process, the substances were heated by irradiation rather than thermal heating, which is the opposite of the usual process. The interaction of microwave irradiation with the polar molecule is used to obtain the dipole moment of the reaction mixture. Molecule rotation can be influenced by activity. This orientation improves the chance of collision between the molecules and reduces energy activation and heat release, leading to increased reaction and formation of the nanoparticle. Applying this process to the synthesis of nanoparticles therefore offers more advantages than the usual synthesis process. Lin et al [17] synthesized a series of distinct metal ions on N-doped TiO₂ using a microwave-assisted process. All the N-TiO₂ photo catalysts co-doped with metal ions showed photo catalytic hydrogen production performances incomparable to those of pure N-TiO₂ and TiO₂. The particularly improved performance of Cu/N-TiO₂ was essentially due to the synergistic effects of copper and nitrogen producing an impurity energy level, reducing the band gap energy, as well as their function in improving charge separation, resulting in the highest possible photo catalytic activity.

Microwave-assisted synthesis is considered to be a fundamental branch of green chemistry. It is widely recognized as a simple and ecologically sustainable method, more energy-efficient than conventional methods such as oil or sand baths. However, the high cost of the equipment, the inadequacy of large proportion production and the complication of monitoring the reaction process limit its application to the synthesis of nanoparticles [5].

5.5. Solid-State Reactions Method

Solid-state chemical reaction for the production of nanomaterial is an attractive process that is widely used in photo catalysis. Compared with other processes such as microwave or hydrothermal, it is highly cost-effective and requires no special equipment or solvents. In this method, the nanomaterial powders obtained from the precursor are thoroughly amalgamated, then transferred to a clean alumina crucible and calcined at high temperature. This method also enables the production of high-crystallinity nanoparticles in large quantities and can be used primarily for the photo degradation of organic contaminants. Iron-doped TiO₂ using TiO₂ powder and FeCl₃ was synthesized using a solid-state reaction by Ghorbanpour et al [18]. The photo catalytic activity of

the specimen samples was studied for the degradation of methyl orange under visible light irradiation. The Fe-doped proportion of 0.5% by mass shows the highest activity, attributed to the improvement in light absorbance and the decrease in band gap energy.

This method is used for nanoparticle synthesis because of its simplicity, accessibility and low cost. However, this process uses high calcination temperatures, which leads to nanoparticles with a limited surface area and a large particle size, thus reducing their photo catalytic activity [5].

TABLE I. Application of different metal/non-metal doped TiO₂ synthesized by different methods for photo catalytic hydrogen production

Dopant	Synthesis method	H₂ production
Platinum	Impregnation/Sol- gel	600 nmol/cm ³
Silver	Sol- gel/solvothermal	180 mmol of H ₂ /gcat
Nitrogen	Oxidation	18 μmol
Nitrogen, Iron, Chromium, Platinum	Hydrolysis	340 μmol
Bismuth, Nitrogen	Sol-gel	1800 μmol/g
Barium, Strontium	Hydrolysis	25 μmol/m ²
Platinum, Nitrogen	Photo deposition	3200 μmol

6. Conclusion

Doping is an attractive process for improving the photo catalytic activity of TiO₂, either by reducing the energy of the band gap or by improving charge separation. Metals such as Cu and noble metals such as Au and Pt are the most frequently studied dopants for TiO₂ because of their superior work function. Nitrogen has been extensively studied as a non- metallic dopant because of its ability to decrease the band gap energy of TiO₂ and enhance the photo catalytic activity of TiO₂. The synthesis processes used to prepare many doped TiO₂ photo catalysts have been explained in detail; many studies have shown that the sol-gel process is still the most commonly used process for synthesizing doped TiO₂ because of certain features, particularly the high surface area and small size of the nanoparticles prepared, recorded at low calcination temperatures. The characterization section illustrated that UV- Vis-DRS spectroscopy, photocurrent and electrochemical impedance spectroscopy are applied to determine the influence of the dopant on the optical properties and charge separation efficiency of TiO₂. Nevertheless, there are a number of key points that should be taken into consideration for further studies on doped TiO₂.

Researchers need to consider the ideal processes for the synthesis of doped TiO_2 , as some processes require dangerous and expensive chemicals and very expensive special equipment should be avoided. In addition, it is essential to achieve the ideal amount of dopant on TiO_2 to obtain the highest photo catalytic hydrogen production activity, otherwise the highest dopant concentration may act as a recombination center. In addition, other studies should focus on finding a low-cost dopant to modify dopants based on very expensive noble metals such as Pt or Au. In addition, photo catalytic chemists should finally focus on finding a suitable sacrificial reagent to be used as a hole trap in the hydrogen production reaction. Ultimately, both laboratory-scale and pilot-scale photo reactor designs for H_2 production should be debated.

In conclusion, the doping process remains an attractive way of improving the photo catalytic activity of TiO_2 . However, research should combine theoretical kinetics and computational research with experimental studies to give a more visible picture of the photo catalytic activity of these substances.

References

- [1] T. Ishaq, M. Yousaf, I. A. Bhatti, A. Batool, M. A. Asghar, M. Mohsin, M. Ahmad. "A perspective on possible amendments in semiconductors for enhanced photocatalytic hydrogen generation by water splitting." *International journal of hydrogen energy*, vol. 46, pp. 39036-39057, 2021.
- [2] S. Singla, S. Sharma, S. Basu, N. P. Shetti, T. M. Aminabhavi. "Photocatalytic water splitting hydrogen production via environmental benign carbon based nanomaterials." *International journal of hydrogen energy*, vol. 46, pp. 33696-33717, 2021.
- [3] C. H. Liao, C. W. Huang, J. C. S. Wu. "Hydrogen production from semiconductor-based photocatalysis via water splitting. *Catalysts*", vol. 2, pp. 490-516, 2012.
- [4] D. Jiang, H. Zhao, Z. Jia, J. Cao, R. John. "Photoelectrochemical behaviour of methanol oxidation at nanoporous TiO_2 film electrodes". *J Photochem Photobiol Chem*, vol. 144, pp. 197-204, 2001.
- [5] M. Ismael. "A review and recent advances in solar-to- hydrogen energy conversion based on photocatalytic water splitting over doped- TiO_2 nanoparticles". *Solar energy*, vol. 211, pp. 522-546, 2020.
- [6] N. M. Chong, B. Jin, K. W. C. Chow, C. Saint. "Recent developments in photo catalytic water treatment technology: a review". *Water Res*, vol. 44, pp. 2997-3027, 2010.
- [7] J. Schneider, M. Matsuoka, M. Takeuchi, J. Zhang, Y. Horiuchi, M. Anpo, W. D. Bahnemann. "Understanding TiO_2 photo catalysis: mechanism and materials". *Chem. Rev*, vol. 114, pp. 9919-

9986, 2014.

[8] M. Ni, M. K. Leung, D. Y. Leung, K. Sumathy. "A review and recent developments in photo catalytic water-splitting using TiO₂ for hydrogen production". *Ren. Sus. Energy Rev*, vol. 11, pp. 401-425, 2007.

[9] R. Dholam, N. Patel, M. Adami, A. Miotello. "Hydrogen production by photo catalytic water splitting using Cr or Fe doped TiO₂ composite thin films photo catalyst." *International journal of hydrogen energy*, vol. 34, pp. 5337-5346, 2009.

[10] H. Li, Y. Hao, H. Lu, L. Liang, Y. Wang, J. Qiu, X. Shi, Y. Wang, J. Yao. "A systematic study on visible light N- doped TiO₂ photo catalyst obtained from ethylenediamine by sol-gel method." *Appl. Surf. Sci*, vol. 344, pp. 112-118, 2015.

[11] T. Sun, E. Liu, J. Fan, X. Hu, F. Wu, W. Hou, Y. Yang, L. Kang. "High photo catalytic activity of hydrogen production from water over Fe doped and Ag deposited anatase TiO₂ catalyst synthesized by solvothermal method". *Chem. Eng. J*, vol. 228, pp. 896-906, 2013.

[12] C.M. Wu, S.J. Chih, K.W. Huang. "Bismuth doping effect on TiO₂ nanofibres for morphological change and photo catalytic performance." *CrystEngComm*, vol. 16, pp. 10692-10699, 2014.

[13] M. Ismael. "Enhanced photo catalytic hydrogen production and degradation of organic pollutants from Fe (III) doped TiO₂ nanoparticles." *J. Environ. Chem. Eng.*, vol. 8, pp. 103676, 2020.

[14] S.L. Yoong, K.F. Chong, K.B. Duta. "Development of copper doped TiO₂ photo catalyst for hydrogen production under visible light." *Energy*, vol. 34, pp. 1652-1661, 2009.

[15] O.S. Ruiz, R. Zanella, R. Lopez, H.A. Cordillo, R. Gomez. "Photo catalytic hydrogen production by water/methanol decomposition using Au/TiO₂ prepared by deposition-precipitation with urea." *J. Hazard. Mater.*, vol. 263, pp. 2-10, 2013.

[16] M.K. Parida, P. Pany, P. Naik. "Green synthesis of fibrous hierarchical meso-macroporous N doped TiO₂ nano photo catalyst with enhanced photo catalytic H₂ production." *International journal of hydrogen energy*, vol. 38, pp. 3545- 3553, 2013.

[17] H.Y. Lin, Y.C. Shih. "Efficient one-pot microwave assisted hydrothermal synthesis of M (M=Cr, Ni, Cu, Nb) and nitrogen co-doped TiO₂ for hydrogen production by photo catalytic water splitting." *J. Mole Catal A: Chem*, vol. 411, pp. 128-137, 2016.

[18] M. Ghorbanpour, A. Feizi. "Iron doped TiO₂ catalysts with photo catalytic activity." *J. Water Environ. Nanotechnol.*, vol. 4(1), pp. 60-66, 2019.



Study Of Mechanical, Electronic and Optical Characteristics for AuBiF₃ Material

Nassah Younes^{1,*}, Benmakhlouf Abdenmour², Remache El Ouardi³

¹ department of ST University of Ammar Thelidji Laghouat, Algeria, y.nassah@lagh-univ.dz

² department of ST University of Ammar Thelidji Laghouat, Algeria, a.benmakhlouf@lagh-univ.dz

³ University of Laarbi Ben M'hidi Oum El Bouaghi, Algeria, rlouardi@yahoo.fr

*Corresponding author:(Nassah Younes), Email: y.nassah@lagh-univ.dz

Abstract

In this study, we present an ab initio theoretical study of the mechanical, electronic, and optical properties of AuBiF₃ using ultrasoft pseudopotentials within the framework of density functional theory (DFT). Our investigation shows the formation energy is negative, which indicates that the material is stable thermodynamically. The elastic properties show that the studied perovskite satisfies the Born stability criteria, confirming its mechanical stability. Additionally, the Pugh ratio (B/G) exceeds 1.75, indicating that the material exhibits ductility. The electronic band gap indicates that this material is a semiconductor with a direct M-M band gap of 1.51 eV, as determined using the HSE06 functional, making it suitable for solar energy applications. An examination of the optical properties shows that the absorption coefficient exhibits significant absorption in the visible range, on the order of 10⁴ cm⁻¹, along with strong ultraviolet absorption, also on the order of 10⁴ cm⁻¹. Our findings suggest that the investigated material possesses notable characteristics, making it promising for solar cell applications and other optoelectronic devices.

Keywords: Perovskite; Absorption; Ductile; Solar Cells; Semiconductor.

<https://doi.org/10.63070/jesc.2025.045>

Received 10 July 2025; Revised 16 November 2025; Accepted 17 December 2025;

Available online 24 December 2025.

Published by Islamic University of Madinah on behalf of *Islamic University Journal of Applied Sciences*.

This is a free open access article under the Creative Attribution (CC.BY.4.0) license.

1. Introduction

The global energy landscape is facing major challenges resulting from a combination of critical factors, including climate change, the constant increase in energy demand linked to population growth, large-scale industrialization, and the progressive scarcity of conventional fossil fuels [1]. The climate emergency and economic constraints are driving scientific and industrial communities to develop renewable and sustainable energy solutions [2]. Solar energy is the most promising alternative among the existing sources due to its nearly infinite supply and demand, compatibility with large-scale activities, and low environmental impact [3]. This dynamic has resulted in deep study into new functional materials that can improve the performance of optoelectronic devices, particularly photovoltaic cells (PVCs) [4]. The target materials must have desirable optical properties such as a high absorption coefficient, high optical conductivity, low reflection, and compatibility with low-cost manufacturing techniques [5]. Halogenated perovskites (PHs) with the formula ABX_3 , where A and B are organic or inorganic cations and X is a halogen anion, have received lot of attention [6]. These materials have proven to be particularly versatile, with applications ranging from solar cells [7] to light-emitting diodes (LEDs) [8], advanced optoelectronic devices [9], and lasers [10]. Perovskite solar cells are notable in the photovoltaic sector for their exceptional electrical and optical properties: extended carrier lifetime, high electron mobility, low exciton binding energy, high absorption capacity in the visible spectrum, and intrinsic tolerance to crystal defects [11].

These advantages position PSCs as highly promising materials for PV applications, where the efficiency of PSCs has seen a dramatic improvement, with the PCE increasing from 3.8 % in 2009 [12] to an impressive 28 % these years [13]. This development is the result of multiple strategies, such as bandgap engineering, interface modification, chemical composition optimization, and defect encapsulation and passivation to limit non-radiative losses [14]. Current theoretical models estimate that the theoretical maximum efficiency of these cells could reach approximately 31.1% [15]. These advances confirm the disruptive potential of halogenated perovskites in next-generation solar technologies and justify the continued exploration of new compositions, device architectures and structural modifications to reconcile high performance and long-term stability.

To advance research in this field, we propose the exploration of new compounds from the halogenated perovskite family, which remain largely unexplored both theoretically and experimentally. To this end, we selected the compound $AuBiF_3$ for an in-depth study based on density functional theory (DFT). The results obtained reveal that this material exhibits a direct bandgap of around 1.51 eV, a crucial characteristic for multijunction solar cells to optimize solar spectral capture and maximize conversion efficiency [16, 17]. This study will provide important information on electronic, elastic, and optical

properties in order to better understand its potential in solar cell applications. Our work seeks to give a complete characterization of the fundamental properties of AuBiF_3 , allowing us to assess its potential for next-generation solar technology. These findings will help to expand the database of functional materials suited to solar energy and may open up new pathways in the construction of high-efficiency solar cells, particularly in multi-layer topologies where band gap optimization is a critical factor.

2. Calculation detail

All calculations presented in this study were performed using the pseudopotential and plane-wave method, as implemented in the ab initio simulation code CASTEP [18]. The treatment of the electron exchange-correlation energy was performed using the generalized gradient approximation (GGA) with the Perdew–Burke–Ernzerhof (PBE) parameterization [19]. For better accuracy in band gap estimation, complementary electronic structure calculations were performed using the hybrid Heyd–Scuseria–Ernzerhof (HSE06) functional [20]. The interactions between ionic cores and valence electrons were described using pseudopotentials method [21]. Kohn-Sham wave functions were developed on a plane-wave basis with a cutoff energy set at 600 eV [22]. The Brillouin zones were discretized according to the Monkhorst-Pack scheme [23] with a $6 \times 6 \times 6$ mesh for structural relaxations and $12 \times 12 \times 12$ for electronic and optical calculations. The mechanical properties of the polycrystalline phases were then evaluated from the constants C_{ij} using the Voigt-Reuss-Hill scheme [24].

3. Structural characteristics

AuBiF_3 compounds crystallize in a cubic perovskite-like structure ABX_3 , belonging to the space group $\text{Pm}\bar{3}\text{m}$ with a number of formulas per unit cell $Z = 1$. In this configuration, Bi^{3+} ions occupy B sites and are octahedral coordinated by six fluorine (F^-) ions, while Au^+ ions reside in A sites, at the center of a cub octahedral cage formed by twelve fluorine ions. The unit cell of the AuBiF_3 perovskite lattice is represented in Figure 1. Before undertaking electronic structure calculations using density functional theory (DFT), a first assessment of the geometric stability of the perovskite phase was performed by applying the semi-empirical Goldschmidt model [28]. This model predicts the crystallographic feasibility of structure based on the tolerance factor, defined by the following equation:

$$t = (r_A + r_x) / \sqrt{2}(r_B + r_x) \quad (1)$$

The variables represent the site X, respectively. The Goldschmidt tolerance factor (t) is a useful parameter for estimating the stable structure of the studied material. When t is close to 1, it indicates an ideal cubic structure, while values between 0.8 and 1.0 suggest the potential stability of a distorted

perovskite phase. The calculated tolerance factor of the investigated compounds exhibits 0.916, which suggests higher stability in the cubic structure. Table 1 summarizes the obtained results

Table 1. ionic radii R_i , tolerance factor t , calculated total energy E_{Tot} , AuBiF₃ perovskite.

Material		R_i	a	t	E_{Tot}	H_f
AuBiF ₃	Au	1.37	4.57	0.81	-3051	-1.74
	Bi	1.07				
	F	1.33				

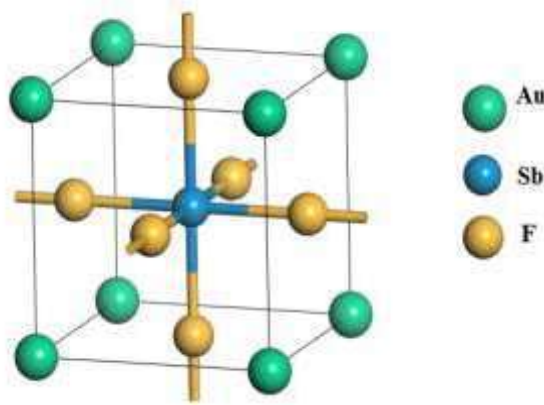


Figure 1. The cubic perovskite structures of AuBiF₃. The Au, Bi and F atoms are all in special Wyckoff positions: 1a: (0,0,0), 1b: (1/2,1/2,1/2) and 3c: (1/2,1/2,0), respectively.

4. Elastic properties

The stiffness and strength of crystalline materials can be assessed via their single-crystal elastic constants. Table 2 presents the values of C_{11} , C_{12} , and C_{44} for the examined compound, ascertained by the strain-stress method [25], elucidating its dynamic response and deformation characteristics under an applied load. The elastic constants were utilized to calculate additional mechanical parameters, including bulk modulus (B), Pugh's ratio (B/G), Young's modulus (E).

The examined material met the Born stability criteria [26] :

$$C_{11} - C_{12} > 0, C_{12} > 0, C_{11} > 0, C_{11} + 2C_{12} > 0, \text{ and } C_{12} < B < C_{11}$$

The bulk modulus (B) quantifies a material's resistance to uniform compression and signifies the extent of resistance during volumetric deformation. Table 2 indicates that the material possesses a high bulk modulus, signifying substantial resistance to hydrostatic pressure.

Young's modulus quantifies the stiffness of an elastic material, defined as the ratio of stress to

strain. The moderate Young's modulus (E) further elucidates the compound's softness. Table 2 illustrates that the current compound has a moderate value, signifying that it deforms more readily under applied stresses and undergoes greater elastic strain compared to stiffer materials with elevated Young's moduli.

The B/G ratio represents the brittleness or ductility of solids [27]. The number above 1.75 implies ductile material, whereas lower values suggest brittle material. The B/G ratio reaches 11.75, demonstrating the ductile nature and flexibility without fracture of the investigated perovskite, which displays high plasticity, which is useful for electronic materials. The obtained results are revealed in the table 2.

TABLE 2. Elastic constants C_{ij} , bulk modulus $B(GPa)$, shear modulus $G(GPa)$, B/G ratio, and Young's modulus $E(GPa)$ of $AuBiF_3$.

Material	C_{11}	C_{12}	C_{44}	B	B/G	E
$AuBiF_3$	138	23	0.25	61	11.75	33

5. Electronic properties

Electronic band structure is a fundamental tool for characterizing the energy states accessible to electrons in a crystal. From the relaxed geometric configurations, we calculated the band structure of the halogenated perovskite compound $AuBiF_3$ using density functional theory (DFT) within the generalized gradient approximation (GGA) framework, according to the Perdew–Burke–Ernzerhof (PBE) parameterization, as implemented in the CASTEP code. The electronic band dispersion was determined along the high-symmetry directions of the first Brillouin zone. The results are presented in Figure 2, for an energy window extending from -15 to 15 eV. The analysis reveals that the valence band maximum (VBM) and the conduction band minimum (CBM) are located at the M point of the Brillouin zone. This configuration confirms that $AuBiF_3$ is a direct bandgap semiconductor, characterized by an (M_c-M_v) -type electronic transition. To obtain a more precise estimate of the bandgap, additional calculations were performed using the hybrid Heyd–Scuseria–Ernzerhof (HSE06) functional. The findings indicate a direct bandgap value of 1.51 eV. This significant value places $AuBiF_3$ as promising compound used in multijunction photovoltaic architectures for high-efficiency solar energy conversion devices[16, 17].

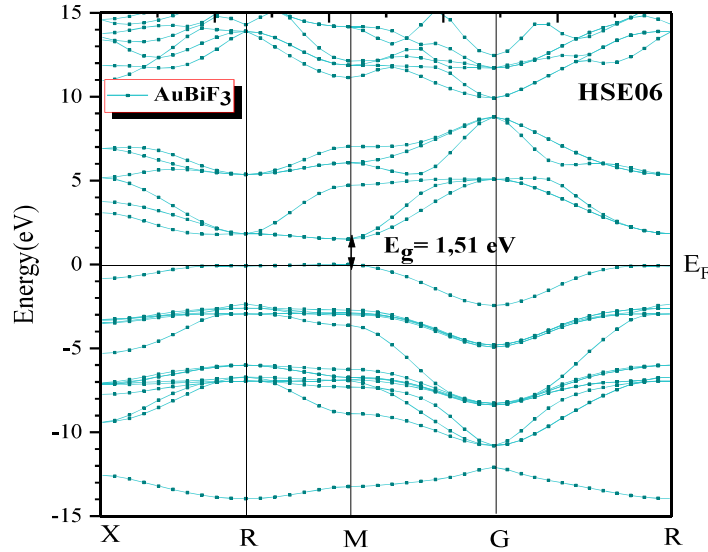


Figure 2. Band structure calculated in high symmetry direction using HSE06 for AuBiF₃ perovskites.

Electronic densities of states (DOS) provide valuable information on the contribution of atomic orbitals to the valence and conduction bands and therefore allow the identification of the electronic origin of the material's band gap. As illustrated in Figure 3, the valence band of both AuBiF₃, located between -12.5 and -5 eV, is dominated by the F-p orbitals with few contribution of Bi: s-p orbitals. Near the Fermi level, the maximum valence band (VBM), which extends from 0 eV to -2.5 eV, is predominantly occupied by Au-d orbitals. The conduction band minimum (CBM) is mainly formed by Bi-p orbitals, while the rest of the conduction band is generated by Au-p and Bi-s orbitals. It can be deduced that the band gap energy of AuBiF₃ is mainly formed by Au-d in (VBM) and Bi-p in (CBM).

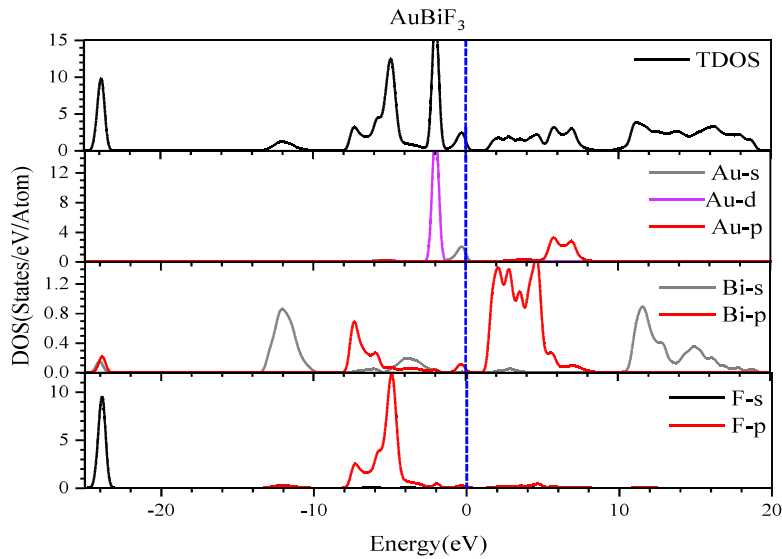


Figure 3. Total (TDOS) and partial density of states (PDOS) calculated using GGA-PBE for AuBiF₃ perovskite.

6. Optical properties

The optical properties of the materials under consideration were investigated throughout a wide spectrum (0 to 25 eV), allowing for an extensive analysis of their electromagnetic response to incident radiation. The complex dielectric function [28], which consists of real $\varepsilon_1(\omega)$ and imaginary $\varepsilon_2(\omega)$ parts, given through the relation

$$\varepsilon(\omega) = \varepsilon_1(\omega) + i\varepsilon_2(\omega)$$

the imaginary part of the dielectric function $\varepsilon_2(\omega)$ can be obtained using the following equation [29] :

$$\varepsilon_2(\omega) = \frac{2\pi e^2}{m_e^2 \omega^2 \varepsilon_0} \sum_{c,v} \int_{BZ} |\langle \psi_k^c | \vec{P}_i | \psi_k^v \rangle|^2 \delta(E_k^c - E_k^v - \hbar\omega) dk^3 \quad (9)$$

the real dielectric function $\varepsilon_1(\omega)$ is derived from $\varepsilon_2(\omega)$ through the Kramers-Kronig [30] relation given by the relation below:

$$\varepsilon_1(\omega) = 1 + \frac{2}{\pi} P \int_0^\infty \frac{\omega' \varepsilon_2(\omega')}{\omega'^2 - \omega^2} d\omega' \quad (10)$$

The real and the imaginary parts allow to calculate the absorption coefficient given as follows

$$\alpha(\omega) = \sqrt{2} \omega \left[\sqrt{\varepsilon_1^2(\omega) + \varepsilon_2^2(\omega)} - \varepsilon_1(\omega) \right]^{1/2} \quad (11)$$

The absorption coefficient $\alpha(\omega)$ is a fundamental parameter in evaluating the optical performance of materials, particularly for solar cell (SC) applications. It measures the efficiency with which a material absorbs incident light energy, reflecting its ability to convert light into electrical energy. Figure 3 shows the variation of the absorption coefficient as a function of photon energy. For candidate solar cell materials, typical absorption coefficient values are between 10^4 and 10^6 cm^{-1} . In the infrared region, the absorbance reaches approximately $2.5 \times 10^4 \text{ cm}^{-1}$, reflecting moderate interaction with low-energy photons. In the visible region between (1.65 and 3.26 eV), a more pronounced absorption is observed, with a peak reaching $6.7 \times 10^4 \text{ cm}^{-1}$, which represents a promising threshold for efficient absorption of sunlight. Progressing towards the ultraviolet region, a sharp increase is noted: the absorbance peaks at $2.5 \times 10^4 \text{ cm}^{-1}$ for a photon energy of approximately 9.03 eV, illustrating a highly absorbing behavior favorable to UV photodetectors and high-performance optoelectronic devices.

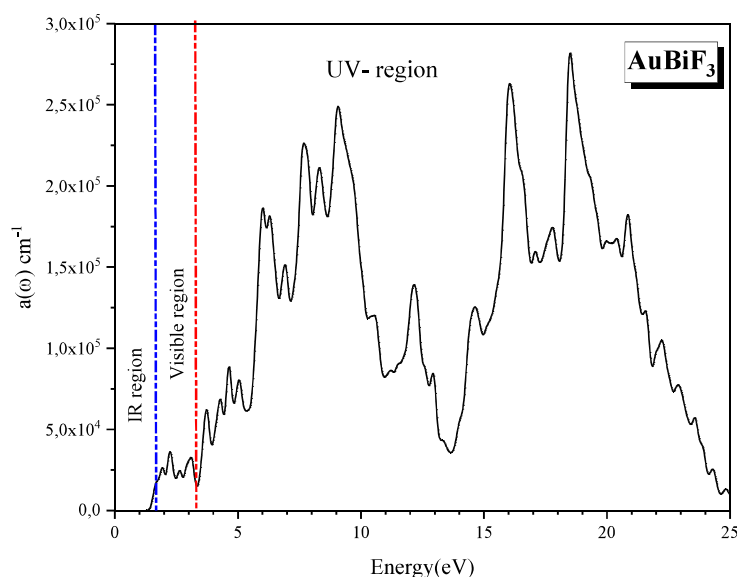


Figure 4. Calculated absorption coefficient using GGA-PBE for AuBiF₃ perovskite.

7. Conclusion

The rapid advancement of photovoltaic technologies, particularly tandem solar cells, requires materials with both high absorption capacity and reliable mechanical stability. The AuBiF₃ perovskite was studied using density functional theory (DFT) to characterize its structural, electronic, and optical characteristics. Electronic analysis indicates a direct band gap of 1.51 eV using HSE06 functional, which coincides with the ideal energy window for the lower layers in tandem multijunction architectures. The optical properties, such as absorption coefficient, demonstrate good absorption in the infrared, visible and ultraviolet regions, suggesting strong photonic interaction in the visible, and near-infrared regions, which is essential for high efficiency. These properties position AuBiF₃ as a strong candidate for next-generation photovoltaic devices, particularly in high-performance tandem cells and multifunctional optoelectronic applications. These results provide a solid theoretical foundation for future experimental work and practical integration on an industrial scale.

References

- [1] P. Basumatary, P. Agarwal, A short review on progress in perovskite solar cells, Mater. Res. Bull., 149 (2022) 111700.
- [2] M. Younas, T.A. Kandiel, A. Rinaldi, Q. Peng, A.A. Al-Saadi, Ambient-environment processed perovskite solar cells: a review, Materials Today Physics, 21 (2021) 100557.
- [3] J. Liao, X. Zhang, S. Guo, S. Zhang, X. Hu, Y. Chen, Fabrication and challenges for high-efficiency and up-scale perovskite solar modules, J. Mater. Chem., 12 (44) (2024) 17720-17741.
- [4] Q.A. Akkerman, L. Manna, What defines a halide perovskite?, ACS energy letters, 5 (2) (2020) 604-610.
- [5] P. Roy, A. Ghosh, F. Barclay, A. Khare, E. Cuce, Perovskite solar cells: A review of the recent advances, Coatings, 12 (8) (2022) 1089.



- [6] A.W. Faridi, M. Imran, G.H. Tariq, S. Ullah, S.F. Noor, S. Ansar, F. Sher, Synthesis and characterization of high-efficiency halide perovskite nanomaterials for light-absorbing applications, *Industrial & Engineering Chemistry Research*, 62 (11) (2022) 4494-4502.
- [7] F. Cao, L. Bian, L. Li, Perovskite solar cells with high-efficiency exceeding 25%: A review, *Energy Mater. Devices*, 2 (1) (2024) 9370018.
- [8] R.H. Friend, D. Di, S. Lilliu, B. Zhao, Perovskite LEDs, *Scientific Video Protocols*, 1 (1) (2019) 1-5.
- [9] R. Dong, Y. Fang, J. Chae, J. Dai, Z. Xiao, Q. Dong, Y. Yuan, A. Centrone, X.C. Zeng, J. Huang, Photodetectors: High-Gain and Low-Driving-Voltage Photodetectors Based on Organolead Triiodide Perovskites (*Adv. Mater.* 11/2015), *Adv. Mater.*, 27 (11) (2015) 1967-1967.
- [10] X. Lu, X. Fan, H. Zhang, Q. Xu, M. Ijaz, Review on preparation of perovskite solar cells by pulsed laser deposition, *Inorganics*, 12 (5) (2024) 128.
- [11] Y. Li, D. Maldonado-Lopez, V. Rios Vargas, J. Zhang, K. Yang, Stability diagrams, defect tolerance, and absorption coefficients of hybrid halide semiconductors: High-throughput first-principles characterization, *J. Chem. Phys.*, 152 (8) (2020).
- [12] A. Kumar, S. Singh, M.K. Mohammed, A.E. Shalan, Effect of 2D perovskite layer and multivalent defect on the performance of 3D/2D bilayered perovskite solar cells through computational simulation studies, *Solar Energy*, 223 (2021) 193-201.
- [13] G. Tong, L.K. Ono, Y. Qi, Recent progress of all-bromide inorganic perovskite solar cells, *Energy Technology*, 8 (4) (2020) 1900961.
- [14] J. Tao, C. Zhao, Z. Wang, Y. Chen, L. Zang, G. Yang, Y. Bai, J. Chu, Suppressing non-radiative recombination for efficient and stable perovskite solar cells, *Energy Environ. Sci.*, 18 (2) (2025) 509-544.
- [15] M.S. Reza, M.S. Reza, A. Ghosh, M.F. Rahman, J.R. Rajabathar, F. Ahmed, M. Sajid, M.F.I. Buian, J. Bhandari, M.A. Islam, New highly efficient perovskite solar cell with power conversion efficiency of 31% based on $\text{Ca}_3\text{Ni}_2\text{I}_8$ and an effective charge transport layer, *Optics Communications*, 561 (2024) 130511.
- [16] D.H. Kim, C.P. Muzzillo, J. Tong, A.F. Palmstrom, B.W. Larson, C. Choi, S.P. Harvey, S. Glynn, J.B. Whitaker, F. Zhang, Bimolecular additives improve wide-band-gap perovskites for efficient tandem solar cells with CIGS, *Joule*, 3 (7) (2019) 1734-1745.
- [17] M.N.A. Dipon, M.A. Sahriar, S. Sarker, M.T. Islam, A. Rauf, M.R.H. Abed, A.R. Nirjhar, S.J. Tan-Ema, K.M. Shorowordi, S. Ahmed, A comprehensive study of mechanically stacked tandem photovoltaic devices: materials selection and efficiency analysis using SCAPS, *Energy Convers. Manage.*, 300 (2024) 117904.
- [18] V. Milman, K. Refson, S. Clark, C. Pickard, J. Yates, S.-P. Gao, P. Hasnip, M. Probert, A. Perlov, M. Segall, Electron and vibrational spectroscopies using DFT, plane waves and pseudopotentials: CASTEP implementation, *Journal of Molecular Structure: THEOCHEM*, 954 (1-3) (2010) 22-35.
- [19] H. Peng, J.P. Perdew, Rehabilitation of the Perdew-Burke-Ernzerhof generalized gradient approximation for layered materials, *Phys. Rev. B*, 95 (8) (2017) 081105.
- [20] J. Heyd, J.E. Peralta, G.E. Scuseria, R.L. Martin, Energy band gaps and lattice parameters evaluated with the Heyd-Scuseria-Ernzerhof screened hybrid functional, *J. Chem. Phys.*, 123 (17) (2005).
- [21] M. Fuchs, M. Bockstedte, E. Pehlke, M. Scheffler, Pseudopotential study of binding properties of solids within generalized gradient approximations: The role of core-valence exchange correlation, *Phys. Rev. B*, 57 (4) (1998) 2134.
- [22] A. Seidl, A. Görling, P. Vogl, J.A. Majewski, M. Levy, Generalized Kohn-Sham schemes and the band-gap problem, *Phys. Rev. B*, 53 (7) (1996) 3764.

- [23] Y. Wang, P. Wisesa, A. Balasubramanian, S. Dwaraknath, T. Mueller, Rapid generation of optimal generalized Monkhorst-Pack grids, *Comput. Mater. Sci.*, 187 (2021) 110100.
- [24] Y. Nassah, A. Benmakhlouf, L. Hadjeris, T. Helaimia, R. Khenata, A. Bouhemadou, S. Bin Omran, R. Sharma, S. Goumri Said, V. Srivastava, Electronic band structure, mechanical and optical characteristics of new lead-free halide perovskites for solar cell applications based on DFT computation, *Bull. Mater. Sci.*, 46 (2) (2023) 55.
- [25] C. Truesdell, Murnaghan's Finite Deformation of an Elastic Solid (1952), in: *An Idiot's Fugitive Essays on Science: Methods, Criticism, Training, Circumstances*, Springer, 1984, pp. 148-150.
- [26] J. Wang, J. Li, S. Yip, D. Wolf, S. Phillpot, Unifying two criteria of Born: Elastic instability and melting of homogeneous crystals, *Physica A: Statistical Mechanics and its Applications*, 240 (1-2) (1997) 396-403.
- [27] O. Senkov, D. Miracle, Generalization of intrinsic ductile-to-brittle criteria by Pugh and Pettifor for materials with a cubic crystal structure, *Scientific reports*, 11 (1) (2021) 4531.
- [28] J.N. Hilfiker, T. Tiwald, Dielectric function modeling, in: *Spectroscopic Ellipsometry for Photovoltaics: Volume 1: Fundamental Principles and Solar Cell Characterization*, Springer, 2019, pp. 115-153.
- [29] H. Kuzmany, H. Kuzmany, The dielectric function, *Solid-State Spectroscopy: An Introduction*, (1998) 101-120.
- [30] M. Orazem, J. Esteban, O. Moghissi, Practical applications of the Kramers-Kronig relations, *Corrosion*, 47 (4) (1991) 248-259.

80	نظام تتبع نقطة القدرة القصوى الهجين - تحكم بسيط في مدمج في أنظمة الطاقة الشمسية Z عاكس مصدر الكهروضوئية المستقل	8
91	تحسين نقل الحرارة في سخانات الهواء الشمسية باستخدام أضلاع مسامية	9
101	إنتاج الهيدروجين التحفيزي الضوئي من ثاني أكسيد التيتانيوم	10
113	دراسة الخصائص الميكانيكية والإلكترونية والبصرية لـ مادة AuBiF_3	11







الفهرس

رقم البحث	المقال	رقم الصفحة
1	التحقق العملي من وحدة تحكم تناسبية تكاملية ذات كسب تكييفي من الرتبة الكسرية لأنظمة الطاقة الشمسية الكهروضوئية المتصلة بالشبكة	1
2	(MPPT) تقييم أداء طرق تتبع نقطة القدرة القصوى والوضع (P&O) باستخدام خوارزمية الرصد والملاحظة الانزلاقي المحسن والمنطق الضبابي في أنظمة الطاقة الشمسية الكهروضوئية: دراسة مقارنة في ظل ظروف منتظمة وغير منتظمة	14
3	نهج اجتماعي اقتصادي لأنشطة تجفيف المحاصيل الزراعية في منطقة غرداية بالصحراء الكبرى	25
4	التحكم المتقدم في جهد الشبكة لأنظمة الطاقة الشمسية الكهروضوئية المتصلة بالشبكة باستخدام قدرات العاكس الكهروضوئي الذكي	34
5	دراسة تجريبية لتكثيف البخار وإزالته في موقد شمسي صندوقي باستخدام قدر ضغط مدمج بأنبوب مرن	48
6	العلاقة بين الأشكال الهندسية للطوب المجوف وكفاءته الحرارية: حالة منزل عائلي في مناخ صحراوي حار	58
7	تحسين أداء الوحدات الشمسية في المناخات القاحلة: استراتيجيات الحد من الغبار في غرداية، الجزائر	71



	<p>Abdul Qadir Bhatti</p> <p>Professor, Civil Engineering, Faculty of Engineering, Islamic University of Madinah. Saudi Arabia</p> <p><u>ORCID Link https://orcid.org/0000-0001-5433-7803</u></p>
	<p>Shamsuddin Ahmed</p> <p>Professor, Industrial Engineering, The Faculty of Computer and Information Systems Islamic University of Madinah, Saudi Arabia.</p> <p><u>https://orcid.org/ orcid.org/</u></p>

Editorial Secertary



	<p>Ahmad Ziad Al-Zuhaily</p> <p>Assistant Editor, Computer science, Engineer, Islamic University of Madinah. Saudi Arabia</p>
	<p>Abdulrahman Saeed Odeh</p> <p>Assistant Editor, Computer science, Engineer, Islamic University of Madinah. Saudi Arabia</p>

	<p>Mussa. A. Said</p> <p>Professor, Chemistry, Islamic University of Madinah, Saudi Arabia.</p> <p>Orcid: https://orcid.org/0000-0003-3073-5449</p>
	<p>Fazal Noor</p> <p>Professor, Computer science and engineering, Islamic University of Madinah. Saudi Arabia</p> <p>Orcid: https://orcid.org/0000-0002-0096-3435</p>
	<p>Basem Rashid Alamri</p> <p>Associate Professor, Electrical Engineering, Taif University, Saudi Arabia</p> <p>https://orcid.org/0000-0002-8667-0042</p>
	<p>Saad Talal Alharbi</p> <p>Professor in Computer Science,  Human Computer Interaction, Faculty of Computers, Taibah University, Saudi Arabia</p> <p>https://orcid.org/0000-0003-0913-8631</p>
	<p>Yazed Alsaawy</p> <p>Associate Professor, Computer and information systems, Islamic University of Madinah. Saudi Arabia</p> <p>Orcid: https://orcid.org/0000-0001-5031-3388</p>

Editorial Board

	<p>Editor-in-Chief: Mohamed Benghanem</p> <p>Professor, Faculty of Science, Islamic University of Madinah, Saudi Arabia.</p> <p>Orcid: https://orcid.org/ 0000-0002-2527-8741</p>
	<p>Managing Editor: Ahmad B. Alkhodre</p> <p>Professor, Computer science, Islamic University of Madinah. Saudi Arabia</p> <p>Orcid: https://orcid.org/0000-0001-6168-3552</p>

Editorial Board Members

	<p>Aly Ramadan Seadawy</p> <p>Professor, Mathematics, Taibah University, Madinah, Saudi Arabia</p> <p>Orcid: https://orcid.org/0000-0002-7412-4773</p>
	<p>Reda Abdelmonsef A. Ibrahim</p> <p>Professor, Biology, Kafrelsheikh University, Egypt</p> <p>Orcid: https://orcid.org/0000-0001-6472-5666</p>

قواعد النشر في المجلة

- أن يكون البحث جديداً، ولم يسبق نشره
- أن يتسم بالأصالة والجدة والابتكار والاضافة للمعرفة
- أن لا يكون مستلماً من بحوث سبق نشرها للباحث/ للباحثين
- أن تراعى فيه قواعد البحث العلمي الاصيل، ومنهجيته.
- أن يشتمل البحث على:
 - ✓ صفحة عنوان البحث باللغة الانجليزية.
 - ✓ مستخلص البحث باللغة الانجليزية.
 - ✓ صفحة عنوان البحث باللغة الانجليزية.
 - ✓ مستخلص البحث باللغة العربية.
 - ✓ مقدمة.
 - ✓ صلب البحث.
 - ✓ خاتمة تتضمن نتائج وتوصيات.
 - ✓ ثبت المصادر والمراجع.
 - ✓ الملاحق الملزمة (إن وجدت).
- في حال (نشر البحث ورقاً) يمنح الباحث نفسه نسخة من عدد المجلة الذي نشر بحثه بها و10 نسخ من بحثه بشكل مستقل
- في حال اعتماد نشر البحث تؤول حقوق نشره كافة للمجلة، ولها ان تعيد نشره ورقياً أو إلكترونياً، ويحق لها
- إدراجه في قواعد البيانات المحلية والعالمية- بمقابل أو بدون مقابل -وذلك دون حاجة للإذن الباحث.
- لا يحق للباحث إعادة نشر بحثه المقبول للنشر في المجلة- في أي وعاء من أوعية النشر- إلا بعد إذن
- كتابي من رئيس هيئة تحرير المجلة
- نمط التوثيق المعتمد في المجلة هو نمط IEEE

معلومات الإيداع

النسخة الورقية :

تم الإيداع في مكتبة الملك فهد الوطنية برقم 1439/8742 وتاريخ 1439/09/17 هـ

الرقم التسلسلي الدولي للدوريات (ردمد) 7936 – 1658

النسخة الإلكترونية:

تم الإيداع في مكتبة الملك فهد الوطنية برقم 1439/ 4287 تاريخ 1439/9/17 هـ

الرقم التسلسلي الدولي للدوريات (ردمد) 7944 -1658

الموقع الإلكتروني للمجلة:

<https://jesc.iu.edu.sa>

ترسل البحوث باسم رئيس تحرير المجلة إلى البريد الإلكتروني

jesc@iu.edu.sa

الآراء الواردة في البحوث المنشورة تعرب عن وجهة نظر الباحث فقط، ولا تُعرب بالضرورة عن المجلة.



Islamic University Journal of Applied Sciences (IUJAS)



مجلة الجامعة الإسلامية للعلوم التطبيقية
(IUJAS)

صادر عن

الجامعة الإسلامية بالمدينة المنورة

إصدار خاص

**7th International Symposium on New and Renewable Energies
October 15 - 16, 2025 Ghardaïa, Algeria**



ديسمبر 2025

بِسْمِ اللَّهِ الرَّحْمَنِ الرَّحِيمِ



الجامعة الإسلامية
ISLAMIC UNIVERSITY OF MADINAH

مجلة الجامعة الإسلامية
للعلوم التطبيقية
مجلة علمية دورية محكمة

مجلة ذات وصول مفتوح



Print ISSN: 1658-7936
Online ISSN: 1658-7944

إصدار خاص ديسمبر ٢٠٢٥